The effects of hand configuration on propulsive forces in swimming

R. Bazuin

Technische Universiteit Delft

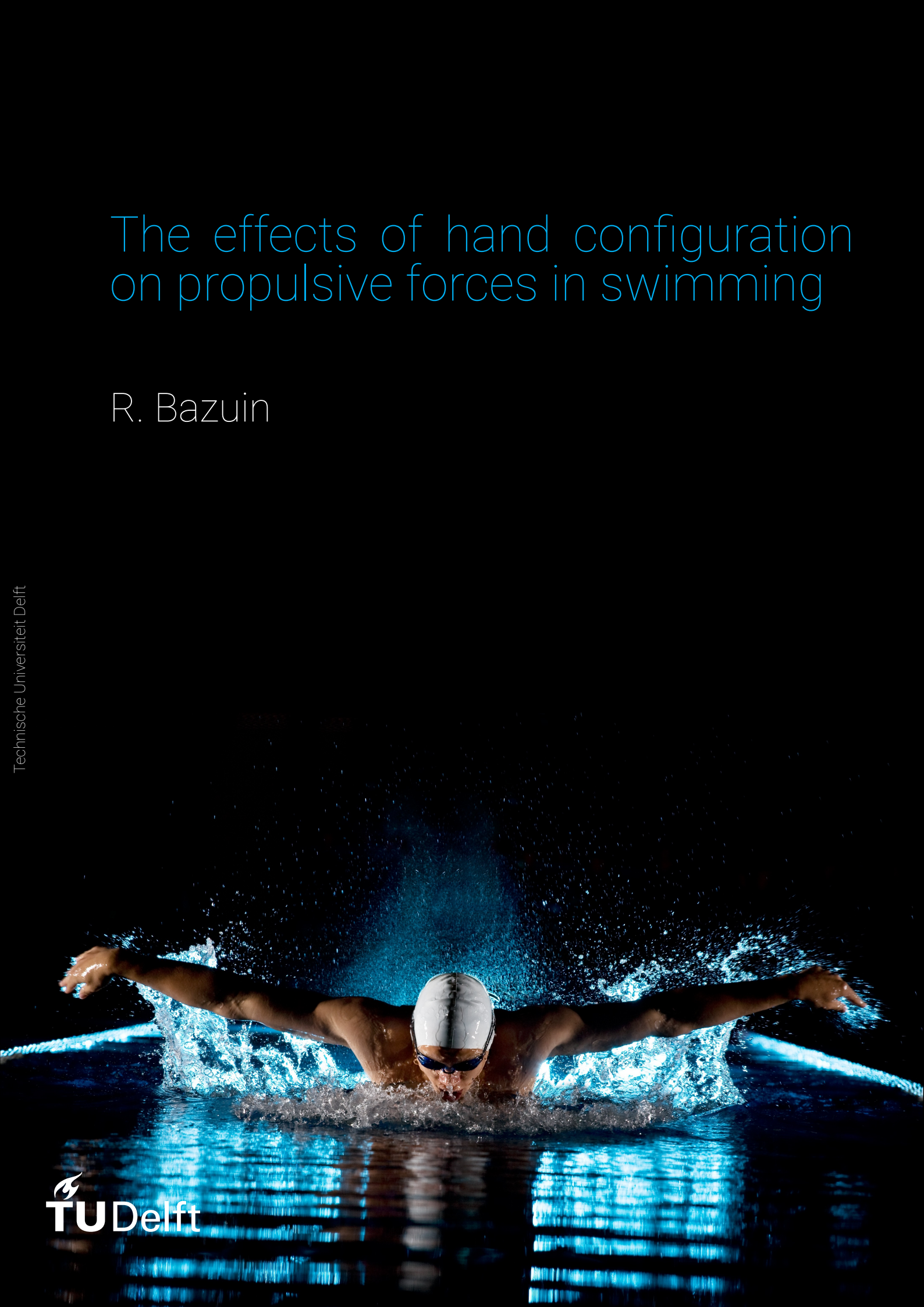

TU Delft

The effects of hand configuration on propulsive forces in swimming

by

R. Bazuin

to obtain the degree of Master of Science
at the Delft University of Technology,
to be defended publicly on Thursday May 3, 2018 at 02:00 PM.

P&E report number:	2892	
Student number:	4226895	
Project duration:	February 20, 2017 – May 3, 2018	
Thesis committee:	prof. dr. ir. W. van de Water,	TU Delft, supervisor
	prof. dr. ir. J. Westerweel,	TU Delft, supervisor
	ir. E. J. Grift,	TU Delft, supervisor
	dr. A. Sciacchitano	TU Delft

An electronic version of this thesis is available at `http://repository.tudelft.nl/`.

Preface

This thesis marks the end of my studies at TU Delft. During the past year I have been working on challenging research towards the effects of hand configuration in swimming. I hope that all the done research expresses itself in performance enhancements in professional swimming. I learnt a lot from the experimental research, where I had the privilege to work with high-end research facilities. This work would not have been possible without the help and guidance of a lot of people.

First and foremost, I would like to thank ir. Ernst Jan Grift for his guidance. I am really grateful that you were always approachable during my thesis and encouraging me. All the discussions we had, thesis related or unrelated, were of great importance to help me think critically and fulfil this thesis. Furthermore, without the help and enthusiasm of prof. dr. ir. Willem van de Water this thesis would not have been the same. I am really thankful for all the discussions we had and the resulting critical feedback. I am grateful that prof. dr. ir. Jerry Westerweel gave me the opportunity to work on this project. The discussions we had and the research facilities you arranged for me, were of large importance for this research. I would also like to thank Dr. Andrea Sciacchitano for taking the time and being a part of my thesis committee. Furthermore, I would like to thank dr. ir. Mathieu Pourquie for his help and guidance on the CFD simulations. Without the help of Jasper Ruijgrok I would not even have been able to do any experiments, I am really grateful for all your workshop manufacturing and prototyping. I would also like to thank Peter Poot for his help and time during the towing tank experiments.

R. Bazuin
Delft, April 2018

Abstract

During front crawl swimming, water is driven backwards with the limbs. Drag forces generated by the limbs are consequently used for forward propulsion. The hands are responsible for approximately 60% of the generated propulsive forces. Reaching a podium place in competitive swimming is dependent on differences in finishing times smaller than 0.5%. For this reason, investigating the effects of hand configuration on swimming performance is of interest. Configurable properties of the hand are the finger spreading and hand palm cupping. It is argued that a small finger spreading leads to a larger obstruction in the fluid flow compared to closed fingers, resulting in larger generated drag forces. Similarly, a small hand cupping is expected to increase the drag forces in analogy to the drag increase experienced by cupped disks. In this thesis, an experimental investigation is carried out to look into the effects of both finger spreading and hand cupping. Furthermore, CFD simulations are used for the abstract modelling of hands with finger spreading by use of slotted disks.

Towing tank experiments in water are performed to investigate the effects of finger spreading for five full-scale arm models. The research showed that a small finger spreading of 5° can increase the drag coefficient of the hand with 1.7%, in comparison to closed fingers. Larger spreadings were found to influence the drag coefficient disadvantageously, where a 20° finger spreading reduced the drag with 1.5%. The found effects indicate that finishing times can be reduced with 0.3% by using 5° finger spreading instead of 20° spreading.

Wind tunnel experiments are used to look into the effects of hand cupping. Dynamic scaling based on the Reynolds number is used to account for the used air flow. Effects for five full-scale arm models with different hand cuppings were investigated, these have a 5° finger spreading which was found optimal from previous research. It appeared that small rotations around the longitudinal axis of the arm have large influences on the drag coefficient, where a maximum in drag was never found for the hand palm perpendicular to the flow, but with an abducted thumb opposing the flow. The research showed that 6% more drag is generated for a flat hand in comparison to the largest investigated hand cupping. This indicates that finishing times can be reduced with 0.8% by using a flat hand instead of a large hand cupping.

In conclusion, the research found a hand configuration with 5° finger spreading and a flat hand palm optimal for maximizing drag forces. The found effects on finishing times indicate that using this hand configuration can play an important role in reaching podium places during front crawl swimming.

Nomenclature

Acronyms

CFD	Computational Fluid Dynamics	
POA	Point of application of force	

Dimensionless numbers

Fr	Froude number	-
Re	Reynolds number	-
St	Strouhal number	-

Greek Symbols

α	Angle of attack	$^\circ$
β	Porosity	[-]
ϵ	Turbulent dissipation rate	$\mathrm{J\,kg^{-1}\,s^{-1}}$
μ	Dynamic viscosity	$\mathrm{kg\,m^{-1}\,s^{-1}}$
ν	Kinematic viscosity	$\mathrm{m^2\,s^{-1}}$
ω	Specific turbulent dissipation rate	$\mathrm{s^{-1}}$
ϕ	Blockage ratio	-
ρ	Density	$\mathrm{kg\,m^{-3}}$
σ_x	Standard error of the mean	-
τ_w	Wall shear stress	$\mathrm{kg\,m^{-1}\,s^{-2}}$
φ_z	Angle of attack	$^\circ$

Roman Symbols

A	Projected area on a plane perpendicular to the free stream	$\mathrm{m^2}$
$a(t)$	Acceleration	$\mathrm{m^2\,s^{-1}}$
C_D	Drag coefficient	-
C_L	Lift coefficient	-
C_M	Drag moment coefficient	-
D	Characteristic diameter	m
f	Vortex shedding frequency	Hz
F_D	Drag force	N
$F_D(t)$	Instantaneous drag force	N
F_L	Lift force	N

g	Gravitational acceleration	$\mathrm{m\,s^{-2}}$
k	Turbulent kinetic energy	$\mathrm{J\,kg^{-1}}$
L	Characteristic length	m
m_a	Added mass	kg
U	Swimming velocity	$\mathrm{m\,s^{-1}}$
u_*	Wall friction velocity	$\mathrm{m\,s^{-1}}$
V	Flow velocity	$\mathrm{m\,s^{-1}}$
y^+	Dimensionless wall distance	-

Contents

1

Introduction

The 50 meter freestyle swimming for women on the Olympic Games of 2016 in Rio de Janeiro illustrated that differences in finishing times are minimal. The number six finished only 0.12 s behind the number one, on a total swimming time of 24 s. This indicates that even the smallest improvements in swimming performance can be crucial in reaching a podium place. Fundamental research to the fluid dynamics involved in human swimming can lead to a better understanding of the drag and propulsion acting on swimmers. As a result, performance improvements for elite swimmers could be derived. In the past, thorough research has been done both experimentally and numerically on different aspects of swimming hydrodynamics, varying from the hydrodynamics around the complete body of a swimmer to just the orientation of the thumb. During this thesis the effects of hand configuration on propulsive forces in swimming are investigated. All research is performed at constant velocities. Aspects of hand configuration are finger spreading, thumb positioning, cupping of the hand and rotations of the hand. This chapter starts by giving general information on a front crawl swimming stroke. Hereafter fundamental information on drag is presented. Based on this drag, the propulsive aspects within swimming are discussed, with an overview of current literature towards the effects of hand configuration. Finally the objectives of the research are formulated together with an outline of this report.

1.1. Front crawl swimming

Figure 1.1 gives an illustration of a front crawl swimming stroke. As a swimmer moves forward through water its body experiences a drag force. To overcome for this drag, a swimmer generates propulsive forces by driving water backwards with his arms and legs (van Ingen Schenau & Cavanagh, 1990; van Houwelingen et al., 2017). In this way a swimmer uses drag and lift forces acting on its arms and legs for forward propulsion. The swimming velocity U can either be increased by lowering drag acting on the body, or by increasing the propulsive forces generated by the swimmer. The latter is investigated during this thesis by looking into effects of varying the hand configuration.

Four different phases are distinguished during front crawl swimming (Polloreno, 2014), figure 1.1 gives an illustration of the different phases. During the *catch* the hand enters the water, here lift forces play an important role in forward propulsion (van Houwelingen et al., 2017). Then the hand moves underwater in the *pull* phase, this phase is responsible for generating most propulsive forces and uses drag forces for this purpose. The forearm moves perpendicular to the water in a large portion of this phase as shown in figure 1.1. As the hand moves along the body it reaches the water surface again, where it is pulled out of the water in the *exit* phase. Then finally the hand moves above the water surface in the *recovery* phase, such that it comes back in the original catch position. Especially small improvements within the pull phase can have significant influences on the swimming performance, as most propulsive forces are generated during this phase. For this reason it is most interesting to find an optimum hand configuration for the pull phase.

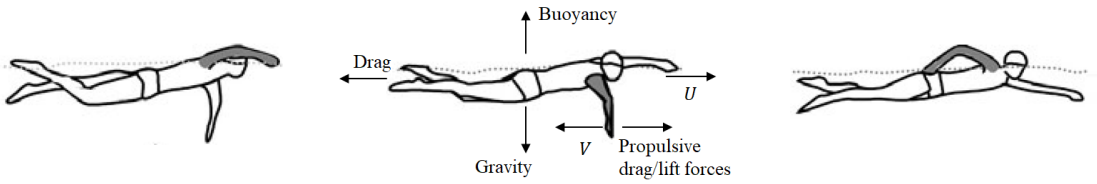

(a) Catch (b) Pull (c) Exit

Figure 1.1: Illustration of the different phases distinguished during a front crawl swimming cycle, with from left to right the *catch*, *pull* and *exit* phases. (b) Illustrates the forces and velocities acting on a swimmer during the pull phase. Propulsive forces can either be drag- or lift-based (van Houwelingen et al., 2017). Modified from Strzala & Tyka (2009).

1.2. Fundamentals of drag

The importance of viscous effects is quantified by the Reynolds number, it signifies the transition of laminar to turbulent flow. The Reynolds number represents the ratio of inertial and viscous forces and is expressed as

$$\mathrm{Re} \equiv \frac{VD}{\nu}. \tag{1.1}$$

Here V is the flow velocity with respect to an object, D is a characteristic diameter and ν the kinematic viscosity of the fluid (White, 2011). Furthermore, the Reynolds number is used for scaling to achieve dynamic similarity for experiments performed in different fluids or at different circumstances. For the purpose of scaling, matching Reynolds are needed while the fluid conditions vary.

Forces are experienced on an object that is exerted to a fluid flow, a drag and lift force are respectively experienced in the streamwise direction and in a direction perpendicular to it. Dimensionless drag and lift coefficients are expressed as

$$C_{D,L} = \frac{F_{D,L}}{\frac{1}{2}\rho V^2 A}, \tag{1.2}$$

where ρ is the fluid density, A is the projected area of the object on a plane perpendicular to the mean flow and $F_{D,L}$ is the drag or lift force (White, 2011). These force coefficients are generally dependent on the Reynolds number and shape of the object. Drag force is often proportional to V^2 for high Reynolds number flows as inertia is dominating ($\mathrm{Re} > 10^4$) (Kundu et al., 2015).

The formulation of the drag coefficient in equation 1.2 only applies to fluid flows at a steady-state. When accelerations take place, an extra component in drag due to added mass arises, which originates from the fluid inertia that surrounds the moving object. In this situation the instantaneous, i.e. time dependent drag force is expressed as

$$F_D(t) = a(t)m_a + \frac{1}{2}A\rho V(t)^2 C_D(V(t)), \tag{1.3}$$

where $a(t)$ is the acceleration, $C_D(V(t))$ the velocity-dependent drag coefficient and m_a the added mass (van Houwelingen et al., 2017).

Distinction in three types of drag is made for an object moving through water, these are viscous drag, pressure drag and wave drag (Marinho et al., 2009). Detailed descriptions of these are given in the next subsections.

1.2.1. Viscous drag

Viscous drag is the fluid resistance associated with viscosity and the formation of boundary layers. These boundary layers cause the fluid flow along the surface of a body to slow down. Viscous drag is predominant for low flow velocities, i.e. $\mathrm{Re} < 1$ (Hoerner, 1965). It depends on the flow velocity, and the wetted surface area and surface characteristics of the body (Marinho et al., 2009). Viscous drag is usually dominant for streamlined bodies, e.g. an airfoil (Nakayama & Boucher, 1998).

1.2.2. Pressure drag

Pressure drag usually dominates for fluid flow around blunt bodies, e.g. circular cylinders, where a wake is formed due to flow separation (Nakayama & Boucher, 1998). In the wake, velocity and pressure both decrease

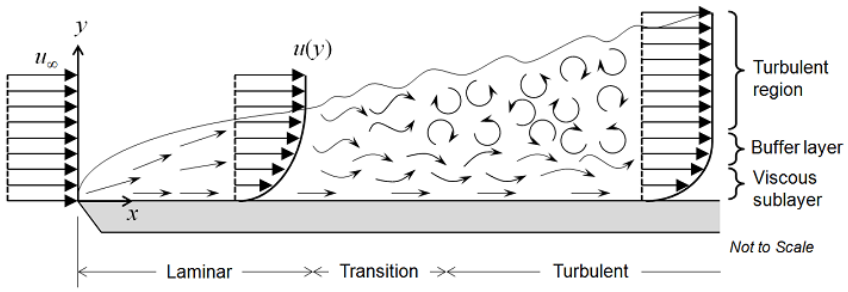

Figure 1.2: Growth of a boundary layer on a flat plate including transition to turbulence. Different wall layers distinguished in the turbulent boundary layer; a viscous sublayer, a buffer layer and a turbulent region, respectively (Frei, 2017).

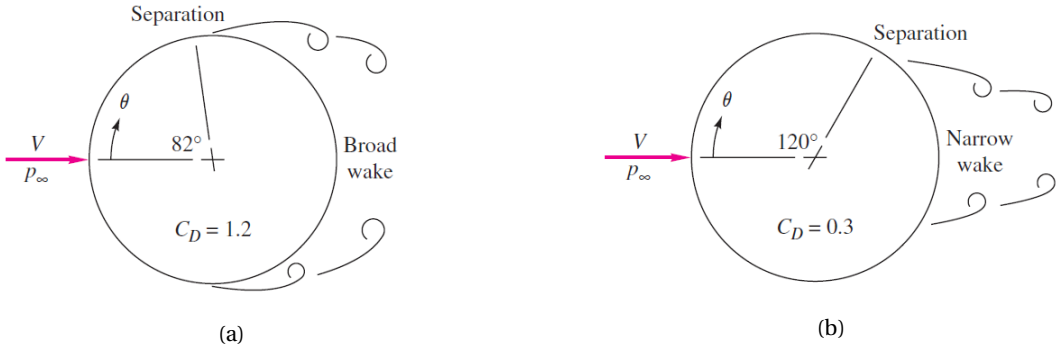

Figure 1.3: Flow pas a circular cylinder: (a) laminar separation (10^3 <Re < $3 \cdot 10^5$); (b) turbulent separation (Re > $3 \cdot 10^5$), where the separation point moves downstream and a narrower wake is formed resulting in lower drag (White, 2011).

relatively to the free stream. Pressure drag is introduced due to the pressure difference over the front and rear of the body. Pressure drag depends on the flow velocity and cross-sectional area of the body (Marinho et al., 2009).

The drag coefficient C_D is usually nearly constant at high Reynolds numbers (Re > 10^4), however for circular cylinders a strong decrease in drag coefficient called the drag crisis is found. For smooth circular cylinders the drag crisis is found for $3 \cdot 10^5$ < Re < $3 \cdot 10^6$. As shown in figure 1.4, a sudden dip in C_D from 1.2 to 0.3 is observed inside the drag crisis of a smooth cylinder. This decrease in C_D is a result of boundary layer transition (Kundu et al., 2015). Initially a thin laminar boundary layer grows as fluid flows downstream. Then transition to a faster growing turbulent boundary layer takes place for higher Reynolds numbers (Kundu et al., 2015). An illustration of such boundary layer transition along a flat plate is given in figure 1.2. Different regions are distinguished inside the turbulent boundary layer. A viscous sublayer is found next to the wall where viscous stresses are dominating. Further away from the wall in the buffer layer, turbulence stresses start to dominate over viscous stresses. The buffer layer eventually connects to a turbulent region where viscous stresses are negligible compared to turbulence stresses (Frei, 2017). Depending on the shape of an object, the boundary layer starts decelerating at a certain point downstream as a result of adverse pressure gradients. Here reverse flow is observed, which results in flow separating from the wall. Flow separation is responsible for the formation of a wake behind an object, figure 1.3 gives an illustration of flow separation around a circular cylinder. Large drag is observed for a fully laminar boundary layer where a broad wake is formed, this wake can be completely turbulent (Kundu et al., 2015). Transition to turbulence delays flow separation as a turbulent boundary layer is more capable of withstanding adverse pressure gradients (Kundu et al., 2015). This leads to the separation point moving downstream, such that a narrower wake and lower drag are observed as shown in figure 1.3b.

Figure 1.4 also illustrates the effects of wall roughness on the drag coefficient for a circular cylinder. Wall roughness can accelerate the boundary layer transition, such that a drag crisis is observed at lower Reynolds numbers. Figure 1.4 shows that the decrease in drag inside the drag crisis becomes smaller for a rough surface compared to a smooth surface. Effects of wall roughness generally come into play when the roughness height

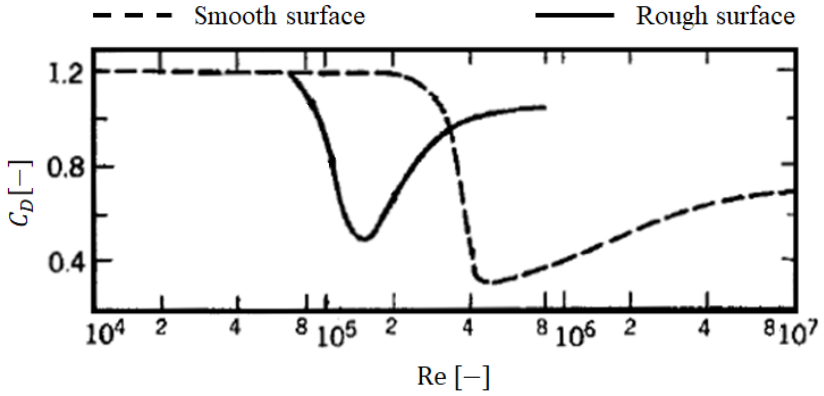

Figure 1.4: Measured drag coefficient for a circular cylinder with effects of wall roughness. For the smooth surface, the drag crisis for $3 \cdot 10^5 < \text{Re} < 3 \cdot 10^6$ is due to the transition of the boundary layer to turbulence and the consequent downstream movement of the point of separation (Kundu et al., 2015). The surface roughness shifts the occurrence of a drag crisis to lower Reynolds numbers. Modified from Isyumov (2015).

h of the surface is larger than the thickness of the viscous sublayer, meaning that the Reynolds number $\text{Re}_* = hu_*/\nu >> 1$ (Nieuwstadt et al., 2016). Here u_* is the friction velocity that gives information on the velocity in the boundary layer.

1.2.3. Wave drag

An object that pierces the free water surface forms surface waves in its wake as it moves relative to a fluid. The energy required for this wave formation introduces an extra component of drag, called wave drag (Hoerner, 1965). The Froude number is a dimensionless quantity that gives similarity rules for free-surface flows (e.g. surface waves). It is often used to describe different flow regimes in which wave drag is of importance. The Froude number represents the ratio of inertial to gravitational forces and is expressed as

$$\text{Fr} \equiv \frac{V}{\sqrt{gL}}, \tag{1.4}$$

where g is the gravitational acceleration and L is a characteristic length scale, usually taken as the length of the object at the free-surface in the streamwise direction. Koo et al. (2014) used large eddy simulations to look into the effects of interface piercing circular cylinders for varying Reynolds and Froude numbers. Figure 1.5a and 1.5b show the wave formation at Fr = 0.44 and Fr = 1.24, respectively. For increasing Fr an increase in surface deformations is observed, as water is piling up at the front, and a hollow forms behind the object. Furthermore, for increasing Froude number a broader wake is formed consisting of larger waves in comparison to lower Fr.

Figure 1.5c presents the drag coefficients for interface piercing circular cylinders as function of Froude number (Hoerner, 1965). For $\text{Fr} \to 0$ the water surface has the effect of a solid ceiling, no surface deformations are observed, such that only viscous drag and pressure drag are experienced. An additional wave drag component is observed when the Froude number increases, where a maximum is found for $\text{Fr} \approx 1$. As Fr increases further the waves produced by the interface penetrating cylinder break up. Water piling up at the front of the cylinder moves upwards and sidewards such that water sprays in the air. This results in a decrease in drag coefficient that becomes asymptotically stable for large Fr.

1.3. Drag in swimming

A swimmer uses drag forces acting on its limbs for forward propulsion. Around 85-90% of propulsive forces are generated by the arms, where the hand has a 2.5 times bigger contribution to the propulsion than the forearm (van Houwelingen et al., 2017; Bilinauskaite et al., 2013). The large contribution of the hand makes it interesting to look into the effects of hand configuration on propulsive forces in swimming. As a hand has no streamlined shape, contributions of viscous drag to the propulsion in swimming are small.

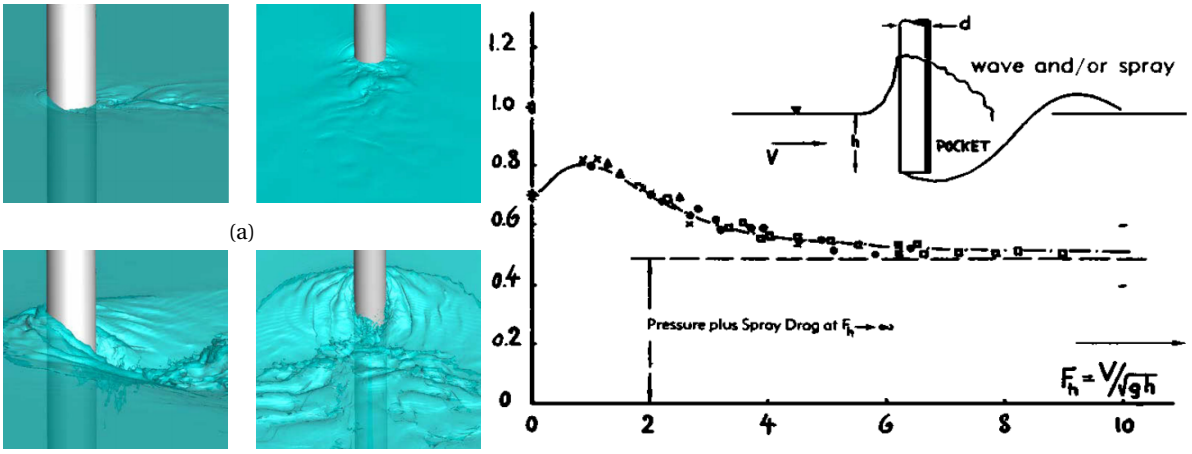

Figure 1.5: For an interface piercing circular cylinder: (a) and (b) show the wave field at Fr = 0.44 and Fr = 1.24, respectively. The first column gives a side view and the second column shows the wake region (Koo et al., 2014); (c) shows the effect of drag coefficient for varying Froude number, modified from Hoerner (1965).

Many applications prefer the delay of flow separation as it decreases drag, however along the arm of a swimmer it is the exact opposite as it needs drag maximization. Geometric similarity between a forearm and a circular cylinder exists. For a forearm (as well the hand palm) with width D = 0.1 m and stroke velocity V = 2 ms^{-1} the Reynolds number is Re $\sim 2 \cdot 10^5$. Theoretically only a laminar boundary layer grows around a cylindrically shaped forearm for this Reynolds number, however surface roughness and the forearm not being perfectly cylindrically shaped can (de)accelerate the boundary layer transition (Hoerner, 1965; Nieuwstadt et al., 2016). In this way effects of a drag crisis can be experienced around the forearm at Reynolds numbers observed in front crawl swimming.

Van Houwelingen et al. (2017) gives an extensive literature review on the aspects of hand configuration on the hydrodynamics in swimming. Based on literature review, effects of finger spreading, thumb position, hand orientation and Reynolds number dependency on drag and lift around the hand of a swimmer are discussed in this section. Furthermore, the velocity path of hand during front crawl swimming is described.

1.3.1. Angle of attack

During a swimming stroke, the arm can rotate along all three Cartesian axes, these orientations play an important role in experienced drag and lift forces. Especially effects of rotations around the x-axis as shown in figure 1.6a are extensively investigated, this rotation is defined as the angle of attack α. An overview of effects on drag and lift coefficients for varying angle of attack is given by van Houwelingen et al. (2017), here a collection of both numerical and experimental work is presented. Effects on drag coefficient C_D from experimental studies are presented in figure 1.6b, while numerical work shows similar results. All studies obtained a clear parabola with a maximum drag coefficient around $\alpha = 90°$, which is the position that has the hand palm perpendicular to the flow and maximizes the projected area. Note that large differences in drag coefficient occur in figure 1.6a for the work of different researchers. This is due to the differences in investigated arm models and differences in definitions. Some researchers looked at only a hand, while others had a forearm attached to the hand. Furthermore, different definitions for the area A in equation 1.2 were used, both the wetted surface area and the projected area.

All studies show that $C_L \approx 0$ for $\alpha = 90°$, where C_L becomes positive for a leading thumb and negative for a leading little finger. For most orientations lift has lower values than drag. Lift force can be used for propulsion by use of so called sculling motions. However it is argued that a straight pull that uses only drag for propulsion is more effective (van Houwelingen et al., 2016), hence for the present research it is mostly relevant to look at effects of drag for increasing propulsion in swimming.

1.3.2. Finger spreading

Schleihauf (1979) performed extensive research on the hydrodynamics of the hand of a swimmer, among which the effect of finger spacing was investigated. Steady state experiments were performed in an open-water channel for different angles of attack α. Schleihauf (1979) found that closed fingers lead to a highest

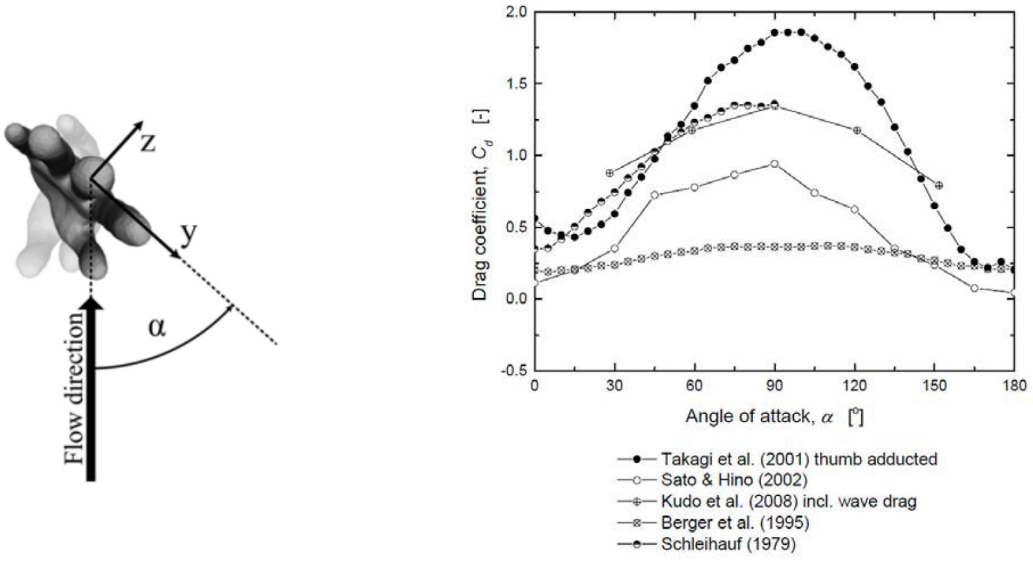

(a) (b)

Figure 1.6: (a) Gives the definition of angle of attack α, where the thumb is leading for $\alpha = 0-90°$ and for $\alpha = 90°$ the hand palm is perpendicular to the flow. (b) Presents an overview of found drag coefficients for varying angles of attack based on experimental work (van Houwelingen et al., 2017).

drag coefficient, independent of α. For 6.35 mm spacing a decrease in drag coefficient of 11% compared to closed fingers was observed while $\alpha = 90°$ (hand palm perpendicular to direction of motion), and a decrease of 19% for 12.7 mm spacing.

Minetti et al. (2009) performed Computational Fluid Dynamics (CFD) simulations on hands with eight different finger spacings and found that C_D is independent of Reynolds number and has its maximum at 8 mm spreading, giving ~8.8% more drag than for closed fingers. It is observed to have a 20% larger wake region at the optimal spacing. Which indicates that more energy is extracted from the flow and thus the pressure differential is larger over the hand leading to a higher propulsion.

Marinho et al. (2010) performed CFD simulations in ANSYS Fluent for hands with different finger spacings based on the hand of an Olympic swimmer. For simulations at 2 $\mathrm{m\,s^{-1}}$ in water it was found that a 3.2 mm spacing gave an increase in drag of around 13% compared to a closed hand, while a 6.4 mm spread gave a decrease of around 7%.

A more fundamental description of finger spreading is given by Lorente et al. (2012), where 2D CFD simulations around a row of cylinders with different spacings were performed. The spaced cylinders give a representation of finger spreading. Effects of Reynolds numbers in the range $20 < \mathrm{Re} < 100$ were investigated. For this range of Reynolds numbers a finger spacing of 0.2 - 0.4 times the diameter of the cylinder is found optimal, such that for Re = 100 the drag increases with 18%. Note that the Reynolds numbers around the fingers of a swimmer are orders of magnitude higher, with a finger thickness $D = 0.01$ m and $V = 2\ \mathrm{m\,s^{-1}}$ the Reynolds number is $\mathrm{Re} \sim 10^4$ around a finger.

Bilinauskaite et al. (2013) performed CFD simulations at different velocities for four hand models (spread/closed fingers and abducted/adducted thumbs). They did find an increase in drag coefficient for spread fingers, both for abducted and adducted thumbs.

In the research of van Houwelingen et al. (2016), five full scale forearm/hand models with different finger spreadings were investigated. They performed both experiments (wind tunnel) and simulations (immersed boundary method) on the same five models. Drag coefficients C_D and moment coefficients C_M were determined. Their numerical work shows a local maximum in $C_{D,M}$ for 10° and 20° finger spreading. Their numerical work found maxima in C_D and C_M for respectively 5° and 10° finger spreading. Increases in $C_{D,M}$ of 2% and 5% with respect to the closed fingers were obtained for the experimental and numerical work, respectively.

Westerweel et al. (2016) formulated a theoretical concept based on the actuator disc model to describe the drag force as function of finger spreading. A hand with finger spreading is here described by four parallel cylinders with length l, diameter D and a spacing d. Similarly to an actuator disc, streamlines for a flow

around the four cylinders start expanding, where the degree of expansion depends on d/D. Streamline expansion results in a pressure decrease in the wake and hence to propulsion. A scaling argument for the drag force based on the actuator disc principle is derived as

$$F_D \sim \rho V \cdot 4lD \cdot \left[1 + \frac{3d}{4D}\right]\left[1 - \sqrt{\frac{d}{D}} \cdot \frac{d/D}{1 + d/D}\right]. \tag{1.5}$$

Similarly to research on realistic hand models it is found that small gaps can be beneficial for maximizing drag force. A maximum increase in drag force of 4% compared to a closed hand is found for $d/D = 0.3$, disadvantageous effects in F_D arise for $d/D > 0.7$.

1.3.3. Thumb position

Several authors looked into the effects of thumb positioning, where adducted, abducted and partially abducted thumbs are used (van Houwelingen et al., 2017). Here an abducted thumb moves away from the hand and an adducted thumb touches the hand. Schleihauf (1979) found that abducted thumbs result in more lift for small angles of attack α, while for larger angles a partially abducted thumb is favourable. Takagi et al. (2001) showed that thumb abduction for a leading thumb leads to larger lift forces, while drag forces for abducted and adducted thumbs are similar. For a leading little finger an adducted thumb gives both larger drag and lift forces. Bilinauskaite et al. (2013) showed that thumb adduction results in largest drag during the pull phase of a swimming stroke. Here spreading the finger simultaneously leads to even larger drag forces.

All these studies considered hand models with no forearm attached to it, hence the effects of interaction between the thumb and forearm remains unknown. But the studies agree that thumb abduction can be beneficial in the parts of the swimming stroke where lift is important for forward propulsion, while thumb adduction is favourable for maximizing drag.

1.3.4. Reynolds number dependency

Previous research looked into the effects on $C_{D,L}$ for varying Reynolds numbers while maintaining the angle of attack at $\alpha = 90°$. Van Houwelingen et al. (2017) concluded that drag and lift coefficients are independent of Reynolds number for $2 \cdot 10^4 < \mathrm{Re} < 4 \cdot 10^5$. A drag crisis around the cylindrically shaped forearm is expected, therefore it is unlikely that $C_{D,L}$ is independent of all Reynolds numbers. It is expected that Reynolds number independences found for numerical work around arm models are an artefact of using too coarse grids, such that the turbulent boundary layers cannot be fully resolved (van Houwelingen et al., 2017).

1.3.5. Front crawl velocity path

Van Houwelingen captured the path of motion of the hand during a front crawl swimming stroke. For this purpose a light-emitting diode connected to the hand of a swimmer was tracked with a camera. The corresponding velocity path of the hand is shown in figure 1.7. Those hand velocities correspond to the velocity V in figure 1.1. Positive velocities correspond to the underwater pull phase and negative velocities represent the recovery phase. Figure 1.7 shows that the hand is moving at a velocity from 0 - 2 $\mathrm{m\,s^{-1}}$ during the pull phase. The drag force is proportional to the squared velocity for high Reynolds number flows. Then a velocity that is associated with the average drag force $\bar{F}_D$ that is generated during the pull phase is given as

$$V_{\bar{F}_D} = \sqrt{\frac{\int_{t_1}^{t_2} V(t)^2 \mathrm{d}t}{t_2 - t_1}}, \tag{1.6}$$

where t_2 - t_1 correspond to the duration of the pull phase. Accordingly it is found for the data of figure 1.7 that $V_{\bar{F}_D} = 1.5\ \mathrm{m\,s^{-1}}$ during the pull phase.

1.4. Wind tunnel fundamentals

This research uses wind tunnel experiments to look into the effects of hand configuration. This section describes some important fundamentals of wind tunnel testing, e.g. effects of flow induced hysteresis and blockage effects.

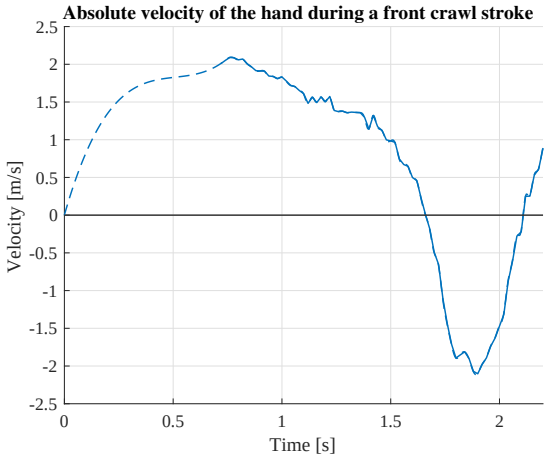

Figure 1.7: The velocity path of the hand during a front crawl stroke. Negative velocities indicate the underwater pulling motion, while positive velocities indicate motions above the water surface. Note that the graph contains dashed regions, here the light-emitting diode was out of sight for the camera, therefore the missing data is interpolated.

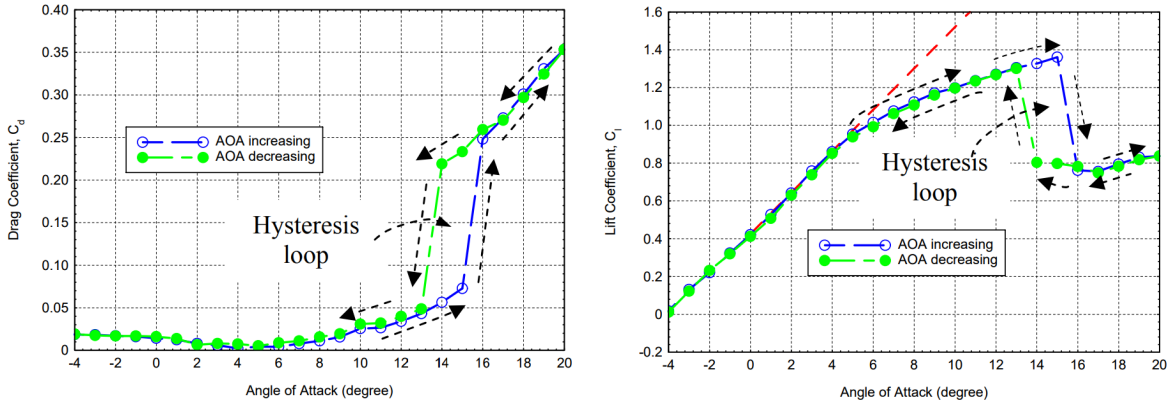

(a) Drag coefficient

(b) Lift coefficient

Figure 1.8: Drag and lift coefficient for an airfoil for increasing and decreasing angle of attack (AOA). A hysteresis loop is observed around the stall angle. From Yang et al. (2008).

1.4.1. Flow induced hysteresis

Hysteresis is the dependence of the state of a system on its history. Effects of hysteresis can be observed in a fluid flow when experiments are done for varying angles of attack (Yang et al., 2008). Figure 1.8 shows the variation of drag and lift coefficients for an airfoil as function of the angle of attack. For small angles of attack the airfoil can be considered a streamlined body such that the flow nicely attaches to the body and low drag force is experienced. As the angle of attack increases (at $\alpha = 16°$) a phenomenon called stall is observed, where a sudden jump in C_D and drop in C_L occur, at this point the flow starts separating from the body and a wide disturbed wake is formed (Yang et al., 2008). As the angle of attack decreases again, it can be observed that stall appears at a lower angle of attack than before (at $\alpha = 14°$), thus the flow starts reattaching at a different angle of attack than at which separation started initially (Yang et al., 2008). This phenomenon is demonstrated by the hysteresis loop in figure 1.8.

1.4.2. Blockage effects

During wind tunnel experiments, air flows past a bluff body that is bounded by rigid walls, and introduces so-called blockage effects. The rigid boundaries prevent a free lateral displacement of the airflow by the body, leading to an increase in the free-stream velocity (Maskell, 1963). As the free-stream velocity increases, larger drag forces are experienced on a body according to equation 1.2. Correction methods are developed to account for these blockage effects (Maskell, 1963). Blockage (ϕ) is defined as the ratio of the projected area of the model and the cross sectional area of the wind tunnel's test section. Barlow et al. (1999) suggests to not

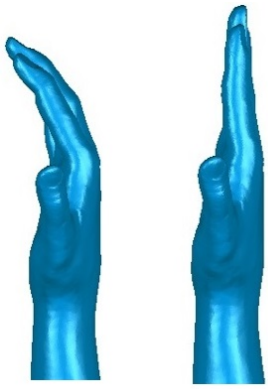

Figure 1.9: Illustration of hand cupping the hand. On on the left a cupped hand is shown, with a curvature in the hand palm and fingers. On the right a flat hand is illustrated.

use blockage correction methods for $\phi < 5\%$ based on the lack of confidence in these methods.

1.5. Research objectives

The current research is exploring the effects of hand cupping on propulsive forces. Also the effects of varying the angle of attack and Reynolds number are investigated. The next subsections give motivations for these research topics.

1.5.1. Hand cupping

Many authors looked into the effects of finger spreading and thumb positioning in swimming, while this is not the only variable in hand configuration. Cupped hands are formed by having a curvature in the fingers and hand palm, figure 1.9 gives an illustration of such cupped hand. A literature study did not show that effects of hand cupping were previously investigated, although there are arguments for hand cupping leading to an increase in drag. This was derived from the experimental data on cupped disks from Hoerner (1965) shown in figure 1.10a. Here the effects on drag coefficient are presented for varying ratios of disk height to thickness (h/d). It shows an increase from $C_D = 1.17$ for a flat disk to $C_D = 1.41$ for a hemispherical shaped disk, where $10^5 < \text{Re} < 10^6$. A hand with its fingers in a cupped shape has a geometrical similarity to a cupped disk. Therefore it is expected that similar effects in drag coefficient are arising for cupped hands.

Although the data from figure 1.10a shows an increase in drag coefficient, it does not take into account the reduction in frontal projected area as h/d increases. Therefore it is more interesting to look at the effect of $C_D A$ as a function of h/d, since this quantity needs maximization to maximize the drag force. Figure 1.10b shows the relation between $C_D A$ and h/d. A maximum of $C_D A = 1.21$ is found for $h/d = 0.08$, giving an increase in $C_D A \sim 3\%$ compared to a flat disk. This gives reason to expect an increase in drag when a swimmer cups his hands.

1.5.2. Angle of attack

Previous research looked into the effects of varying the angle of attack α. Takagi et al. (2001) was the only who looked into the effects of varying the angle of attack for different hand models, with respectively an abducted and adducted thumb. As the two hand models give different effects on C_D for varying α it is expected that different finger spreadings or hand cuppings also respond differently to varied angles of attack. Hence it is of interest to perform experiments for various hand configurations at varying angles of attack.

1.5.3. Reynolds number dependencies

Previous research found Reynolds number independent effects on $C_{D,L}$ for hand models with and without forearm attached to it. It is argued that the presence of a forearm is likely to introduce effects of Reynolds number dependency. Because of the occurrence of a drag crisis around a cylindrically shaped forearm. Furthermore, Reynolds number effects are not necessarily equal for different hand configurations and angles of attack. This makes it interesting to explore the effects of Reynolds numbers during this research.

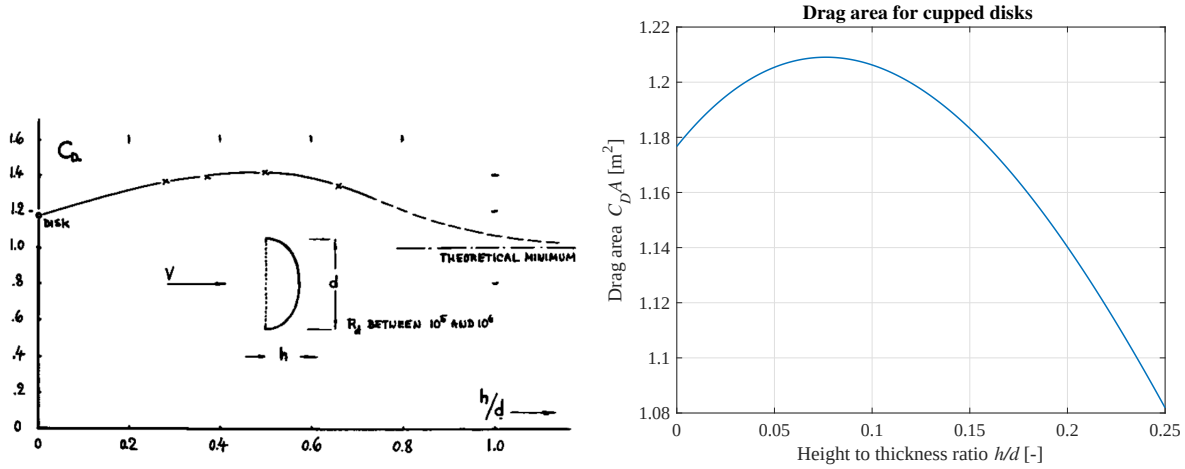

(a) (b)

Figure 1.10: (a) Presents the drag coefficient of cupped disks as a function of their height to thickness ratio h/d for Re between $10^5 - 10^6$ (Hoerner, 1965). (b) Shows C_DA as a function of h/d based on the data from Hoerner (1965).

1.6. Outline of the report

For this thesis, the effects of hand configuration on the propulsive forces in swimming are investigated. In chapter 2 the effects of finger spreading are investigated by means of towing tank experiments. Chapter 3 explores the modelling of simplified shapes that can describe hands with finger spreading, CFD simulations are carried out to look into the effects of drag for those simplified shapes. Chapters 4 and 5 look into the effects of hand cupping, wind tunnel experiments are used for this investigation. Finally, chapter 6 draws conclusions towards the effects of hand configuration. Here the found effects of hand configuration are applied to competitive swimming to investigate possible performance enhancements.

2

Finger spreading: towing tank experiments

Effects of fingers spreading in swimming have extensively been researched. Van Houwelingen et al. (2016) did both CFD simulations and wind tunnel experiments on one set of arm models with varying finger spreading. This chapter describes experiments done with the same arm models, performed in a towing tank facility at TU Delft. Here experiments are carried out in water with the presence of a free surface, in contrary to the wind tunnel experiments of van Houwelingen et al. (2016). This chapter starts with a description of the used arm models and experimental setup. Hereafter the experimental methods and the obtained results are discussed. Finally conclusions on the effects of finger spreading are drawn.

2.1. Hand models

Figure 2.1 shows five configurations of finger spreading as used by van Houwelingen et al. (2016), here the forearm is not visualized but it is equal to that in figure 4.1. Those models are created by use of 3D-printing, with a 0.002 m wall thickness and a hollow inside. Each model has a hand palm width, arm length and projected frontal area A of 0.096 m, 0.507 m and 0.042 m^2, respectively. Physically, the skin of a hand can extend and compress when fingers are spread. These effects are not taken into account for the projected areas of the five arm models from van Houwelingen et al. (2016), i.e. all arm models have an equal projected area A.

2.2. Experimental setup

This section gives information on the characteristics of the used towing tank and measurement of forces acting on the arm models as they are towed through the water.

2.2.1. Towing tank characteristics

The idea of a towing tank came from the naval architect William Froude, who developed the facility to perform experiments on scaled ship hulls. A towing tank available at the department of Maritime and Transport Technology at TU Delft is used. This towing tank is illustrated in figure 2.2, it consists of a large water filled basin made out of concrete. It has a length of 85.00 m, width of 2.75 m and maximum water depth of 1.25 m. A towing carriage is mounted on two rails above the water basin and can move in its x-direction by means of electric power drives. The facility is designed in such a way that vibrations transmitted from external sources

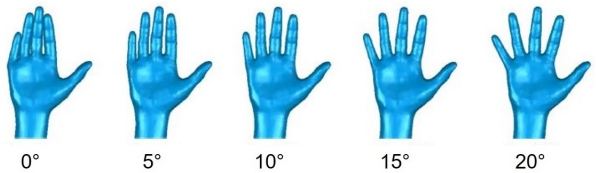

Figure 2.1: The finger spreads are 0°, 5°, 10°, 15° and 20°. The angle of each finger is defined as the angle relative to the 0° position. For example, for the 20° model the index finger and ring finger are positioned 20° outward compared to their position in the 0° model, whereas the little finger is bent 40° outward. These angles roughly correspond to a spacing between the finger tip side edges of 0, 7.5, 15, 20 and 25 - 30 mm, respectively (van Houwelingen et al., 2016).

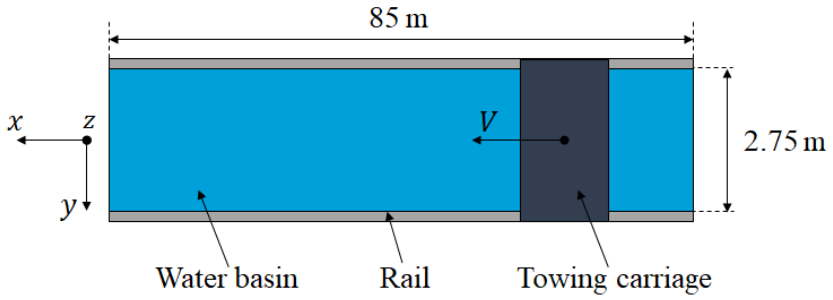

Figure 2.2: Illustration of the towing tank facility in a top view. Here the water basin and the corresponding dimensions are given. The towing carriage moves with velocity V on top of two rails in positive x-direction.

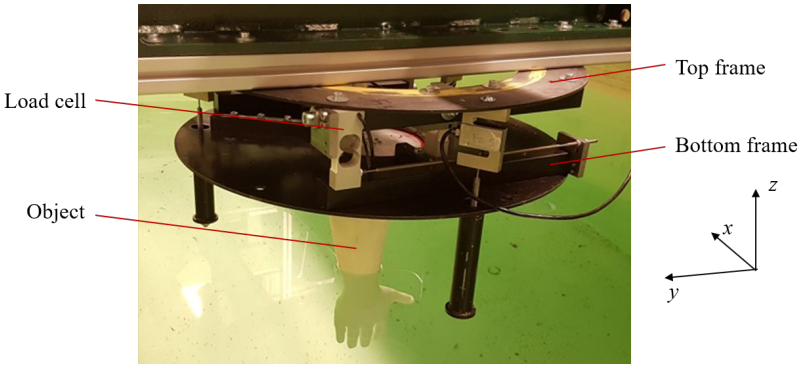

Figure 2.3: Photo of the used six-component measurement system and the corresponding coordinate system, here the towing carriage moves in the positive x-direction with velocity V.

to the towing tank are minimized. The towing carriage is limited to a maximum velocity of 2.00 $\mathrm{m\,s^{-1}}$ and an acceleration of 0.250 $\mathrm{m\,s^{-2}}$ (van 't Veer, 2018).

2.2.2. Force measuring system

The arm models are connected to the towing carriage, drag and lift are experienced on the arm models as they are towed through the water basin. The magnitude of these forces and moments are determined with the six-component measurement system that is shown in figure 2.3. The measurement system consists of two frames interconnected by six load cells, with the arm models mounted to the bottom frame. The top frame is on one side connected to the towing carriage and at the other side to the six load cells. In this way forces and moments acting on the objects lead to small motions and rotations of the bottom frame, this causes deformations in the strain gauges on the load cells which can be translated into forces. A right-handed Cartesian coordinate system is used with its origin at the centre between the top and bottom frame. The x, y, z-axes are respectively directed downstream, transverse and upward. Appendix A gives a detailed description of the characteristics of the force measuring system, where the measuring accuracies are presented in figure A.2. Drag forces are measured more accurately at higher velocities, with an accuracy <0.5% for towing velocities $V > 1\ \mathrm{m\,s^{-1}}$. Drag moments are measured more accurately at lower velocities, with an accuracy $\approx 1\%$ for $V < 1\ \mathrm{m\,s^{-1}}$

2.3. Experimental methods

It is the purpose to study the influence of finger spreading on drag of the hand. It is assumed that interference exists between flow generated by the fingers and only a part of the forearm. This makes it unnecessary to

Table 2.1: Overview of the investigated finger spreadings and towing velocities. Towing velocities correspond to Reynolds numbers ranging from $0.24 \cdot 10^5 < \mathrm{Re} < 1.90 \cdot 10^5$.

Finger spreading	[°]	0, 5, 10, 15, 20
Velocity	[$\mathrm{m\,s^{-1}}$]	0.250, 0.500, 0.750, 0.875, 1.000, 1.125, 1.250, 1.500, 1.750, 2.000

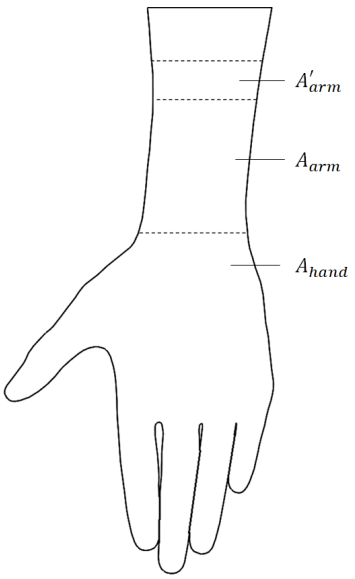

Figure 2.4: Distinction in the difference parts of the immersed arm models, with a contribution of the hand and forearm, and an additional forearm contribution due to water level variations. $A_{hand} = 0.018$ m^2, $A_{arm} = 0.0067$ m^2 and $A'_{arm} = \pm 0.000067$ m^2.

fully immerse the arm models. The arm models are chosen to immerse for 0.31 m, such that a quarter of the forearm is under water. In this way forces acting on the models are reduced, reducing the risks of mechanical failure.

Table 2.1 gives an overview of the investigated towing velocities, these correspond to $0.24 \cdot 10^5 < \text{Re} < 1.90 \cdot 10^5$. Effects of random errors are taken into account by performing experiments at each towing velocity three times for all finger spreadings from table 2.1. Furthermore, arm models are remounted during the experiments, such that effects of the alignment of the arm models are taken into account. Also experiments take place in a random order of towing velocities.

Significant temperature variations were observed during the experimental campaign, varying from 17 - 19°C. By measuring the temperature at the beginning, middle and end of each measuring day those variations are tracked. For water, viscosity has a notable dependence on temperature, such that $\nu(17°\text{C})/\nu(19°\text{C}) = 1.05$. These changes in viscosity are taken into account by the Reynolds number from equation 1.1, used as a non-dimensional quantity for comparing experiments performed at different towing velocities and water temperatures. As a result of vaporization, the water level experiences daily variations; the level was measured three times per day to track the variations. Maximum water level variations of ± 0.001 m were observed. For the drag force F_D from equation 1.2, a distinction in drag coming from the arm and the hand can be made, such that

$$F_D = \frac{1}{2}\rho V^2 \left(A_{hand} C_{D_{hand}} + A_{arm} C_{D_{arm}} + A'_{arm} C_{D_{arm}} \right). \tag{2.1}$$

Here the subscripts *hand* and *arm* correspond to the immersed parts of respectively the hand and forearm, as illustrated in figure 2.4. Variations in the water level result in an additional forearm immersion A'_{arm}. The area $A_{hand} = 0.018$ m^2, $A_{arm} = 0.0067$ m^2 and A'_{arm} varies with ± 0.000067 due to the water level variations. Takagi et al. (2001) found that the drag coefficient of the hand $C_{D_{hand}} \approx 1.75$. As the forearm is roughly cylindrically shaped, a drag coefficient $C_{D_{arm}} \approx 0.64$ is expected (White, 2011). Accordingly, the small water level variations of ±0.001 m lead to deviations in the drag force F_D of ±0.15%. For further experiments, corrections to the projected area A are applied to account for the water level variations.

Tested models

A variety of experiments are carried out in the towing facility, below the different cases are described.

- **Circular cylinder:** experiments are done for a circular cylinder as validation of the used force measuring system. For a circular cylinder, the time-averaged lift force $F_y = 0$. In this way, experiments on the cylinder are used to properly align the force measuring system such that $F_y \approx 0$ is reached. The force

measuring system is finally aligned with an accuracy of 2°. Furthermore, the circular cylinder is used to look into the effects of surface piercing that were described in subsection 1.2.3. The used circular cylinder has a 0.08 m diameter and 0.31 m immersion depth that are similar to that of the arm models; its PVC surface is considered hydrodynamically smooth.

- **Finger spreading:** experiments are done for the five full scale arm models from van Houwelingen et al. (2016) that have 0°, 5°, 10°, 15° and 20° finger spreading. The hand palm is always held perpendicular to the towing direction (angle of attack α = 90°). Experiments are repeated three times to take effects of random errors into account. These experiments are considered the main experiments to obtain insight in the effects of finger spreading.
- **Variation of immersion depth:** experiments are done for the arm models with 5° and 10° finger spreading at a larger immersion depth, 0.34 m instead of 0.31 m. In this way the effects of immersion depth are investigated. This is used to validate the assumption that the flow around the fingers only interferes with a quarter of the forearm.

Data acquisition
A measurement amplifier from Peekel Instruments (Type: PICAS 600) is used to amplify the output voltages from the load cells. Measuring sensitivities of 49.4, 20.3 and 145 mV/N are used for the load cells in x-, y- and z-direction, respectively. An analog filtering system built-in the amplifier has been used. The signals are digitized for further processing in a LabView programme. In this programme, voltages are converted to forces by means of calibration factors. Calibrations factors for each load cell were determined by applying multiple known forces to them. A sampling frequency of 1000 Hz is used for the experiments. Depending on the towing velocity, sampling times in the range of 18 - 50 s were used, where a higher towing velocity results in less sampling time. As part of a calibration procedure the forces acting on the arm models at rest are measured, whereafter these forces are subtracted from the forces measured during the towing experiments.

2.4. Results and discussion

In this section the results following from the towing tank experiments are presented and discussed. At first results for the circular cylinder are discussed where comparisons to literature are made. Hereafter, results for the the five 3D-printed arm models are discussed in detail, where the reliability of the measurements is investigated. Finally, the effects of immersion depth for the arm models are investigated.

2.4.1. Circular cylinder

Figure 2.5 gives an overview of the drag and lift coefficients found for the circular cylinder, presented as both a function of Reynolds number and Froude number. In similarity to figure 1.5c, a parabolic shape in C_D is observed with its maximum around Fr = 1. The determined drag coefficient is of the same magnitude as shown was in figure 1.5c. As it concerns a hydrodynamically smooth cylinder, C_D is expected to be constant for the investigated range of Reynolds numbers, that is with the absence of a free water surface. Hence it can be concluded that the found behaviour of drag coefficients is purely an effect of the free-surface deformations.

Fluid flow around a circular cylinder is characterized by oscillating flow patterns. Vortices are shed from a circular cylinder as part of the flow separation, this results in an oscillating lift force F_L. Vortex shedding around circular cylinders occurs in the range $10^2 < \mathrm{Re} < 10^7$ (White, 2011). The oscillating flow mechanisms are described by the Strouhal number

$$\mathrm{St} \equiv \frac{fD}{V}, \tag{2.2}$$

here f is the vortex shedding frequency, D is a characteristic diameter and V is the flow velocity. For circular cylinders St ≈ 0.21 for the Reynolds numbers range used in figure 2.5 (White, 2011). This indicates that vortices have shedding timescales $1/f$ in the range of 0.20 - 1.5 s. The used sampling times were in the range of 18 - 50 s. The shedding timescales are small compared to the sampling times. This indicates that large amounts of vortices are shed during the towing experiments, which should result in a time-averaged lift coefficient $C_L = 0$. However, figure 2.5 shows that $C_L \neq 0$, this is assigned to the suboptimal alignment of the force measuring system. Based on $C_{D,L}$ from figure 2.5 it is found that the alignment is approximately 2° off. Alignment inaccuracies will be taken into account for the measurements around the arm models.

Figure 2.6 gives a presentation of the wake around an arm model as it is was observed during the experiments, similar effects were observed for the circular cylinder. Similar to the results shown in figure 1.5a and

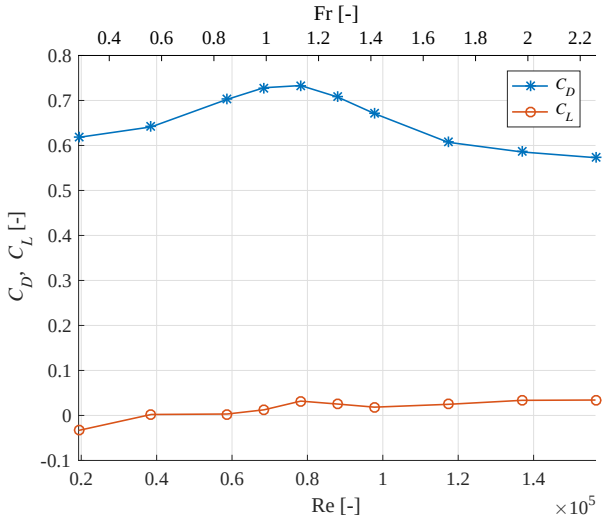

Figure 2.5: Drag and lift coefficients for a circular cylinder as function of Reynolds and Froude numbers.

figure 1.5b, it is observed that for low Froude numbers a narrow wake is formed with little water piling up at the front of the object. The wake is broadening directly behind the object. At larger Froude numbers water is piling up at the front of the object. Initially a large, narrow hollow is formed in the wake of the object, resulting in a large standing wave. Only after this wave the wake becomes broader, with its width increasing far beyond that at low Froude numbers.

2.4.2. Finger spreading

In this subsection the results from experiments with the five arm models are presented. Experiments are done at the towing velocities from table 2.1. Figure 2.7a - 2.7b present force coefficients as a function of Reynolds number. The mean value of the independently done experiments are presented, with the corresponding error bars included. Errors are expressed as the standard error of the mean, given as $\sigma_x = \sigma/\sqrt{n}$, here σ is the standard deviation and n is the sample size. For $C_{D,M}$ it appears that errors at the lowest Reynolds numbers are relatively large, ≈0.4% of the mean value. Errors are considered negligible at higher Reynolds numbers as they are ≈0.05% of the mean value. This indicates that the influence of random errors due to for example fluctuations in the fluid flow, dents in the towing tank rail and vibrations on the towing carriage are not affecting the time-averaged values of $C_{D,M}$. Errors in C_L are generally somewhat larger, possibly because of larger fluctuations in the fluid flow in the y-direction due to vortex shedding from the forearm and fingers. Furthermore, the load cells in y-direction measure with a lower resolution than the load cells in x- and z-direction , which is likely to increase the size of random errors.

Figure 2.7a presents the drag coefficient C_D as a function of Reynolds number. A similar parabolic shape in C_D is observed as for the circular cylinder, with a larger magnitude in C_D due to the influence of the less streamlined hand compared to the cylinder. Differences in C_D for the investigated finger spreadings are small. Figure 2.7a shows that drag curves of the different finger spreadings have inconsistent behaviour at different Reynolds numbers, which is not explained by the done integral force measurements. For example, intersections of the drag curves at $\mathrm{Re} \approx 1.6 \cdot 10^5$ are observed. However, a clear distinction between the different drag curves is observed for $10^5 < \mathrm{Re} < 1.4 \cdot 10^5$, which shows that a small spreading of 5° is beneficial for drag maximization. The drag coefficient decreases as the finger spreading becomes larger than 5°, giving a minimum in C_D at 20° spreading. While no clear distinction in C_D over the whole Reynolds number range can be made, it shows that a small spreading of 5° is always optimal, and a large spreading of 20° is always disadvantageous.

In addition to drag forces, the force measuring system also provides information on the drag induced moments. The corresponding moment coefficient C_M is presented in figure 2.7b as function of Reynolds number. A similar trend in C_M is observed as in C_D, with as main difference that 10° spreading leads to increased drag in the range $0.8 \cdot 10^5 < \mathrm{Re} < 10^5$. Furthermore, differences in C_M for the different finger spreadings are somewhat larger than differences in C_D.

Similar to the circular cylinder, the parabolic shape in $C_{D,M}$ is likely a result of free-surface deformations, as the cylindrically shaped forearm intersects the water surface in a similar fashion. Therefore no Reynolds number dependence effects on $C_{D,M}$ are expected for a hand model towed through water in the absence of

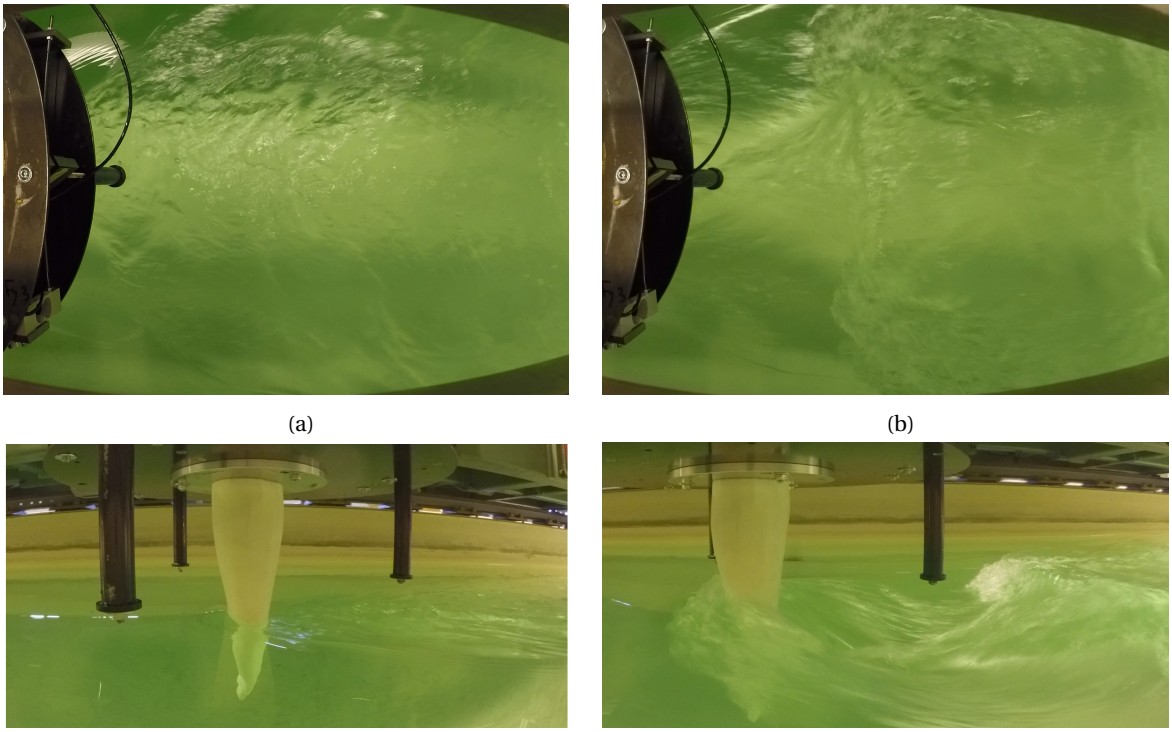

(a) (b)

(c) (d)

Figure 2.6: The wake formed behind a surface piercing arm model. (a) Top view with Fr = 0.65; (b) top view with Fr = 1.62; (c) side view with Fr = 0.65; (d) side view with Fr = 1.62.

a free-surface. This is in agreement with the Reynolds number independent effects that Takagi et al. (2001) found.

Figure 2.7c shows the variation of the lift coefficient C_L. Here, positive lift coefficients are directed from the thumb to the little finger. Lift coefficients are small compared to the drag coefficients, being $\approx 5\%$ of C_D. No zero lift is found with the hand palm orientated perpendicular to the flow, in contrary to previous research. This could partly be an effect of the suboptimal alignment of the force measuring system, but it is likely to be mostly an effect of the fluid flow around the arm models, as the alignment is only 2° off. Figure 2.7c shows that all arm models have significant different lift coefficients. This indicates that for varying angles of attack, the drag coefficients of all arm models change in different ways. Therefore it would interesting to investigate the effects of C_D, C_M and C_L for varying angles of attack during future research.

For the different arm models, weighted averages of $C_{D,M}$ are taken over the Reynolds number range. These weighted averages are shown relatively to that of the hand with 0° finger spreading in figure 2.7d. This gives information on the drag over the whole Reynolds number range, an optimum is found for 5° finger spreading. For 5° spreading, the coefficients C_D and C_M are respectively 1.1% and 1.7% larger in comparison to closed fingers. Furthermore, a 20° finger spreading results in a decrease in $C_{D,M}$ of 1.5%, compared to closed fingers.

The outcomes of the research towards the same arm models done by van Houwelingen et al. (2016) were presented in subsection 1.3.2. Note that they subjected the whole forearm to a fluid flow, while the towing tank experiments only had them partially immersed. Similarly to the experimental work of van Houwelingen et al. (2016), the maximum in C_D is found for 5° spreading. However their experimental work found an optimum in C_M for 10° finger spreading, which is not in agreement with towing tank experiments. Also the numerical work of (van Houwelingen et al., 2016) shows different trends, where 10° finger spreading is leading to largest drag, and an increase in drag for 20° finger spreading is observed as well. This trend is contradictory to figure 2.7a and 2.7d, where $C_{D,M}$ only decreases for spreadings larger than 5°. Magnitudes of the differences in $C_{D,M}$ for various finger spreadings are of the same order as van Houwelingen et al. (2016) showed, where their experimental work found differences up to 2%.

The found observations in drag coefficient agree with literature as it shows that a small finger spacing gives a larger obstruction in the flow than closed fingers, whereas a too large spacing has disadvantageous effects on the generated drag. The theoretical model of Westerweel et al. (2016) showed a maximum increase

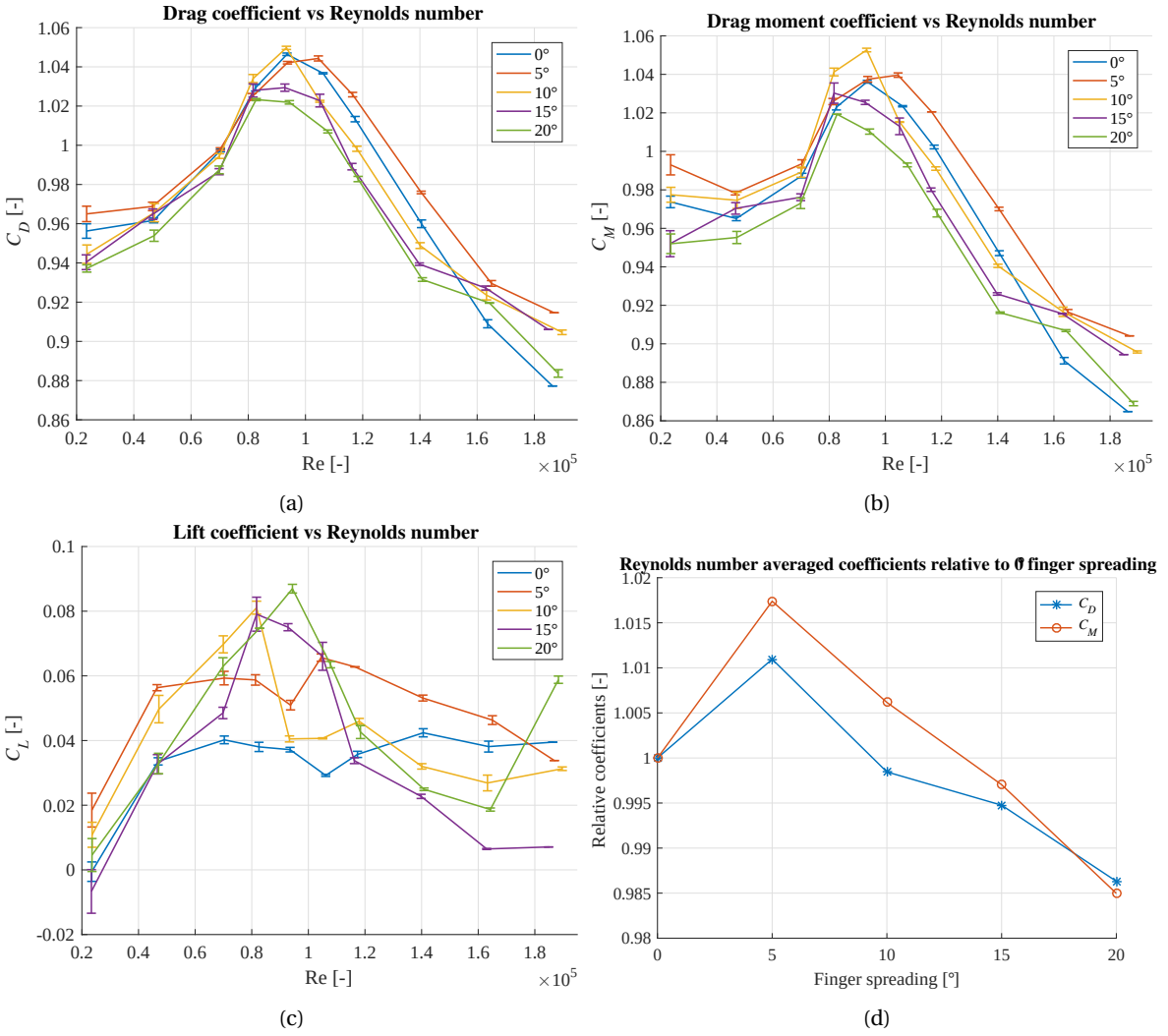

Figure 2.7: Force coefficients as function of Reynolds number for the models with finger spreading, here (a) shows the drag coefficient C_D, (b) shows the drag moment coefficient C_M and (c) the lift coefficient C_L. Weighted averages of C_D and C_M are taken over the whole Reynolds number range. (d) Presents the weighted averages of C_D and C_M relatively to the weighted average of the hand with 0° finger spreading.

in C_D of 3.5% for $d/D = 0.3$, while C_D decreases with up to 6% for $d/D = 1$. The towing tank experiments show smaller effects in C_D than Westerweel et al. (2016), which is not illogical since their abstract model has a completely different geometry than the arm models with finger spreading. However, the general relation between finger spacing and drag is the same.

2.4.3. Variation of immersion depth

It was assumed that the flow around the spread fingers only interacts with a quarter of the forearm. The validity of this assumption is investigated by varying the immersion depth of two of the arm models, i.e. 0.34 m immersion instead of 0.31 m. The 0.34 m immersion leads to an increased part of the forearm subjected to the flow, in analogy to figure 2.4 follows $A'_{arm} = 0.00021$ m^2. Corrections are applied to have insight in only the drag forces acting on A_{hand} and A_{arm}. This allows for comparisons of drag coefficients from experiments done with 0.31 m and 0.34 m immersion.

The experiments for the deeper immersed arm models are only performed once due to time limitations. The minimalistic error bars from figures 2.7a - 2.7b suggest that it is not necessarily needed to repeat experiments. Figure 2.8 presents effects of immersion depth on the drag coefficients for 5° and 10° spread fingers, while the drag moment coefficient C_M shows similar behaviour. The experiments for deeper immersion were performed at somewhat higher temperatures, such that Reynolds numbers are around 5% larger. Therefore,

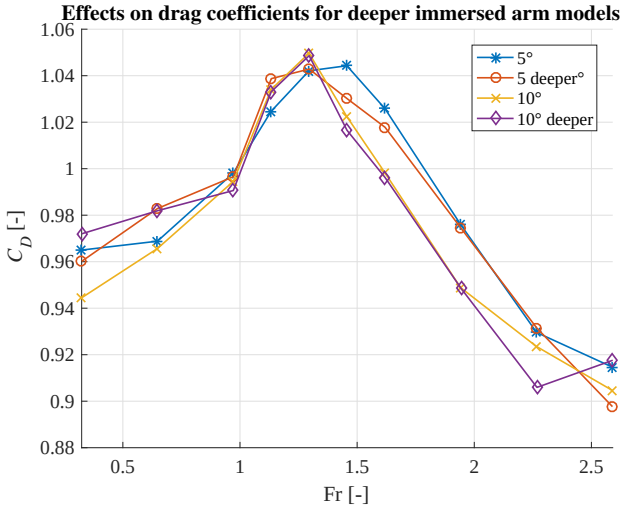

Figure 2.8: Effects on drag coefficient for deeper immersed arm models with 5° and 10° finger spreading. Immersion depths of 0.31 m and 0.34 m are investigated.

comparing drag coefficients on basis of Froude numbers is more suitable, as the obtained parabolic shape is likely to be an effect of the created surface deformations only, and temperature variations have no effects on the Froude number.

The found drag coefficients are not exactly matching for both immersion depths, but it is seen that the same parabolic shapes are obtained and differences in C_D are generally small. Especially the values of C_D are similar for 10° finger spreading when $1 < \text{Fr} < 2$, where the differences in C_D are of the size of the error bars from figure 2.7a. Differences in C_D become significantly larger outside the range of $1 < \text{Fr} < 2$, with deviations in C_D up to 2%. For $\text{Fr} < 1$ the low accuracy of the force measuring system is likely to cause the deviations in C_D. For 5° finger spreading, the drag coefficient is significantly deviating for most Froude numbers, with deviations in C_D up to 1.5%. Although some large deviations in C_D are observed, there is still a clear distinction between the models with 5° and 10° finger spreading. This leads to the conclusion that a finger spreading of 5° can generate larger drag forces than a spreading of 10°. This indicates that the used immersion depth of 0.31 m was sufficient to find differences in drag acting on arm models with varying finger spreading.

2.5. Conclusion

Experiments on the circular cylinder found surface piercing effects that were in agreement with Hoerner (1965). The parabolic shape in $C_{D,M}$ for the circular cylinder was assigned to the surface piercing, as the drag coefficient for circular cylinders is independent of Reynolds number for the investigated range of Reynolds numbers. A similar parabolic shape in $C_{D,M}$ was found for the hand models. This indicated that, in the absence of free surface, Reynolds number independent effects on $C_{D,M}$ are expected as well. This observation matches with those of previous research by e.g. Takagi et al. (2001), who showed that the drag coefficient of a hand model is independent of Reynolds number.

The effects of immersion depth were investigated. Experiments for one finger spreading, with varied immersion depth found significant differences in C_D. However, the distinction in generated drag forces for different finger spreadings remained unchanged. This indicates that only a small immersion depth is needed to find differences in drag between the different arm models.

The error bars for the repeated experiments were found small. The smallest and largest errors in C_D were around 0.05% and 0.4% of the mean value, respectively. This indicates that effects of random errors are negligible and experiments are very well repeatable. Therefore, the effects of fluctuations in the fluid flow and external vibrations are negligible in the determined time-averaged forces and moments. For this reason, the used experimental setup is considered sufficient for finding small differences in forces and moments that act on the arm models.

The towing tank research showed that an optimum in drag coefficient arises for small finger spreadings. A hand with 5° finger spreading is responsible for around 1.1% to 1.7% larger drag compared to closed fingers. The drag coefficient decreases for spreadings >10°, where for a largest spreading of 20° the decrease in $C_{D,M}$ is

about 1.5% compared to closed fingers. The dependency of drag on finger spreading did no completely agree with the work of van Houwelingen et al. (2016). Their wind tunnel experiments found an optimum in C_D and C_M for 5° and 10° finger spreading, respectively. And the numerical work found optima in $C_{D,M}$ for both 10° and 20° finger spreading.

3

Finger spreading: abstract modelling

Chapter 2 investigated the effects of finger spreading by use of different 3D-printed arm models. This gave a realistic reproduction of the hand of a swimmer in different configurations. The increase in drag is explained by the enhanced obstruction in the fluid flow provided by slightly opened fingers. This is in analogy to the drag experienced by a porous disk, where small porosities can enhance the drag (Theunissen et al., 2016).

The experiments on the full scale arm models from chapter 2 were both time and money consuming, which makes the exploration of more simplified shapes interesting. Therefore it is investigated how a hand with finger spreading can be described more abstractly, such that simple, mathematically well described 2D geometries can be created for further research. This chapter looks into simple geometries usable for this purpose.

Hands with finger spreading are represented by circular disks that have well-defined shapes cut into it (slotted disks). CFD simulations in ANSYS Fluent are carried out to look into the effects of drag for different slotted disks. The first part of this chapter looks into the analogy between hands with finger spreading and circular disks. Then simulations are carried out around ordinary circular disks, as validation of the simulation methods. Hereafter, the used slotted disk geometries are described, whereafter the simulation results are discussed. Finally, conclusions are drawn whether slotted disks can represent hands with finger spreading.

3.1. Disk-hand analogy

A hand is relatively thin and has no streamlined shape, it is expected that contributions of viscous drag to the total drag are small. Then in the absence of a free-water surface only influences of pressure drag are experienced by the hand. This is in analogy to the experienced drag for circular disks, where Nakayama & Boucher (1998) show that contributions of viscous drag are negligible for a circular disk. A circular contour can be drawn around a hand with 0° finger spreading, hence as a first approach, a hand with closed fingers is represented by a circular disk. Similarly, a hand with spread fingers is enclosed by a circular contour in which slots are cut to account for the finger spreading. The slotted disks discussed in section 3.3 are created for the purpose of abstractly describing finger spreading, examples of slotted disks are presented in figure 3.8. This section gives information on the flow around circular disks. Furthermore, the effects of porosity in perforated disks are discussed.

3.1.1. Flow around a circular disk

Figure 3.1 illustrates the flow field around a circular disk. Here a stagnation point exists at the inflow side of the disk, resulting in a high pressure relative to the free stream. A boundary layer grows on the front of the disk from the centre to the edges. Negligible boundary layer growth takes places on the edges of the disk, as the disk is thin in comparison to its diameter. Therefore the flow separates immediately from the edge, resulting in a broad wake with low pressure compared to the free stream. The pressure differential over the disk results in a contribution of pressure drag, while effects of viscous drag are negligible (Nakayama & Boucher, 1998).

Figure 3.2 shows the drag coefficient for a circular disk as function of Reynolds number (Hoerner, 1965). This figure summarizes data coming from several wind tunnel experiments all showing that $C_D \approx 1.17$ for $10^4 \leq \mathrm{Re} \leq 10^6$. For a hand palm width of 0.1 m, Reynolds numbers are of the order $\mathrm{Re} \sim 10^5$ during actual swimming. Therefore, in this CFD research towards a hand-disk analogy, simulations are performed at three

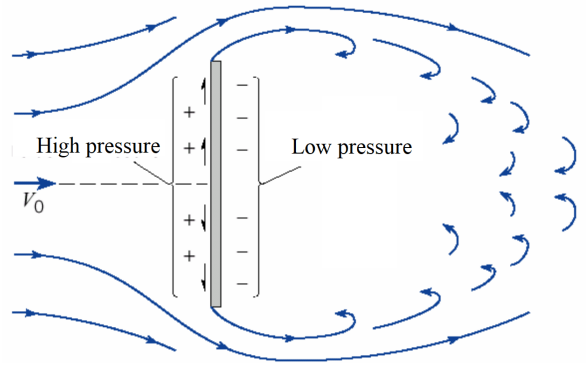

Figure 3.1: Illustration of a fluid flow normal to a circular disk. Modified from Crowe et al. (2008).

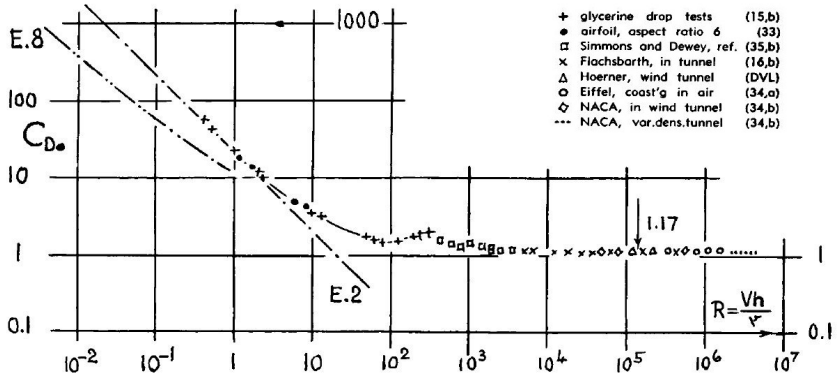

Figure 3.2: Drag coefficients for circular disks (in normal flow) as a function of Reynolds number (Hoerner, 1965).

Reynolds numbers ranging from $10^4 \leq \mathrm{Re} \leq 10^6$. The simulations are used to see if the value $C_D \approx 1.17$ can be retrieved, and if the drag coefficient is independent of the Reynolds number.

3.1.2. Effects of porosity

The enhanced drag found for a small finger spreading has similarities with the drag for a porous plate. Batchelor (2000) considered a flat rigid plate with holes drilled into it that is subjected to a steady flow velocity V. Then fluid discharges from the rear of the plate as a number of jets which ultimately mix with the surrounding fluid. In the wake, the velocity equals that of the free stream velocity V again (Batchelor, 2000). A simple model based on a momentum balance argument found the drag force acting on a perforated plate as

$$F_D = \frac{1}{2}\rho V^2 (1-\beta)^2, \tag{3.1}$$

here the porosity β corresponds to the perforated fraction of the plate (Batchelor, 2000). Equation 3.1 indicates that the drag coefficient decreases for increasing porosity, which is illustrated in figure 3.3a. Next to the simple momentum balance argument of Batchelor (2000), Theunissen et al. (2016) performed experimental research to the modelling of porosity by a continuous distribution of (singular) point sources on the surface of a disk. Figure 3.3a shows experimental data taken from Theunissen et al. (2016), where six different hole topologies were investigated with porosities β ranging from 0.05 to 0.50. Theunissen et al. (2016) shows a similar trend of decreasing drag coefficients as the model of Batchelor (2000). However, the decrease in C_D for the model of Batchelor (2000) is much steeper, this is likely a result of the infinite plate size and the continues distribution of the holes in this model. From Theunissen et al. (2016) follows that a small porosity of $\beta = 0.05$ can increase the drag coefficient with 3%, compared to a closed circular disk. For $\beta = 0.10$, the drag coefficient equals that of a closed circular disk again, whereafter C_D decreases further for $\beta > 0.10$. Drag coefficients were found independent of Reynolds number for the investigated range $0.4 \cdot 10^5 < \mathrm{Re} < 1.7 \cdot 10^5$. Hole topology has large effects on the drag coefficient, resulting in variations of C_D up to 5% for a constant

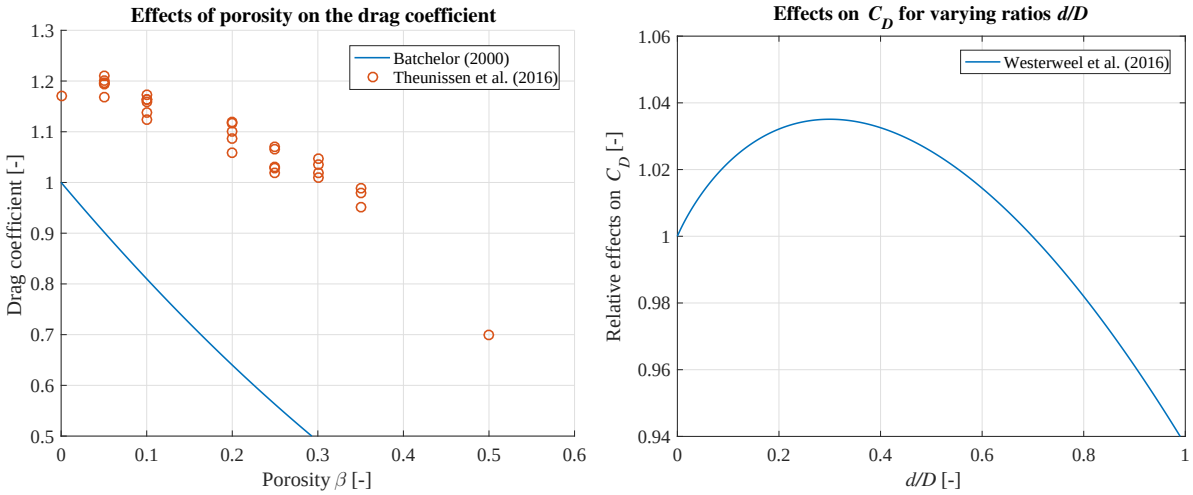

(a) (b)

Figure 3.3: The relationship of drag coefficient for different models. (a) Shows the effects of porosity based on Batchelor (2000) and Theunissen et al. (2016). (b) Shows the effects of varying the ratio d/D (finger spacing to finger thickness) (Westerweel et al., 2016).

porosity. The findings of Theunissen et al. (2016) indicate that the drag of porous disks is caused by a combination of the pore flow and the separated flow around the disk. It is likely that similar flow behaviour is found around slotted disks, where the slots act as a porosity.

The model of Westerweel et al. (2016) can be used as an alternative to describing finger spreading with porosity. Here a pore flux is assumed proportional to the pressure difference across a disk, where the flux is also determined by the geometry of the interdigit region. In this way, finger spreading is represented by four equispaced cylinders with spacing d and diameter D. The corresponding relation between drag force and ratio d/D is presented in equation 1.5. Figure 3.3b gives an illustration of the relation between the effects on C_D and the ratio d/D. Here a small spacing of $d/D = 0.3$ increases the drag coefficient with 4%, while C_D decreases with 6% for $d/D = 1$. Similarity in geometry between the slotted disks and the model of Westerweel et al. (2016) is observed, which suggests that the drag on the slotted disks can be described by the flux through the interdigit region.

3.2. Simulation on circular disks

This section describes the CFD simulations carried out on circular disks as part of a validation of the simulation methods. The used computational domain and simulation settings are discussed, and the effects of grid refinement and turbulence modelling are investigated. Finally, conclusions are drawn regarding the suitability of the used simulation methods for further use on the slotted disks.

3.2.1. Computational domain

The circular disk is modelled as two-dimensional and infinitely thin, as this makes grid generation easier compared to a three-dimensional disk. Two-dimensional modelling of the disk is expected to be suitable based on the observed fluid flow illustrated in figure 3.1, where no viscous drag is observed due to the small thickness of the disk.

In principle, simulations around circular disks can be carried out in a two-dimensional domain by use of the axisymmetry condition. However, simulations around the slotted disks require a three-dimensional computational domain, as they have an axisymmetrical shape. In principle, simulations along all the slots of the slotted disks are not required to obtain insight in the drag coefficients, as the slots have a repeating pattern over the circumference of the disk. However, to generate a computational domain that is also suitable for future simulations around asymmetric geometries, a three-dimensional computational domain is used where the flow around the complete (slotted) disk is simulated. Therefore for the purpose of validating the simulation methods, the three-dimensional domain from figure 3.4a is used for simulations around the circular disks. This domain is subdivided into 3x3x3 blocks. The two-dimensional disk is placed in the centre of the domain, as shown in figure 3.4b. The fluid flow is directed normal to the disk, where flow variables near

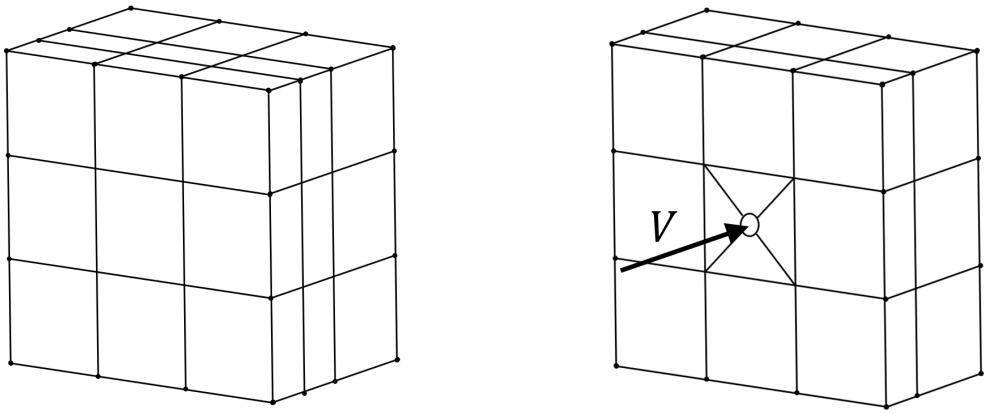

(a) The complete three-dimensional computational domain subdivided into 3x3x3 blocks.

(b) Part of the computational domain that shows the location of the circular disk.

Figure 3.4: Different views of the computational domain, the fluid flow is directed normal to the disk with velocity V.

Table 3.1: Number of cells for the different used grids as part of a grid refinement study.

Grid	Number of cells
Coarse	$2 \cdot 10^5$
Medium	$6 \cdot 10^5$
Fine	$2 \cdot 10^6$

the disk and inside its wake are changing with large gradients. Small cell sizes are required to resolve the large gradients in the flow. The used computational domain allows for small cell sizes around the disk and in its wake, making the flow in these regions well described. Gradients in the flow are smaller further away from the disk, therefore larger cells are used in these regions to save computational time.

Figure 3.5a shows a front view of the mesh created in the plane intersecting the disk, where figure 3.5b zooms in around the disk. On the surface of the disk an unstructured grid is used which small cells, the cells grow larger from the edge of the disk to the rectangle that encloses it.

Figure 3.5c shows a side view of the grid, where fluid flows from top to bottom. Cells become smaller from the domain inlet to the disk, and after the disk they grow larger again. In this way, the fluid flow in the near wake and stagnation point of the disk is well described, where gradients in the flow are large. Meshes for three different grid refinement levels are investigated as part of a grid refinement study. Table 3.1 gives an overview of the used grids and their number of cells.

3.2.2. Turbulence modelling and wall Layers

For the current CFD study, fluid flow is simulated normal to a two-dimensional circular disk in the range of $10^4 \leq \mathrm{Re} \leq 10^6$. Chaotic flow with a highly turbulent wake behind the disk will be observed for the investigated Reynolds numbers. The turbulence is modelled by means of the the Reynolds-averaged Navies-Stokes (RANS) equations. Those RANS equations decompose the velocity, pressure and force components in a mean and fluctuating part (Nieuwstadt et al., 2016). Turbulence models are needed for closure of the system of RANS equations. For this closure, an extra equation describing the change in turbulence kinetic energy k is added (Nieuwstadt et al., 2016). Several two-equation closure models exist and are implemented in ANSYS Fluent. These models assume that two independent scales are needed to statistically describe turbulence. Commonly the $k-\epsilon$ and $k-\omega$ are used for turbulence modelling, of which several variations exist, below a description of the turbulence models is given.

- $\boldsymbol{k-\epsilon}$: this model solves a transport equation for the turbulent kinetic energy k and a similar transport equation for the turbulent dissipation ϵ (the rate at which turbulent kinetic energy is converted into thermal energy). The model is often useful for free-shear layer flows with relatively small pressure gradients (Frei, 2017; ANSYS, 2009). A free-shear layer develops between the free stream velocity and the near zero velocity occurring within the wake of a circular disk. Because of the shape of the disk, a strong pressure gradient and strong flow separation will be observed in its wake, making the $k-\epsilon$ model likely

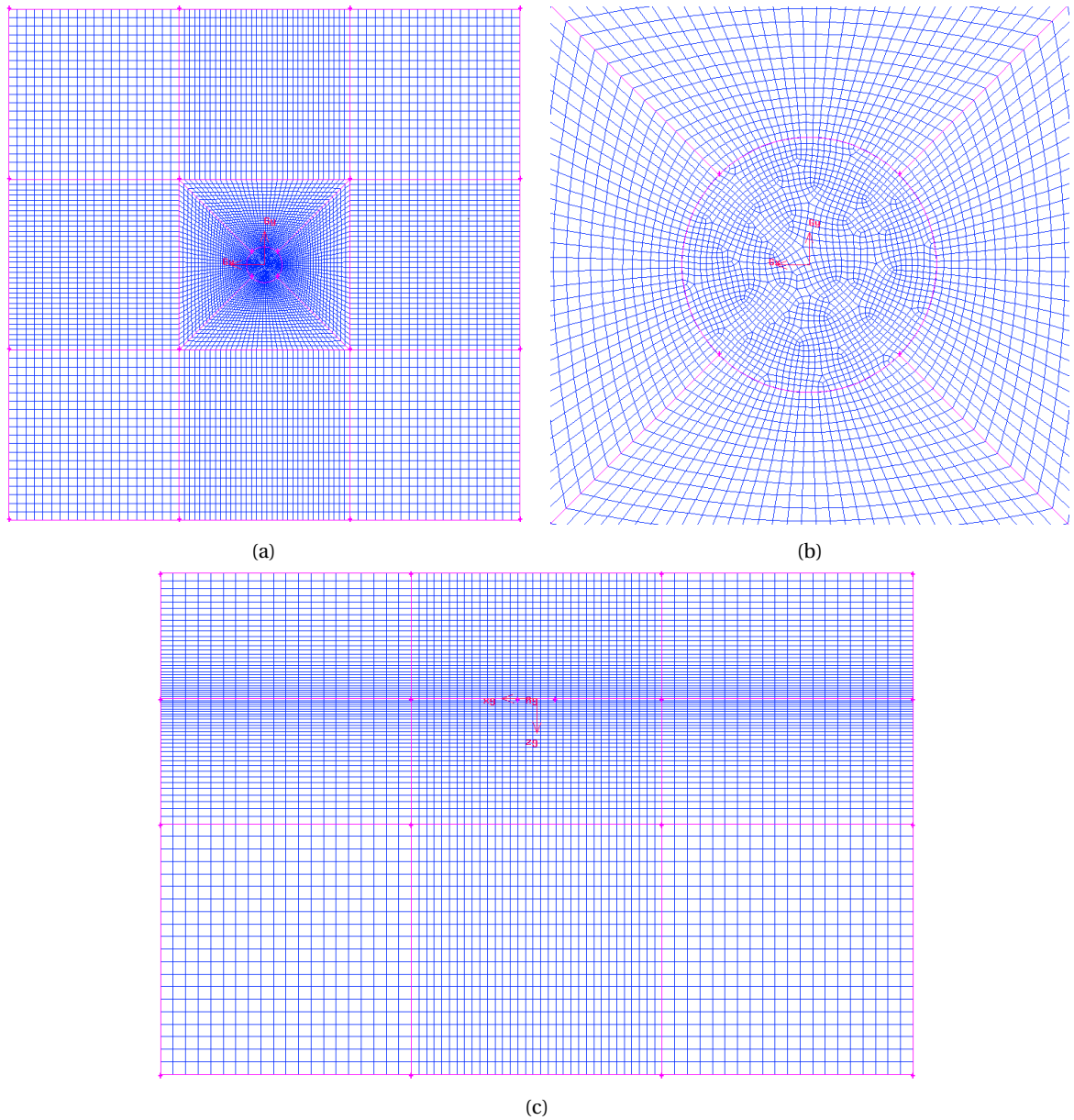

(a) (b)

(c)

Figure 3.5: Presentation of different views of the grid. Where (a) shows a front view with the disk in the centre and (b) gives a close up view of the disk in front view, here fluid flows normal to the disk. In (c) a side view is shown, where cells become larger further away in the wake, fluid flows from top to bottom.

not to be suitable. Another drawback is that the model does not behave well in the logarithmic region of the boundary layer, which requires the implementation of wall functions.

- **Realizable $k-\epsilon$**: this model uses an improved equation for the turbulent dissipation rate ϵ. This improves the simulation of flows involving boundary layers under strong adverse pressure gradients or separation (ANSYS, 2009). This makes the model more suitable for simulations around a circular disk than the standard $k-\epsilon$ model, where strong adverse pressure and separation occur close to the disk.

- **$k-\omega$**: in this model a transport equation for the specific dissipation rate $\omega = k/\epsilon$ is solved, rather than the dissipation rate ϵ. A drawback of this model is its sensitiveness to the inflow boundary conditions. Therefore a modification to this model is suggested that uses the $k-\omega$ formulation for the inner parts of the boundary layer and $k-\epsilon$ in the free-stream, the so called $k-\omega$ model SST (Shear Stress Transport) (Frei, 2017; ANSYS, 2009). In this way the model behaves well for adverse pressure gradients and flow separation, which are observed for the fluid flow around a circular disk.

These different turbulence models will be applied to the simulations on the circular disks, such that a suitable turbulence model can be chosen for the simulations around the slotted disks.

The front and rear of the two-dimensional disk are modelled as walls. On the front of the disk a boundary layer grows according to the principles figure 1.2. Fluid particles that collide on the front of the disk move near the outer edge. The fluid particles experience shear stresses as they move over the disk, which results in boundary layer growth. As the disk is infinitely thin, the flow separates immediately as it reaches the outer edges. The turbulent boundary layer on the front of the disk either needs to be in in the viscous sublayer or in the turbulent region, such that either the viscous stresses or the turbulence stresses have to be described (Nieuwstadt et al., 2016). Insight in the wall layers is obtained by studying the dimensionless wall distance y^+. For $5 < y^+ < 30$ the buffer layer is observed, hence a wall distance y^+ is required outside this interval to properly describe the fluid stresses (Nieuwstadt et al., 2016). The wall distance y^+ is calculated as

$$y^+ = y\frac{u_*}{\nu}, \tag{3.2}$$

here y is the distance to the nearest wall and u_* is the friction velocity at the nearest wall. The friction velocity u_* gives information on the flow velocity in the boundary layer and is defined as

$$u_* = \sqrt{\frac{\tau_w}{\rho}}, \tag{3.3}$$

here the wall shear stress τ_w is the shear stress in the layer of fluid next to the wall. This shear stress is a result of the friction created by the stationary wall on the moving fluid. The wall shear stress is a quantity that follows from the simulations.

3.2.3. Simulation settings and boundary conditions

Table 3.2 gives an overview of the important simulation settings and dimensions of the disk and domain. Furthermore, table B.1 in appendix B gives more detailed numerical settings.

Only time-averaged properties of the flow are required in order to obtain insight in the drag acting on the disks. For this reason a steady-state solver is used. This has as advantage that the computational time is reduced, compared to transient solving. However the time-averaging deprives insight in instantaneous flow fields.

The front of the domain from figure 3.5a is used as velocity inlet. The fluid flows out of a plane that is opposite to the inlet, at this boundary a pressure outlet is defined at atmospheric pressure. The four outer planes that connects the inlet and outlet have a symmetry boundary condition. In this way fluxes, velocity components and other variables are set to zero at the boundary. The symmetry condition treats the flow as if the flow patterns mirror symmetrically around the boundary, which reduces computational time (ANSYS, 2009). A no-slip wall boundary condition is used on the circular disk, this models the disk as a solid on which all velocity components are set to zero.

3.2.4. Validation

Effects of grid refinement, turbulence modelling and Reynolds numbers are investigated to validate the simulation methods. Figure 3.6a presents the found drag coefficients for simultaneously varied grids and Reynolds

Table 3.2: Main settings of the simulations, where table B.1 in appendix B gives details of the numerical settings.

Description	Symbol	Value	Unit
Disk diameter	D	1.4	m
Domain width	-	20.5	m
Domain height	-	20.5	m
Domain length	-	13.8	m
Density of fluid	ρ	1.225	$\mathrm{kg\,m^{-3}}$
Dynamic viscosity of fluid	μ	$1.7894{\cdot}10^{-5}$	$\mathrm{kg\,m^{-1}\,s^{-1}}$
Reynolds numbers	$\mathrm{Re}/10^5$	0.2, 1.0, 1.8	-
Turbulent intensity	-	5	%

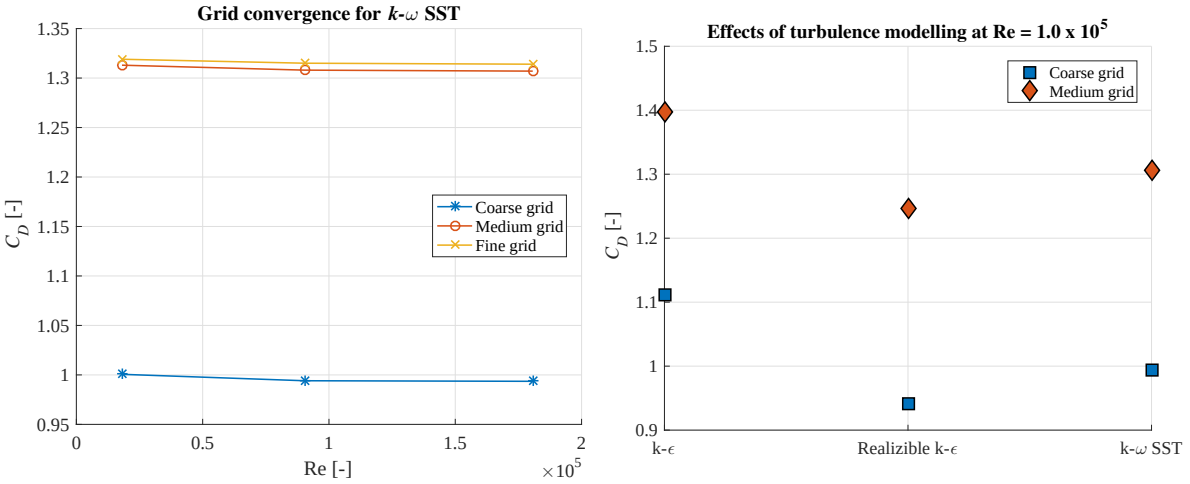

(a) (b)

Figure 3.6: Found drag coefficients for circular disks. (a) Shows C_D as part of grid refinement study. The required computational time for the coarse, medium and fine grid were around 1 hour, 4 hours and 13 hours, respectively. (b) Shows C_D as part of a turbulence modelling study.

numbers. Those simulations used the $k-\omega$ SST model. It appears that C_D is independent of Reynolds number for $0.2 \cdot 10^5 < \mathrm{Re} < 1.8 \cdot 10^5$, which is in agreement with the experimental data from figure 3.2. The drag coefficient C_D clearly converges for the finest grid size. The required computational time for the coarse, medium and fine grid were around 1 hour, 4 hours and 13 hours, respectively. The required computational time for the medium grid is significantly lower than for the fine grid, while the found drag coefficients are comparable, therefore it is recommended to perform simulations for the slotted disks on the medium grid.

Figure 3.6b gives an overview of found drag coefficients for different turbulence models at $\mathrm{Re} = 1.0 \cdot 10^5$, where both the coarse and medium grid are considered. Figure 3.6b shows that found drag coefficients are strongly dependent on the used turbulence model, which can give variations in C_D up to 15%. Similar effects of turbulence models are found for the two grids, with $k-\epsilon$ giving largest C_D and realizable $k-\epsilon$ giving lowest C_D. Both the realizable $k-\epsilon$ and $k-\omega$ SST models are expected to be suitable for simulations around two-dimensional circular disks. On the medium grid, the realizable $k-\epsilon$ models found $C_D = 1.25$, this gives a difference of 7% compared to the experimental data from figure 3.2. Similarly, the $k-\omega$ SST model found $C_D = 1.31$, giving a difference of 11% compared to the experimental data. Simulations on the slotted disks will be performed with both turbulence models, with the remark that the realizable $k-\epsilon$ model is likely to give more accurate results, because realizable $k-\epsilon$ found better agreement with experimental data than $k-\omega$ SST.

Two contour plots are presented to illustrate that the fluid flow matches figure 3.1. Figure 3.7a shows the velocity field on a plane through the centre of the circular disk, while figure 3.7b shows the variation of static pressure. These two contour plots are in agreement with figure 3.1. They show there is zero velocity and a large static pressure in the stagnation point. The velocity decreases significantly in the wake near the disk, whereafter the velocity starts stabilizing again to the free stream velocity further downstream in the wake. Note that the free stream velocity is not yet obtained at the outflow of the domain, this could give

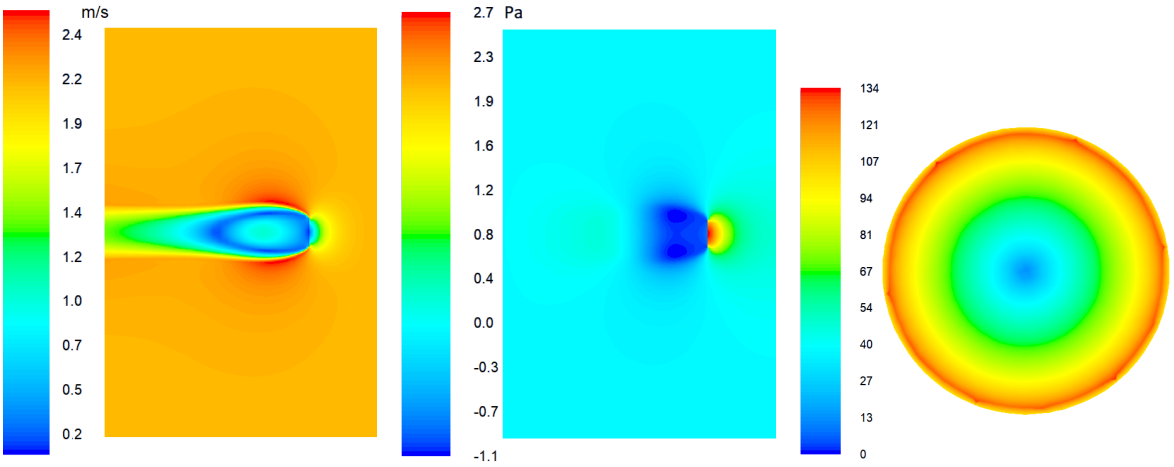

(a) (b) (c)

Figure 3.7: Contour plots on a plane through the centre of the circular disk; (a) shows the velocity magnitude and (b) the static pressure. (c) Presents the the dimensionless wall distance y^+ at the front of the disk.

a pressure increase in the wake, resulting in too low drag forces experienced on the disk. Simulations for an increased domain length were carried out to look into its influence on the experienced drag forces. An increased domain length did not have effects on the drag forces. As the larger domain required significantly more computational time, it is chosen to perform further simulations for the slotted disks on the original domain that was illustrated in figure 3.4.

Figure 3.7c shows that in general the dimensionless wall distance is $y^+ > 40$ on the front of the disk. Only around the centre of the disk lower values of y^+ are obtained, because here the friction velocity $u_* = 0\,\mathrm{m\,s^{-1}}$, resulting in $y^+ = 0$ according to equation 3.2. As $y^+ > 40$, the boundary layer is located inside the turbulent region, where the viscous stresses are negligible compared to the turbulence stresses. A dimensionless wall distance $y^+ < 5$ can be reached on the whole front of the disk by drastically refining the grid. More accurate values of C_D are expected when $y^+ < 5$, as this would model the viscous stresses acting on the disk. However, due to the required increase in computational time there is settled for the current simulation results.

So in conclusion, the simulations for the slotted disks will be carried out on the medium grid, that contains $6 \cdot 10^5$ cells. The same computational domain as shown in figure 3.4 will be used. The effects of both the realizable $k-\epsilon$ and $k-\omega$ SST models will be investigated.

3.3. Simulations on slotted disks

Previously, a circular disk was used to represent a hand with 0° finger spreading. Finger spreading is introduced by creating slots on the edges of the disk. The slots are shaped in a mathematically well described manner, such that hands with finger spreading are represented more fundamentally. This section describes the created slotted disks and the corresponding simulation results. Finally conclusions are drawn on the validity of modelling hands with finger spreading by means of the slotted disks.

3.3.1. Geometric properties

Slots are cut along the edges of a circular disk, the slot width varies in a similar way as for a hand with finger spreading, illustrated with the ratio d/D in figure 3.9. As the slot width increases, the diameter of the disk needs to increase simultaneously, to maintain a constant projected area A. Also the slot height needs to vary simultaneously to maintain a constant ratio of slot height to disk diameter. Furthermore, for realism the smooth shape found along the trajectory of spread fingers is preferably maintained for the slotted disks. A Gaussian is found to satisfy all these criteria This function has a bell curved shape and is described by

$$f(x) = a e^{-\frac{(x-b)^2}{2c^2}}, \tag{3.4}$$

where a is the height of the curve, b is the position of the centre of curve and c controls the width of the curve. Slotted disks are created by subtracting selected Gaussians from the edge of a circular disk. This results in

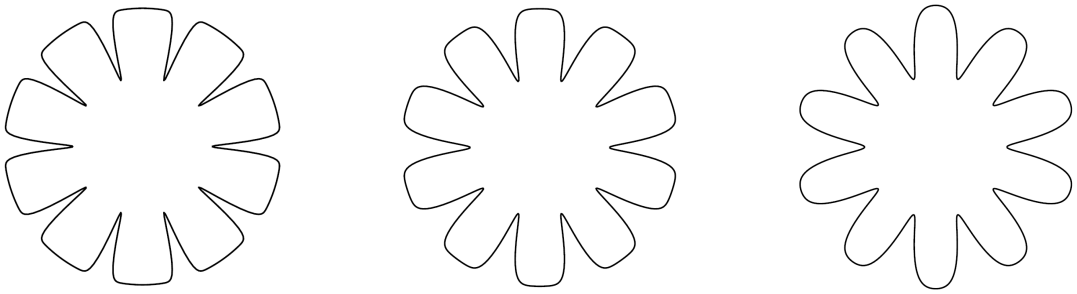

(a) $c = 1.75$ (b) $c = 3.00$ (c) $c = 4.50$

Figure 3.8: Illustration of three slotted disks with varying gap width c.

Table 3.3: Geometric properties of the slotted disks. Here c characterizes the gap width, R is the radius of the disk, d/D gives a ratio of spreading as illustrated in figure 3.9 and $\beta = (A_{out} - A_{in})/A_{out}$ is the porosity.

	c	R	d/D	β
Disk 1	1.75	84.53	0.20	0.14
Disk 2	3.00	89.05	0.34	0.22
Disk 3	4.50	94.75	0.56	0.31
Hand 0°	-	-	0.00	0.00
Hand 5°	-	-	0.23	0.04
Hand 10°	-	-	0.44	0.09
Hand 15°	-	-	0.65	0.13
Hand 20°	-	-	0.82	0.16

slotted disk with x- and y-coordinates given by

$$x = \big(R - f(x)\big)\cos\theta, \tag{3.5}$$

$$y = \big(R - f(x)\big)\sin\theta, \tag{3.6}$$

here R is the radius of the disk and θ the angle for which it exists. For the sake of symmetry, slots are created over the entire arc of the disk, i.e. $0 \leq \theta \leq 2\pi$. A hand with four spread fingers is observed to occupy approximately a third of a circle. Therefore it is chosen to cut ten slots into a full circle to have geometric similarity with a hand with finger spreading. For a hand it is observed that the finger length is approximately the radius of a circle that surrounds the hand. As the slots are present over the whole edge of the circle it is chosen to give them a height equal to half the circle radius, i.e. $a = R/2$. Figure 3.8 gives several examples of slotted disks that are created in this way. The positions of the slots are kept constant, i.e. $b = 0$. When the slot width varies by changing c, the radius R needs to change simultaneously to keep the surface area constant.

Figure 3.9 gives an overview of geometric properties that are found for both the slotted disk models and the hand models used in chapter 2. Here d and D correspond to the geometry of the slots and finger spreading. A ratio d/D is presented in table 3.3 for both the slotted disks and hand models. The areas A_{in} and A_{out} correspond to the surface areas enclosed by respectively the solid and dashed lines. A porosity is defined as $\beta = (A_{out} - A_{in})/A_{out}$, which is presented in table 3.3.

The topology of the slotted disks has on one side similarity with that of a perforated disk, where slot acts as a porosity. However, the porosity of the slots is not equally distributed over the disks as the holes in a perforated disk. This gives the expectation that effects of obstruction in the fluid flow are different for the slotted disks and perforated disks. Furthermore, the slots have a similarity with spaced cylinders. Analogy between the slotted disks and spaced cylinders seems a more realistic representation because the slot width can be varied in a same fashion as the spread fingers. For this reason, variations in d/D are investigated for the slotted disks. For the investigated ratios d/D from table 3.3 the model of Westerweel et al. (2016) gives expectations in drag increase of respectively 6.4%, 6.9% and 3.9% compared to closed fingers.

3.3.2. Results and discussion

The same simulation methods as for the circular disks from section 3.1 are used. Simulations are performed on the medium grid, where effects of both the realizable $k-\epsilon$ and $k-\omega$ SST models are investigated. The

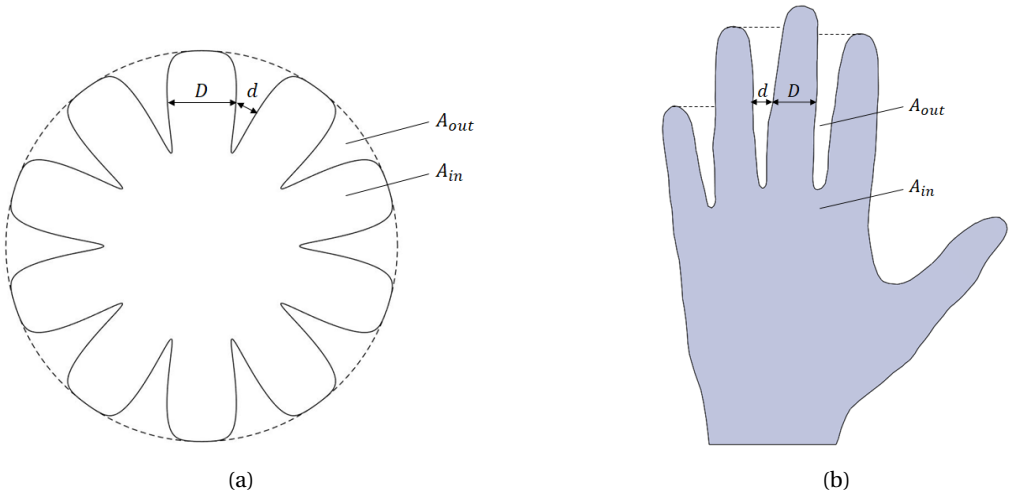

(a) (b)

Figure 3.9: Geometric properties; (a) for slotted disks, (b) hands with finger spreading. Here d/D gives information on the spreading for the fingers and slots. A_{in} and A_{out} correspond to the surface areas enclosed by the solid and dashed lines, respectively.

required computational times were around 8 hours, this is an increase of 4 hours in comparison to the simulations for the circular disks in section 3.2. An overview of drag coefficients following from simulations is presented in figure 3.10, here C_D is given for varying ratios d/D. It appears that the two different turbulence models lead to opposite effects. Realizable $k-\epsilon$ shows an increase in C_D of 1% for increasing d/D, while $k-\omega$ SST shows a decrease in C_D of 2% for increasing d/D. Furthermore, significantly lower values of C_D are observed in comparison to the closed circular disks. Contour plots for the slotted disks appeared to be similar to those in figure 3.7.

The theoretical model from Westerweel et al. (2016) gives expected drag increases of respectively 6.4%, 6.9% and 3.9% for the investigated ratios of d/D from table 3.3. This trend is not found in the simulation results of figure 3.10 for either of the used turbulence models. This indicates that the flow around the slotted disks does not correspond to the model of Westerweel et al. (2016).

Theunissen et al. (2016) looked into the effects of porosity for perforated disks. For the investigated porosities of the slotted disks from table 3.3 ($\beta = 0.14, 0.22, 0.31$) the drag coefficients would decrease with respectively 5.5%, 11% and 17%, according to Theunissen et al. (2016). The simulations with the $k-\omega$ SST model show a similar trend, where the drag coefficients are decreasing as the porosity increases. However, the decreases in C_D for the slotted disks are significantly smaller compared to the perforated disks of Theunissen et al. (2016). This is could be caused by the unevenly distributed porosity for the slotted disks, in comparison to the evenly distributed porosity for the perforated disks. The $k-\epsilon$ model shows opposite behaviour that does not correspond to the drag coefficient of perforated disks. As the simulation results for different turbulence models are contradictory, it is uncertain whether the slotted disks have an analogy with porous disks.

The contradictory simulation results give concerns whether the used simulation methods are suitable for the slotted disks. It appeared that the used simulation methods were valid for the circular disk, although differences in C_D were fairly large compared to experimental data. For future research, several modifications are recommended to make to the simulations that might improve the results. By giving the disk a small finite thickness, boundary layer growth is introduced on its edges. This would result in a more realistic flow separation from the edges, resulting in a more accurate wake formation and thus more accurate drag forces. Another improvement could be found by refining the grid significantly, in a way that the dimensionless wall distance $y^+ < 5$ everywhere on the disk. In this way the simulations take the viscous stresses acting on the disks into consideration. This gives a more complete description of the fluid flow, therefore it is expected that simulation results will come in better agreement with experimental results when $y^+ < 5$ on the disk.

3.4. Conclusion

The simulations around circular disks found drag coefficients comparable to experimental research, being around 7% - 11% off. The medium grid that contains $6 \cdot 10^5$ cells was found sufficient to solve the flow around

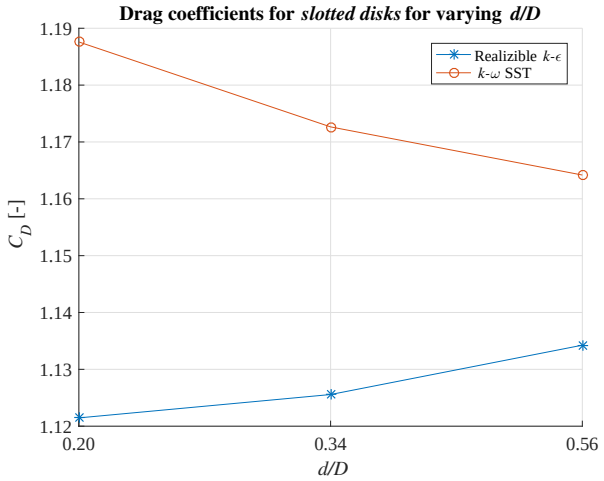

Figure 3.10: Drag coefficients following from the simulation on the slotted disks, presented as function of the ratio d/D. Results of both the realizable $k-\epsilon$ and $k-\omega$ SST model are presented.

a circular disk. Furthermore, effects of C_D appeared to be independent of Reynolds number. The same simulations were expanded to slotted disks that represented finger spreading. For the slotted disks, opposite trends in C_D were observed for different turbulence models. Furthermore, the increases and decreases in C_D appeared to be small, being respectively 1% and 2% for the realizable $k-\epsilon$ and $k-\omega$ SST model, respectively. The simulations around slotted disks did not show a similarity in behaviour with the drag experienced by perforated disks. Also no similarity in C_D was found for the slotted disks and the abstract finger spreading model from Westerweel et al. (2016). From the observations in the simulations results can be concluded that simple simulations on slotted disks are not a viable option to represent hands with finger spreading.

For future research it is recommended to investigate the effects on C_D for the slotted disks by use of experimental research. Wind tunnel experiments can give quick insight in the behaviour of C_D for different slotted disk models. By means of those experimental results, statements can be made regarding the validity of the found simulations results and used simulation methods.

4

Cupped hands: at constant angle of attack

Chapter 2 showed that a swimmer can increase its propulsive forces by spreading its fingers, where a spreading of 5° lead to the largest increase in drag. Besides the effect of finger spreading, it is expected that cupping the hand influences the propulsive forces as well. This chapter describes the experimental procedure used to investigate the effect of cupping the hand. Starting by describing the characteristics of five full scale 3D-printed arm models that were created for this purpose. Hereafter the experimental facility (low speed wind tunnel) and force measuring system are described. Furthermore, the experimental methods and the results generated from those experiments are discussed in detail. Finally, conclusions are drawn regarding the effects on drag for varying hand cuppings.

4.1. Cupped hand models

The five full scale 3D-printed arm models consist of an equal forearm, while the hand cupping is varied. All cupped hands have a 5° finger spreading, since towing tank experiments on models with varying finger spreading found this optimal. The models are created with the open source 3D computer program MakeHuman, that is generally used for the prototyping of human models (The MakeHuman team, 2016). The program uses a detailed human skeleton including its bones and joints. The cupped shapes are created by projecting the end points of the phalanges (digital bones in the hand) on known curved shapes. The thumb is hereby fixed in its neutral (abducted) position since Schleihauf (1979) showed that thumb position on its own already has a large effect on the drag, while the present study only focusses on the effect of the fingers. The five arm models are created by a 3D-printer with a printing resolution of 120 µm (Shapeways, 2018).

Figure 4.1 shows the five created models, for convenience the different models are respectively called: *handball*, *basketball*, *neutral*, *flat* and *reverse*, the characteristics of those models are given below.

- **Handball**: the end points of the phalanges lie on a sphere with the diameter of a handball (D = 0.19 m). The sphere is placed at the hand palm side, with the end point of the middle finger's phalanx that is nearest to the hand palm fixed on it. From here the positions of all other phalanges are modified.
- **Basketball**: equal to the *handball* model, with as difference a used sphere with the diameter of a basketball (D = 0.24 m).
- **Neutral**: the phalanges are in a neutral position as generated by MakeHuman, this can be considered a hand at rest.
- **Flat**: a plane perpendicular to the hand palm intersects the end point of the middle finger's phalanx that is nearest to the hand palm. All end points of the other phalanges are projected on this same plane.
- **Reverse**: equal to the *basketball* model, with as difference a sphere with D = 0.24 m placed at the rear side of the hand, creating a hand with its fingers in a reverse direction. White (2011) shows that for a flow over the convex side of a cup a strong decrease in drag coefficient occurs compared to a flat disk. Therefore a strong decrease in drag coefficient is expected for the *reverse* hand as well.

The five arm models have an equal surface area, however the frontal projected area A changes by cupping the hand. For the calculation of force coefficients the projected area of the *neutral* model is used as a reference, i.e. effectively values $C_D A / A_{neutral}$ are compared. In this way, insight in the performance of all cupped hands relative to the *neutral* hand is obtained.

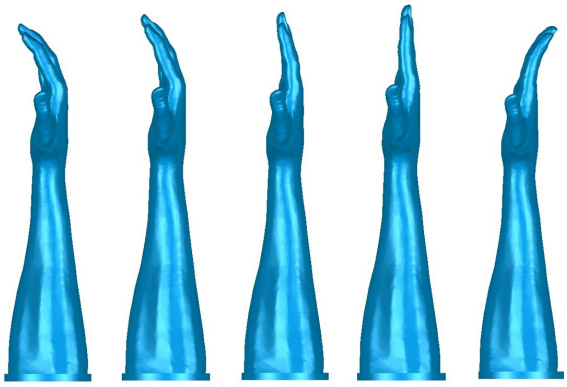

Figure 4.1: Side view of cupped hand models, from left to right respectively the *handball, basketball, neutral, flat* and *reverse* model are shown.

Table 4.1: Characteristics of the low speed wind tunnel from Eindhoven University of Technology (Willemsen, 2016).

Maximum velocity	15.5 $\mathrm{m\,s^{-1}}$
Test section height	1.1 m
Test section width	0.7 m
Test section length	8 m
Inlet turbulence level	5%

4.2. Experimental setup

Comparison of the towing tank research from chapter 2 with the wind tunnel research from van Houwelingen et al. (2016) showed that towing tank experiments are not necessarily required to find small differences in drag acting on arm models. Wind tunnel experiments have several advantages over towing tank experiments. An experimental wind tunnel campaign is less time intensive, as there is no equivalent of a free-water surface present where disturbances appear. Therefore no waiting time is required to make the disturbances stabilize before a new experiment is started. Also there are no limitations in the measuring time, as air flows continuously along the arm models. Furthermore, the forces on the arm models are reduced as the air flow is less dense, this reduces the risk of mechanical failure during the experiments. Therefore the arm models are now fully subjected to a fluid flow, which takes all effects of finger/forearm interference into account. For those reasons the experiments on cupped hands are done in a wind tunnel. This section describes the wind tunnel and force measuring system that are used to look into the effects of cupped hands.

4.2.1. Wind tunnel

In a wind tunnel the model is at a fixed position in a test section, aerodynamic forces are introduced as air flows along the model. Reynolds number scaling is used to enable the comparison of experiments performed in air and water. A closed-loop low speed wind tunnel from the department of Turbulence and Vortex Dynamics at Eindhoven University of Technology is used for this research. It reaches velocities up to 15.5 $\mathrm{m\,s^{-1}}$, giving a Reynolds number Re $\sim 10^5$ around the hand palm for a characteristic diameter $D = 0.1$ m, which is in accordance with a hand moving through water at 1 $\mathrm{m\,s^{-1}}$. This is two times lower than the Reynolds number reached during a swimming stroke and the towing tank experiments. The previous towing tank research indicated that C_D is not dependent on Reynolds numbers ranging from $0.2 \cdot 10^5 < \mathrm{Re} < 1.9 \cdot 10^5$, for this reason the limitations in wind tunnel velocity should be no limitation to finding differences in drag coefficients for the arm models. Further characteristics of the wind tunnel are given in table 4.1. Appendix C describes the calculation of flow velocity based on a measured pressure differential over the contraction of the wind tunnel.

Blockage effects

For the used wind tunnel and arm models the blockage ratio $\phi = 5.5\%$, this blockage ratio is on the boundary of $\phi < 5\%$ where Barlow et al. (1999) suggested to not use blockage correction factors. Besides, all arm models have an almost equal projected area, this gives the expectation that occurring blockage effects are equal for all arm models. Therefore, without applying blockage corrections the experiments still give insight in the relative performance of the arm models. For this reason no blockage correction factors are used.

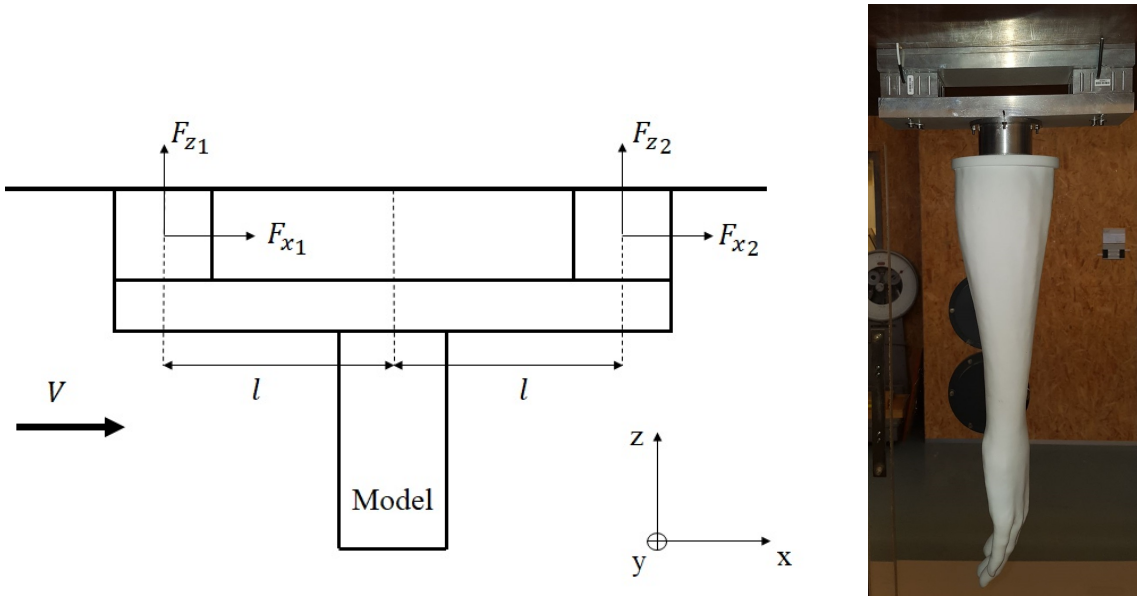

(a) (b)

Figure 4.2: (a) Gives a schematic overview of the force sensor with l = 0.1 m and (b) gives a picture of an arm model connected to it. Air flows from left to right while it generates a drag force, lift force and a drag induced moment on the arm model.

4.2.2. Force measuring system

A force measuring system is attached to the ceiling of the measurement section. It consists a configuration of two identical three-axis load cells that have a measuring capacity of 10 N in all three Cartesian directions (ME-Meßsysteme, 2016). Individual load cells have a measuring accuracy of 1%, hence their combination has one of 2%. By placing the two sensors in a tandem arrangement as shown in figure 4.2, the drag force, lift force and drag induced moment on the models can respectively be determined as

$$F_D = F_{x,1} + F_{x,2}, \tag{4.1}$$

$$F_L = F_{y,1} + F_{y,2}, \tag{4.2}$$

$$M_y = (F_{z,2} - F_{z,1})\,l. \tag{4.3}$$

Figure 4.2b shows that the force sensor is located inside the measuring section itself. The rectangular shaped force sensor is considered a bluff body, an air flow along it introduces significant drag forces. Especially forces $F_{x,1}$ and $F_{x,2}$ are introduced as the flow is assumed purely uniform in the x-direction. These forces are considered independent of the attached arm model, as no interference between the flow around the force sensor and arm models is expected. Willemsen (2016) investigated the velocity profile along the height of the currently used wind tunnel. Figure 4.3 shows there is a boundary layer thickness of around 0.15 - 0.20 m. The force sensor has a total height of 0.05 m, hence it is completely immersed in the low velocity boundary layer. The arm models are connected to the force sensor with a cylindrical shaped adapter with a height of 0.04 m. Due to the spacing given by the adapter it is assumed that the low velocity flow along the force sensor is not interfering with the flow around the hands. As a result, forces acting on the hands are only a result of the uniform fluid flow along them.

Statically indeterminate

A possible complication is found in the force measuring system as the two load cells are connected with a rigid beam. This makes the construction statically indeterminate, as there are more unknown internal forces than equilibrium equations. The construction is restricted to deform when external forces and temperature variations are introduced. Deformations caused by external forces and temperature fluctuations are respectively given as ΔL_T and ΔL_F, where

$$\Delta L_F = \frac{F L_0}{AE}$$

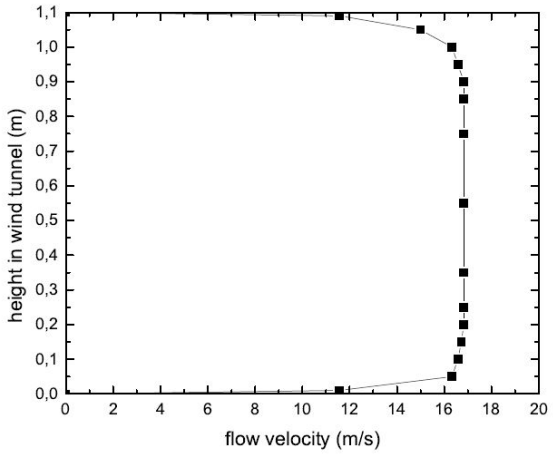

Figure 4.3: The velocity profile along the height of the wind tunnel. It can be noticed that the boundary layer thickness at the top of the wind tunnel is slightly larger than at the bottom Willemsen (2016).

and

$$\Delta L_T = \alpha L_0 \Delta T.$$

Here F is the applied force and ΔT the experienced temperature difference. Furthermore, L_0, A, E and α correspond to the initial length, cross-sectional area, elastic modulus and coefficient of thermal expansion of the beam, respectively. The used load cells have a rated displacement of 0.1 mm at the maximum force (ME-Meßsysteme, 2016). The expected deformations ΔL_F and ΔL_T are much smaller than the rated displacement. For this reason it is expected that the deformations are not influencing the measured forces, hence it is decided to continue the experiments with this statistically indeterminate force measuring system.

The 2% accuracy of the force measuring system could be improved by using one load cell instead of the tandem arrangement. In this way a measuring accuracy of 1% remains, however insight on drag induced moments is no longer available, and effects of crosstalk in the measured forces are enhanced. As an alternative, the tandem arrangement can be improved by making it statically determinate. Replacing one of the supports that connects the rigid beam to the load cells by a roller, is an option to make it statically determinate.

4.3. Experimental methods

For all arm models the experiments are performed at a variety flow velocities, i.e. $0.4 \cdot 10^5 < \mathrm{Re} < 10^5$. Measurements are performed in an order of increasing velocity. In this way boundary layer development takes place similarly around the different arm models, with no influences of velocity induced hysteresis. By waiting 2 minutes after increasing the velocity it is made sure that flow velocity is completely converged inside the tunnel. Hereafter forces and pressure are measured for 5 minutes with a sampling frequency of 205 Hz. For the *handball* and *basketball* models the experiments are performed twice, with remounting the models in between. In this way the repeatability of the experiments is investigated. The arm models are always mounted with the hand palm perpendicular to the flow, as previous research showed this position is optimal for maximizing drag forces (Takagi et al., 2001).

At the start of a measuring campaign, the wind tunnel is first run for 15 minutes such that a constant air temperature inside the tunnel is obtained. No larger temperature fluctuations than 0.5°C were observed during the experiments by following this procedure, hence the flow properties become nearly constant. Both the density and viscosity of the air are assumed to be constant during the experiments at $\rho = 1.18\ \mathrm{kg\,m^{-3}}$ and $\nu = 15.6 \cdot 10^{-6}\ \mathrm{m^2\,s^{-1}}$. Taking the temperature fluctuations of 0.5°C into account would lead to variations in $C_D < 0.2\%$, and variations in $\mathrm{Re} < 0.3\%$.

4.4. Results and discussion

Forces are measured at varying Reynolds numbers for the different arm models. Corresponding drag and lift coefficients are presented in figure 4.4. Experiments for the *handball* and *basketball* models are performed

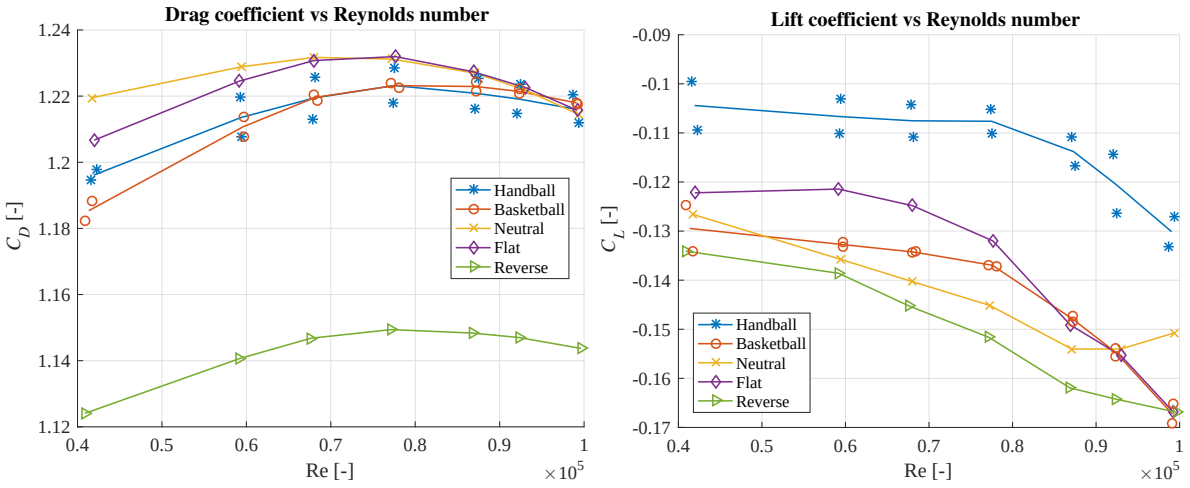

(a) (b)

Figure 4.4: A presentation of the drag coefficients (a) and lift coefficients (b) for the different arm models as a function of Reynolds number. For all coefficients the projected area of the *neutral* is used.

twice, the repeatability of the experiments is discussed. In figure 4.4b the data points corresponding to repeated experiments are presented with markers, with a line plotted through the mean value.

Drag coefficient

Figure 4.4a shows that drag coefficients are following identical trends for all arm models, with a maximum around Re = $7.5 \cdot 10^5$. The drag coefficient appears to start decreasing for Re > 10^5, this is possibly due to the start of a drag crisis around the cylindrically shaped forearm. The existence of a drag crisis could not be confirmed due to the limited maximum flow velocity. Variations in C_D of ~ 3% are found for the investigated range of Reynolds numbers, this indicates that C_D is approximately Reynold number independent.

The hypothesis that a *reverse* hand shape is disadvantageous orientation for maximizing propulsion is confirmed by figure 4.4a, for all Reynolds numbers a significant lower drag coefficient is obtained compared to the other arm models (≈ 8% lower). The *basketball* and *handball* hand shapes tend to follow identical C_D curves, with only small differences in C_D for the two lowest Reynolds numbers. This is possibly a result of the low resolution of the force measurements at low velocities. Similarly, C_D curves for the *neutral* and *flat* shapes are following identical trends, for those hand shapes a largest drag is obtained for Re < $0.9 \cdot 10^5$. Those hand shapes are accountable for 0.4% - 0.9% more drag compared to the cupped hands for Reynolds numbers ranging from $0.7 \cdot 10^5$ < Re < $0.9 \cdot 10^5$. For Re > $0.9 \cdot 10^5$, the differences in C_D become very small, it appears that the *basketball* model obtains largest drag for further increasing Reynolds numbers, measurements at higher Reynolds numbers are needed for confirmation.

Lift coefficient

The arm models were orientated with the hand palm perpendicular to the flow. Previous research suggested that $C_L \approx 0$ for this orientation. Figure 4.4b presents the lift coefficient for varying Reynolds numbers, it shows that $C_L \neq 0$ in this orientation. In contrast to C_D, no Reynolds number independent effect is observed for C_L, where $|C_L|$ increases for increasing Reynolds number. As the current used angle of attack φ_z is not resulting in zero lift, there should exist a rotated orientation that gives $C_L = 0$.

Similarity in drag coefficients was found for the pairs *handball* - *basketball* and *neutral* - *flat*. However, within those pairs significant differences in C_L are observed, around 20% and 10%, respectively. The drag coefficient for the *neutral* hand is likely to increase more at zero lift than for the *flat* hand, while C_D for *basketball* increases more than for *handball*. This indicates that drag curves would deviate strongly from 4.4a when experiments are performed at an orientation where $C_L = 0$.

Repeatability

Experiments are performed twice for the *handball* and *basketball* models. Figure 4.4 included the data points of the repeated experiments. The experiments for the *basketball* model are very accurately repeated, with

differences in $C_{D,L}$ smaller than 0.3%. In contrary, for the *handball* model, large differences in C_D up to 1% are observed. It shows that one of the *handball* data sets reaches significantly higher drag coefficients than the *basketball*, while the other data set reaches significantly lower C_D than the *basketball* model. It appears that the used force measuring system is not very well suitable to compare drag coefficients of the arm models, as repeating the experiments can lead to considerably different conclusions. Furthermore, deviations in C_L are even larger for the *handball* model, being of an order 10%. However, there is still a clear distinction between the C_L curves of all arm models.

4.5. Conclusion

This chapter investigated the effects of hand cupping on drag and lift coefficients. Firstly, the *reverse* hand shape was found strongly disadvantageous, leading to around 8% less drag compared to the other hand shapes. The research indicates that a *flat* and *neutral* hand are preferred for maximizing drag forces. These two hand models lead to approximately 0.4% to 0.9% larger drag, compared to the *basketball* and *handball* hand shapes.

In contrary to previous research, zero lift was not found while the hand palm was orientated perpendicular to the flow. For the different arm models, the observed differences in C_L are large in comparison to the differences in C_L. It is unlikely that the currently found trend in C_D for the arm models is maintained at varying angles of attack. Unfortunately the used force measuring system lacks the possibility to change the angle of attack easily.

Previous research found no Reynolds number dependent effects on C_D for arm models. The current study found small variations up to 3% in C_D for the investigated range of Reynolds numbers, indicating that C_D is approximately Reynolds number independent. It seems that C_D starts decreasing for $\mathrm{Re} > 10^5$, this is possibly due to the start of a drag crisis around the cylindrically shaped forearm. The existence of a drag crisis could not be confirmed due to the limited maximum flow velocity. For future research it would be interesting to look into the behaviour of C_D at $\mathrm{Re} > 10^5$.

Experiments for the *basketball* and *handball* models were done twice. Repetition of the experiments lead to maximum deviations in the drag coefficient of 1%. These deviations are of the same magnitude as differences in C_D between the different arm models. This indicates that the used force measuring system might not be sufficient to find the small differences in drag forces on the arm models.

The observed measuring inaccuracies, in combination with the small differences in drag experienced by the arm models, make it hard to draw conclusions on the propulsive performance of the cupped hands. The only observation that stands out is that the *reverse* model leads to drastically lower drag coefficients. It is useful to redo the experiments on cupped hands, preferably in a wind tunnel with a larger test section that reaches higher flow velocities. In this way the occurrence of blockage effects is reduced, and the effects of increased Reynolds numbers can be investigated. Furthermore, an external force measuring system located outside the test section is preferred, such that it does not interfere with the fluid flow. Also a more accurate force measuring system is preferred to reduce the effect of random errors and make measurements more reliable. Lastly, a force measuring system that can vary the angle of attack easily would be a nice addition, such that effects of drag and lift for varying angles of attack can be investigated. A wind tunnel available at TU Delft fulfils these requirements and was used to redo the experiments. The results are presented in chapter 5.

5

Cupped hands: at varying angles of attack

The experimental setup used in chapter 4 had several downsides for the measurement of aerodynamic forces acting on the arm models. For this reason the experiments on the cupped hands are repeated in another, larger wind tunnel that reaches higher flow velocities. This wind tunnel also contains a more accurate force measuring system. This chapter describes the used wind tunnel and its force measuring system. Subsequently, the experimental methods are described, whereafter a discussion of the experimental results takes place. Finally, conclusions are drawn regarding the effects on drag for varying hand cuppings.

5.1. Experimental setup

The experimental investigation was carried out in the Low Turbulence Tunnel (LTT) at TU Delft, a wind tunnel that is often used for research towards drag and lift. For example, Timmer & van Rooij (2003) used it for research towards force coefficients for a large variety of airfoils that play an important role in the design of wind turbines. The LTT is an atmospheric tunnel of the closed-throat single-return type and is illustrated in figure 5.1a, where figure 5.1b shows a photo of its test section and contraction.

Further properties of the tunnel are given in table 5.1, due to its large contraction ratio a very low free-stream turbulence level is obtained in the test section. Flow properties (density and viscosity) are controlled by cooling the corner vanes (Timmer & van Rooij, 2003). The wind tunnel consists of techniques to vary the angle of attack with $< 0.5°$ precision (Lentink et al., 2007). The next subsections describe the force measuring system, data acquisition, and the relevance of blockage and wall correction methods.

5.1.1. Force measuring system

As shown in figure 5.1a, an external six-component balance is located directly above the test section, a detailed sketch of this balance system is given in figure D.1 from appendix D. Figure 5.2b illustrates just the test section and its corresponding coordinate system. Figure 5.2a shows an arm model attached to a turntable plate at the ceiling of the wind tunnel. The turntable plate is directly connected to the balance system, such that the angle of attack of the model is variable by rotating the balance system. Forces and moments acting on the model are via the ceiling reflected to the balance system, such that the system has to rebalance itself continuously when different forces and moments are applied. This rebalancing takes place by six stepper motors translating six individual weighbeams. The forces and moments acting on the model are determined based on the amount of steps taken by the stepper motors. They are determined with an accuracy of 0.01 N/0.01 N m along the axis of the rotated frame of reference of the balance system.

Table 5.1: Characteristics of the Low Turbulence Tunnel from TU Delft (Timmer & van Rooij, 2003).

Maximum velocity	120 m s^{-1}
Total circuit length	72.7 m
Test section height	1.25 m
Test section width	1.80 m
Test section length	2.60 m
Contraction ratio	17.8
Inlet turbulence level	0.015% at 20 m s^{-1}

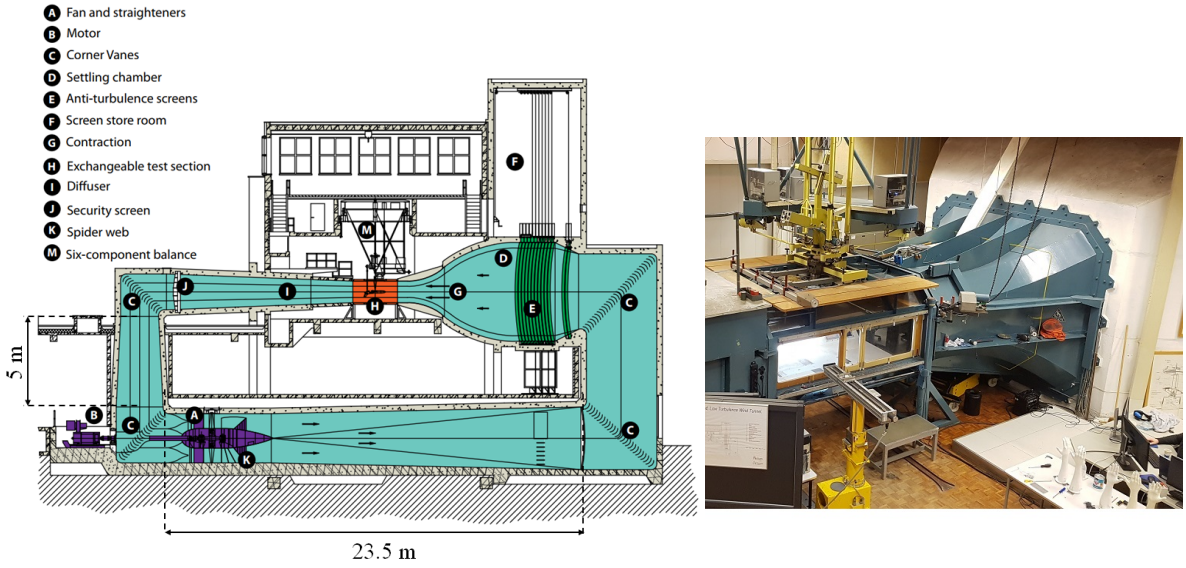

(a) (b)

Figure 5.1: (a) Gives an illustration of the Low Turbulence Tunnel with some characteristic dimensions and its components (Dimchev, 2012). (b) Shows the test section (H) and contraction (G) of the LTT.

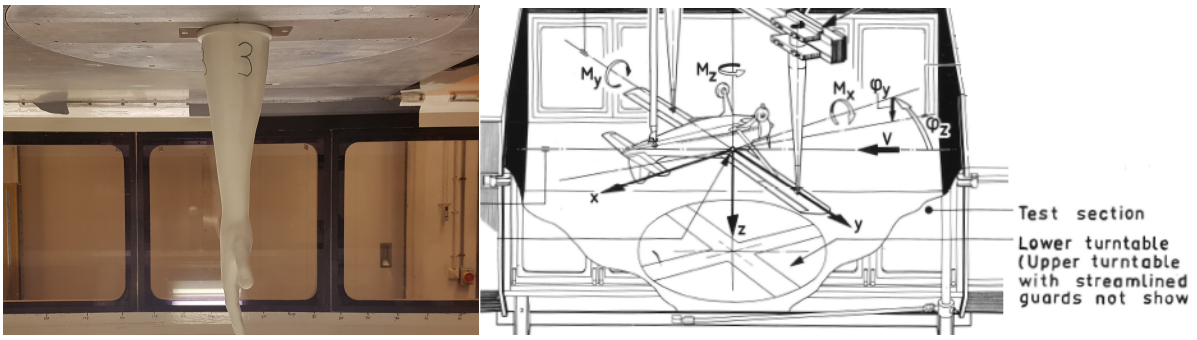

(a) (b)

Figure 5.2: Overview of the wind tunnel test section. (a) Shows an arm model attached to the turntable plate with $\varphi_z = 0°$. (b) Gives an illustration of the coordinate system inside the test section. Air flows from right to left with velocity V. Positive x-, y- and z-forces are respectively directed to the left, out of the paper and downwards (Dimchev, 2012).

As shown in figure 5.2b, air flows from right to left with a velocity V. The Cartesian coordinate system is directed in the rotated frame of reference of the balance system. Figure 5.2b shows the definition of angle of attack φ_z, where for positive φ_z the thumb has a leading position upstream in the flow. For $\varphi_z = 0°$, the x-axis points in the streamwise direction, with the y-axis perpendicular to it and the z-axis in the gravitational direction. This results in the measurement of the forces F_x, F_y and F_z, as well the moments M_x, M_y and M_z. For further processing these forces and moments are decomposed in the tunnel axis itself.

5.1.2. Data acquisition

Translations of the six stepper motors, flow temperature, angle of attack and the pressure difference over the contraction cone are measured quantities during the experiments. Acquisition of these quantities takes place with the CompactRio embedded controller from National Instruments. The data is further processed with a National Instruments LabVIEW programme. Forces and moments acting on the models, flow properties and flow velocity follow from the processing.

5.1.3. Blockage effects

Inside the LTT the arm models have a blockage ratio ϕ = 1.9%. Barlow et al. (1999) suggested to not use blockage correction factors for $\phi < 5\%$. Therefore no blockage correction methods are applied during this research.

5.1.4. Wind tunnel wall effects

The walls of the LTT can be considered as flat plates along which boundary layers grow, as illustrated in figure 1.2. For such boundary layer a Reynolds number is defined as $\mathrm{Re}_x = Vx/\nu$, where V is the free-stream velocity and x is a specified location downstream. When a flow with low turbulent intensity passes along a smooth wall, the boundary layer transits from laminar to turbulent for $\mathrm{Re}_x \sim 5 \cdot 10^6$ (Kundu et al., 2015). Therefore, the boundary layer around the walls of the LTT at the location of the arm model (x = 2.5 m) is laminar for all investigated velocities. Hence, the boundary layer thickness can be approximated with the Blasius profile (White, 2011). This gives the boundary layer thickness along a flat plate as

$$\delta \approx 5.0x/\sqrt{\mathrm{Re}_x} \tag{5.1}$$

where $\delta \approx 0.01$m for $\mathrm{Re}_x = 1.8 \cdot 10^6$, x = 2.5 m and V = 10 m s^{-1}. The boundary layer thickness δ becomes even smaller at higher flow velocities V. This indicates that the boundary layer thickness δ is negligible in comparison to the 0.5 m height of the arm model, therefore no flow interference between the boundary layer and the hands is expected. For this reason no corrections are applied to compensate for wall effects.

Vertical force predictions

Vertical forces F_z are experienced on the arm models when subjected to a fluid flow. An enhancement in the force F_z is experienced by mounting the arm models directly to the ceiling of the LTT, in comparison to mounting them to the ceiling via a strut. The enhancement in F_z is of the same principle as vertical force that is experienced on a hemisphere attached to a flat plate, illustrated in figure 5.3a. Streamlines move both along and over the hemisphere when subjected to a fluid flow. This introduces a high velocity flow at the top of the hemisphere, leading to a low pressure region. This introduces a vertical force that is directed upwards. For an irrational flow, the pressure coefficient on the surface of the hemisphere is given as

$$C_P = \frac{p - p_\infty}{\frac{1}{2}\rho V^2} = 1 - \frac{9}{4}\sin^2\theta, \tag{5.2}$$

where $0 \leq \theta \leq \pi$ (Yu, 2010). Then by integrating C_P over the surface area of the hemisphere a vertical force is found as

$$F_z = \frac{11}{32}\pi\rho\left(\frac{D}{2}\right)^2 V^2, \tag{5.3}$$

where D is the diameter of the hemisphere. In a similar fashion, vertical forces are introduced on the arm models, where the forearm has a diameter D = 0.1 m. The magnitude of the vertical forces F_z can be expressed as a function of the drag forces F_D. By use of equations 1.2 and 5.3 then follows $F_z \approx 0.4F_D$.

Figure 5.3b illustrates the predicted vertical force F_z from equation 5.3. Furthermore, forces F_D, F_L and F_z measured during the experiments are presented. It appears that the predicted vertical forces are in agreement with the measured forces, and that $F_z \approx 0.4F_D$ is a good estimate. This indicates that the forces F_z on the arm models are caused according to the principle found for the hemisphere. Thus, a low pressure region is experienced underneath the hand, resulting in a vertical suction force.

5.2. Experimental methods

The LTT reaches higher flow velocities than the wind tunnel used in chapter 4, making Reynolds number scaling possible for actual front crawl swimming stroke velocities. During previous experiments, the arm models were always positioned with the hand palm perpendicular to the flow (φ_z = 0°). This orientation maximizes the projected area of the arm models, leading to the assumption that drag forces and moments are maximized as well. However, the results from chapter 4 showed that this is not an orientation where zero lift occurs, hence it is expected that a maximum drag occurs at a different angle of attack. As mentioned, the LTT contains a rotatable balance system, making the angle of attack of the models variable. In this way it is investigated whether having the hand palm perpendicular to the flow is optimal.

Table 5.2 gives an overview of the arm models for which aerodynamic forces and moments are investigated, furthermore it shows the velocities and angles of attack for which this is done. The *reverse* model is left out, since previous research in chapter 4 already showed this is a disadvantageous hand shape.

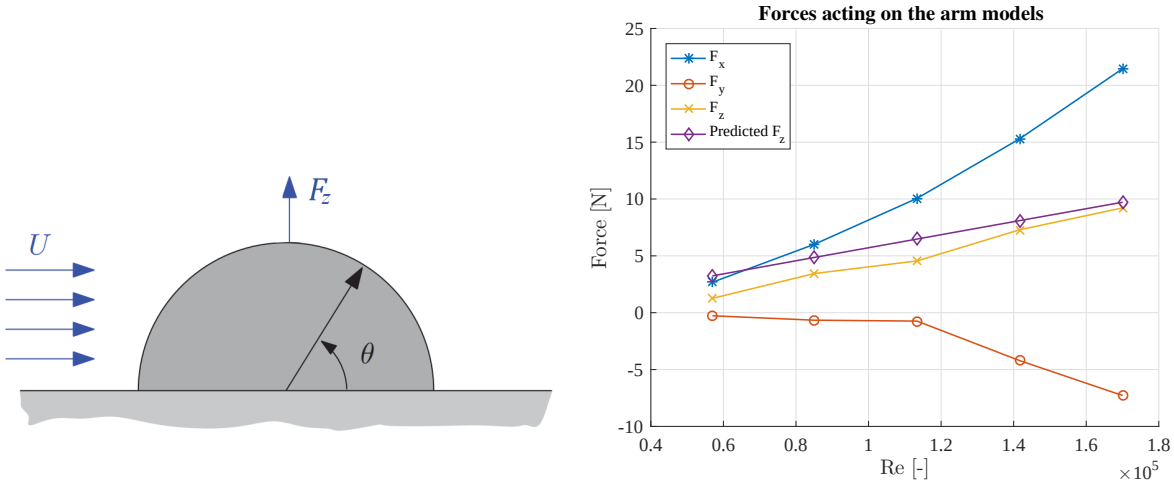

(a) (b)

Figure 5.3: (a) Gives an illustration of a flow field along a hemisphere attached to a flat plate, which introduces a vertical force F_z. Modified from Yu (2010). In (b) an overview of forces acting on the *neutral* arm model are presented, here $\varphi_z = 0°$. Furthermore, the predicted vertical force F_z is illustrated.

Table 5.2: Overview of arm models, flow velocities and angles of attack that are investigated during the experiments in the LTT. Velocities correspond to $0.6 \cdot 10^5 < \text{Re} < 1.7 \cdot 10^5$

Arm model		Handball, Basketball, Neutral, Flat
Velocity	[m s^{-1}]	0, 10, 15, 20, 25, 30
Angle of attack	[°]	-15, -10, -8, -6, -4, -2, 0, 2, 4, 6, 8, 10, 12, 14, 18, 22, 26, 30, 34, 38

5.2.1. Calibration of resistances acting on turntable plate

A calibration procedure is required before doing experiments for the cases from table 5.2. Figure 5.2a shows an arm model mounted to the turntable plate, both the model and turntable plate have a contribution to the total measured aerodynamic resistances. By doing experiments at all velocities and angles of attack from 5.2 with no arm model mounted, the effect of the turntable plate itself is investigated. Results from this analysis are shown in figure 5.4. The projected area of the arm models is used, such that statements regarding the influence of the turntable plate on the total drag can be made. The drag coefficient C_D shows a constant behaviour for angle of attack, which is a result of the axisymmetrical shape of the turntable plate. The plate experiences a drag force due to the boundary layer growth in its streamwise direction. This boundary layer growth introduces wall shear stresses on the plate, where the stresses reduce in size as the boundary layer grows thicker. The plate experiences drag due to the skin friction that the shear stresses introduce. Previous research showed for arm models $C_D \sim 1$, hence the turntable plate itself is accountable for $\sim 4\%$ of the total drag. Therefore it is of importance to subtract the resistance turntable plate from that found for the arm models mounted to it.

Since there is a uniform flow in the x-direction, expectations would be that the boundary layer grows uniformly in x-direction, with no variations in y-direction. This would mean that no wall shear stress is observed in y-direction, such that zero lift is observed, this is not true according to figure 5.4b. Apparently there are disturbances in for example the wind tunnel ceiling that cause small local velocity components in the y-direction, resulting in $C_L \neq 0$.

5.2.2. Flow induced hysteresis

Chapter 1 introduced the effects of hysteresis in the fluid flow, which is likely to apply to the arm models as well. As the arm models are geometrically complex shaped, flow separation can occur at various sections of the models, i.e. around the hand and forearm. It is expected that changing the angle of attack has effect on the occurrence of flow separation at the different sections of the arm. The forearm has similarities in shape with a cylinder, hence flow separation is occurring independent of the angle of attack. The same holds for the hand with its palm perpendicular to the flow, however by increasing the angle of attack the hand becomes more of a streamlined body, where the flow might start to attach. This makes it likely that hysteresis as observed for an airfoil described in chapter 1 occurs around the arm models. To exclude effects of hysteresis during

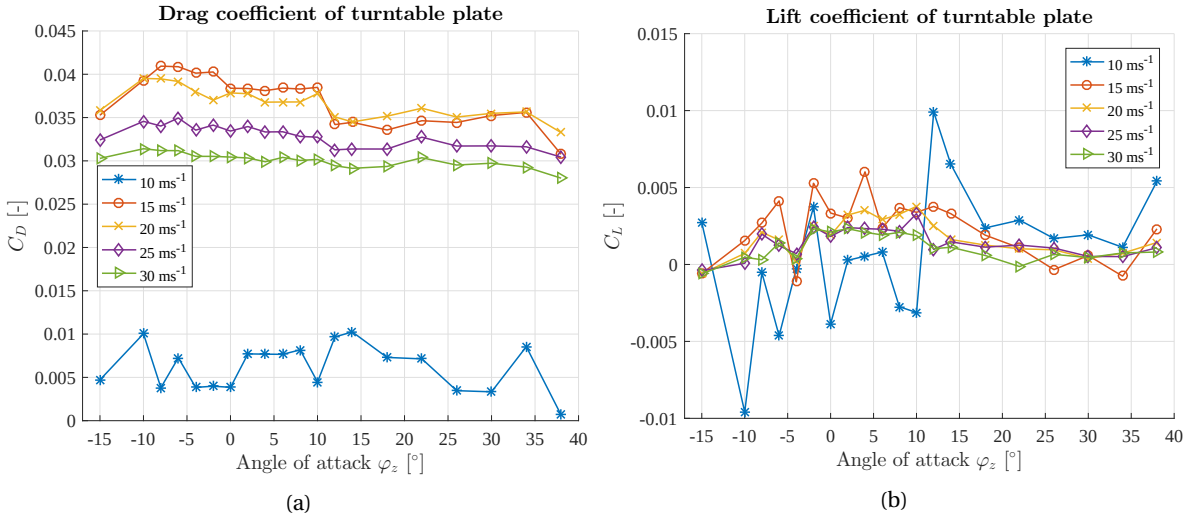

(a) (b)

Figure 5.4: Drag and lift coefficients of the turntable plate itself, here the projected area $A = 0.042$ m^2 of the arm models is used.

Table 5.3: Overview of the used wind tunnel flow velocities that are investigated and their corresponding Reynolds number. Furthermore, the corresponding velocities in water are given for a water temperature of 15°C.

Air flow velocity [m s^{-1}]	Reynolds number [-]	Water flow velocity [m s^{-1}]
10	$0.6 \cdot 10^5$	0.7
15	$0.9 \cdot 10^5$	1.0
20	$1.1 \cdot 10^5$	1.3
25	$1.4 \cdot 10^5$	1.6
30	$1.7 \cdot 10^5$	1.9

the experiments, the angle of attack is always set to $\varphi_z = -15°$ at the start, whereafter increments are made until $\varphi_z = 38°$. Hence experiments are not performed in a randomized order due to these considerations in hysteresis.

After increasing the angle of attack the flow, measurements are started after 10 s, such that the flow around the arm becomes stable. Then with a measuring time of 20 seconds and a sampling frequency of 4 Hz the forces and moments are determined.

5.3. Results and discussion

Experiments are carried out for the cases of table 5.2. This section presents the found effects on the drag and lift coefficients for varying Reynolds numbers and angles of attack. Furthermore, drag and lift coefficients are shown a function of Reynolds number at $\varphi_z = 0°$. Also the maximum drag coefficient and the drag coefficient at zero lift are presented as function of Reynolds number. The performance of each hand cupping over the velocity domain of a swimming stroke is investigated. This is done by taking weighted averages of the drag coefficients over the investigated range of Reynolds numbers. In appendix E, a method is described that determines the point of application of force on the arm models.

5.3.1. Force coefficients versus angle of attack

Experiments are performed at the flow velocities and angles of attack from table 5.2. Drag and lift coefficients found from the experiments are shown as a function of angle attack in figures 5.5 – 5.9. Table 5.3 gives an overview of the Reynolds number corresponding to the investigated flow velocities, furthermore the corresponding velocities for experiments in water are presented. Force coefficients are based on the frontal projected area of the *neutral* model at zero angle of attack, since this is the reference case to which differences in force coefficients are compared. Therefore, effectively comparison of values $C_D A / A_{neutral}$ takes place.

In contrast to previous research of Schleihauf (1979) and (Takagi et al., 2001), it is clear that the maximum value in drag coefficient is never found at $\varphi_z = 0°$, at which the hand palm is perpendicular to the flow. Instead, a maximum drag coefficient is always found at $\varphi_z > 0°$, where the thumb is leading. The lift coefficient

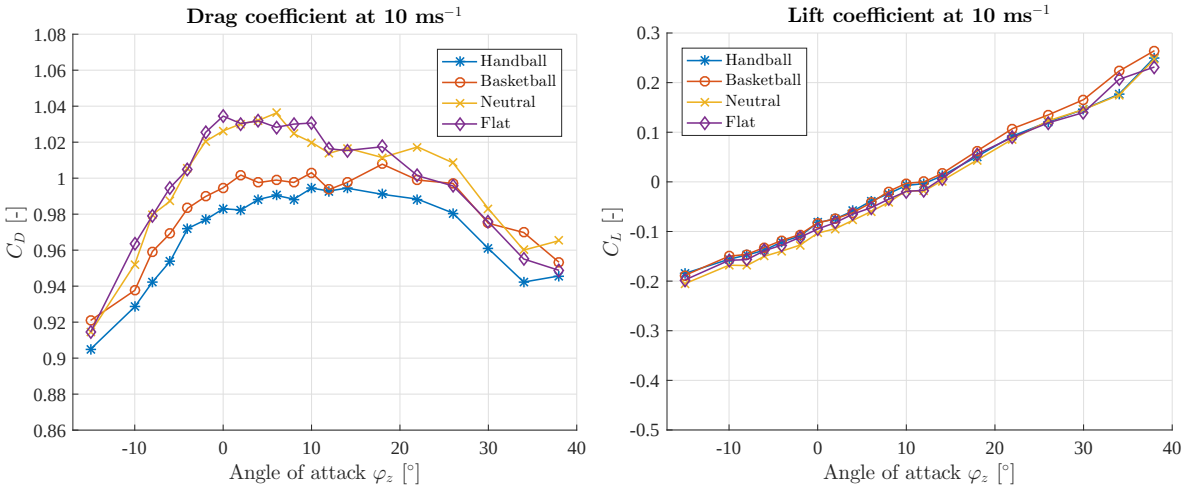

(a) (b)

Figure 5.5: Drag and lift coefficient as function of the angle of attack at 10 m s^{-1}, Re $\approx 0.6 \cdot 10^5$.

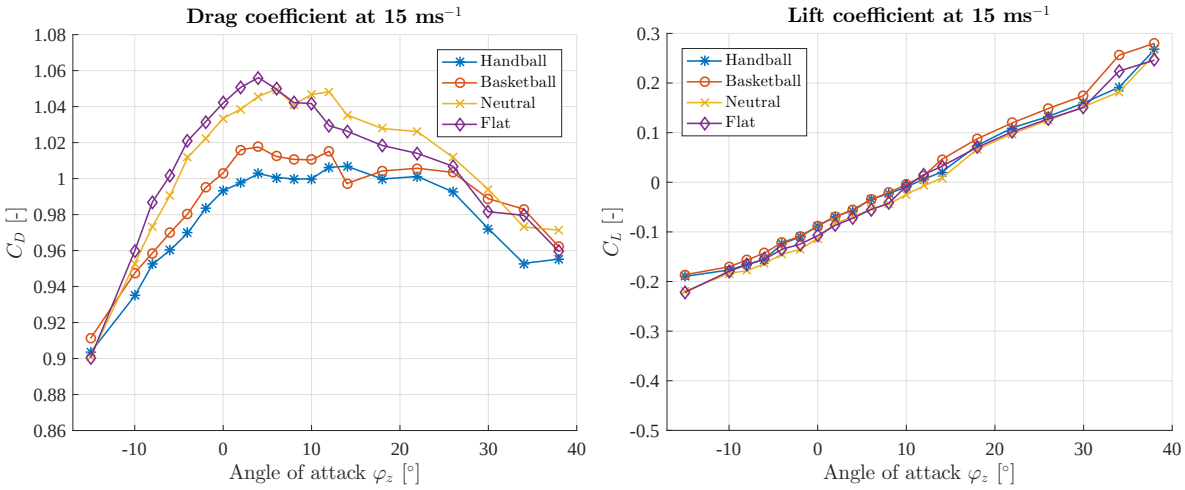

(a) (b)

Figure 5.6: Drag and lift coefficient as function of the angle of attack at 15 m s^{-1}, Re $\approx 0.9 \cdot 10^5$.

is observed to always increase from negative to positive for increasing φ_z, but zero lift never occurs at $\varphi_z = 0°$.

Force coefficients at 10 m s^{-1} and 15 m s^{-1}

As can be observed from figures 5.5 and 5.6, drag and lift curves for 10 m s^{-1} and 15 m s^{-1} are following similar trends, therefore their discussion is combined. At negative angles of attack the little finger is leading upstream in the flow, while for positive angles the thumb is leading. Drag coefficients of all arm models have a parabolic shape, with a maximum somewhere in the range of $\varphi_z = 0 - 14°$. There is a clear distinction in magnitude of C_D curves from the different hand shapes. The *neutral* and *flat* hands are responsible for most drag, and cupping the hand gives a significant decrease in C_D. In the same way an increase in lift coefficient is seen for increasing angle of attack, where $C_L = 0$ around $\varphi_z = 10 - 14°$. Thus, there is an angle of attack at which no shear forces are experienced by the arm. In this case a swimmer does not have to put in effort to compensate for its hand being pulled away by the flow, saving him energy.

Force coefficients at 20 m s^{-1}

Figure 5.7 shows the drag and lift coefficient at 20 m s^{-1}. The values of C_D and C_L are comparable to those at the velocities 10 m s^{-1} and 15 m s^{-1}. However, no clear parabolic shape can be observed for C_D as for the lower velocities. For $\varphi_z = 8 - 14°$ a local minimum occurs in both C_D and C_L. Due to this local minimum in

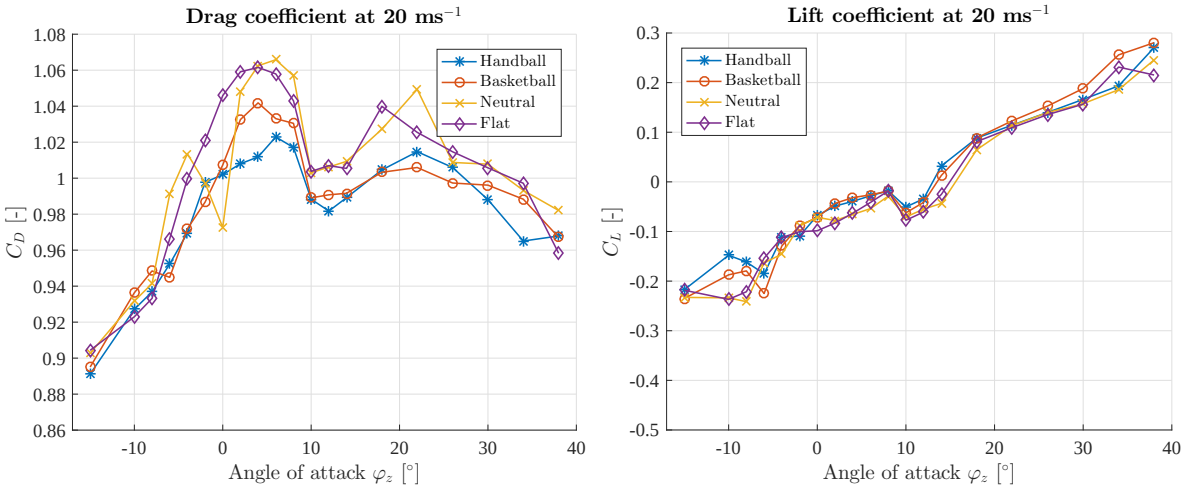

(a) (b)

Figure 5.7: Drag and lift coefficient as function of the angle of attack at 20 m s^{-1}, Re $\approx 1.1 \cdot 10^5$.

C_L the occurrence of zero lift now shifts to a larger angle of attack of $\varphi_z = 14 - 18°$.

A possible reason behind the local minimum in C_D could be an effect of drag crisis. As mentioned in chapter 1, for smooth cylinders a drag crisis is observed around Re $= 3 \cdot 10^5$, where C_D drops from 1.2 to 0.3 (Hoerner, 1965). A much smaller drop is observed for the arm models (1.06 to 0.1), which finds its explanation in the large influence of the hand on the drag coefficient. Therefore a drag crisis around the forearm would lead to a relatively small decrease in total drag coefficient for the complete hand/forearm model. The reason for the drag crisis to occur only at a specific range of φ_z might be found in the interaction of the complex hand shape and the forearm. For positive φ_z the thumb is leading upstream, vortices shed from the thumb later on move around the hand and forearm. Hence the turbulent intensity of the flow is increased due to the thumb, which influences the hand and forearm differently than a purely uniform flow. This results possibly in a specific range of φ_z where effects of a drag crisis are observed.

Subsection 1.2.2 introduced the principle of wall roughness and its effects on boundary layer transition. For the arm models the resolution of the 3D-printer is used as roughness height ($h = 120\,\mu$m). Then with $u_* = V/15$ and $V = 20$ m s^{-1} follows $\mathrm{Re}_* = hu_*/\nu \approx 11 > 1$. This indicates that the arm models have a rough wall, making its roughness elements dominating in the flow separation. The found decrease in drag coefficients occurs at a different Reynolds number (Re $= 1.15 \cdot 10^5$) than for a smooth cylinder (Re $= 3 \cdot 10^5$), this can be an explanation of wall roughness. The effects of wall roughness, in combination with interference of the flow around the fingers and forearm, and the forearm not being perfectly cylindrical shaped, gives a possible reason for the decrease in drag coefficient occurring at a lower Reynolds number than for a smooth circular cylinder.

Force coefficients at 25 m s^{-1}

Drag and lift curves become more unstructured at 25 m s^{-1}, where even less of a parabolic shape in C_D is present. Again two local maxima are present as was seen for 20 m s^{-1}. However, for the *handball, basketball* and *neutral* hands the first maximum is now lower than the second maximum. Furthermore, the location of the first maximum has shifted to $\varphi_z = 10 - 20°$. The optimum from the second maximum is found for very large angles of attack, around $\varphi_z = 25 - 35°$. In contrary to lower flow velocities, the maxima in C_D are not obtained around $C_L = 0$. In addition, there is a maximum in C_L as well around $\varphi_z = 0 - 10°$, this results in three angles of attack where $C_L = 0$.

The drag coefficients of the *flat* hand are strongly deviating for $\varphi_z = 0 - 10°$, where it reaches a significantly larger maximum C_D than the other hand shapes. For increasing angles of attack the curve follows similar patterns as the *handball, basketball* and *neutral* models. Similarly, a strong deviation in lift coefficient is observed for $\varphi_z = 0 - 10°$.

The local minimum in drag coefficient could again be an effect of drag crisis. The relative difference between the maximum and minimum is smaller than for 20 m s^{-1}, but the absolute value of C_D in the local minimum decreased even further compared to 20 m s^{-1}. This is an observation that agrees with the hypothe-

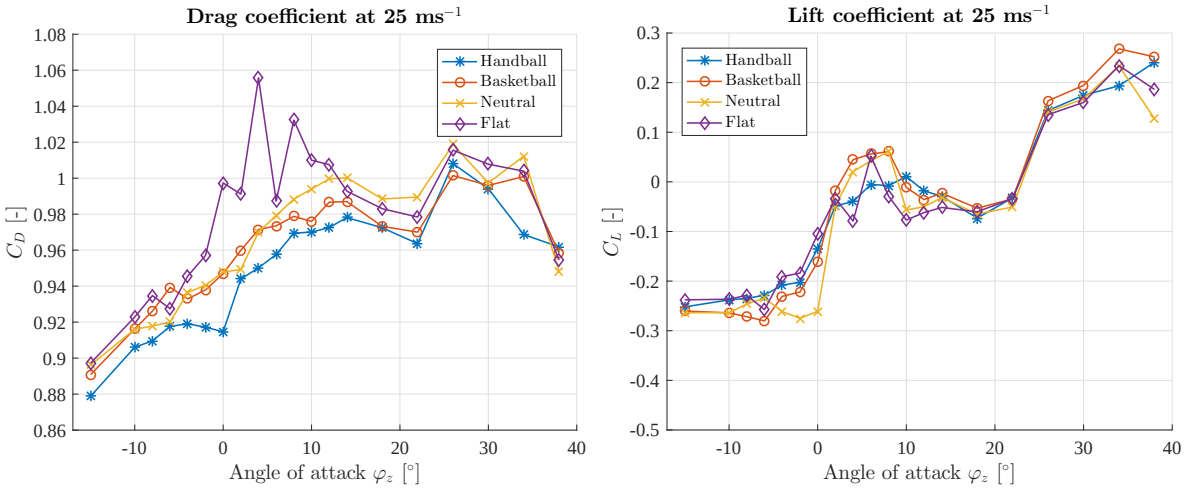

(a) (b)

Figure 5.8: Drag and lift coefficient as function of the angle of attack at 25 m s^{-1}, Re $\approx 1.4 \cdot 10^5$.

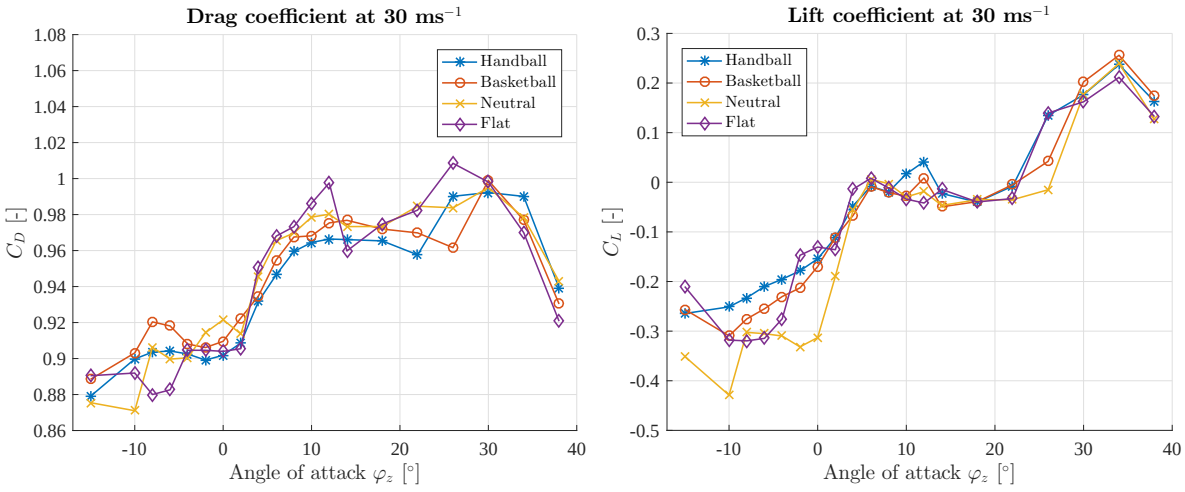

(a) (b)

Figure 5.9: Drag and lift coefficient as function of the angle of attack at 30 m s^{-1}, Re $\approx 1.7 \cdot 10^5$.

ses of a drag crisis.

Force coefficients at 30 m s^{-1}

Increasing the velocity further leads to an even lower drag coefficient of $C_D \approx 0.9$ at $\varphi_z = 0°$, compared to $C_D \approx 1.0$ at 10 m s^{-1}. The optimum in C_D again shifted to even larger angles of attack, where not so much of a local minimum is observed in C_D as for 25 m s^{-1}. There are now two phases in which C_D increases, between $\varphi_z = 10 - 20°$ it reaches a plateau after which it increases further between $\varphi_z = 20 - 30°$. The value of C_D eventually drops again for larger angles of attack. The continuous shift in φ_z where the maximum in C_D is found for increasing Reynolds number gives the impression that at a certain Reynolds number the maximum in C_D would be found with the hand palm parallel to the airflow. Which would be unlikely since this gives a fairly streamlined shape and strong decrease in projected area A. Again the plot of the lift coefficient is fairly chaotic, where a flat region exists for $\varphi_z = 5 - 20°$ where $C_L \approx 0$.

Effects of hysteresis

Subsection 1.3.2 presented the effects of hysteresis in the fluid flow for an airfoil at varying angle of attack. Similar effects of hysteresis were observed for the experiments around the cupped hands. To look into the effects of hysteresis, the effects on C_D for decreasing angle of attack were investigated. Significant differences

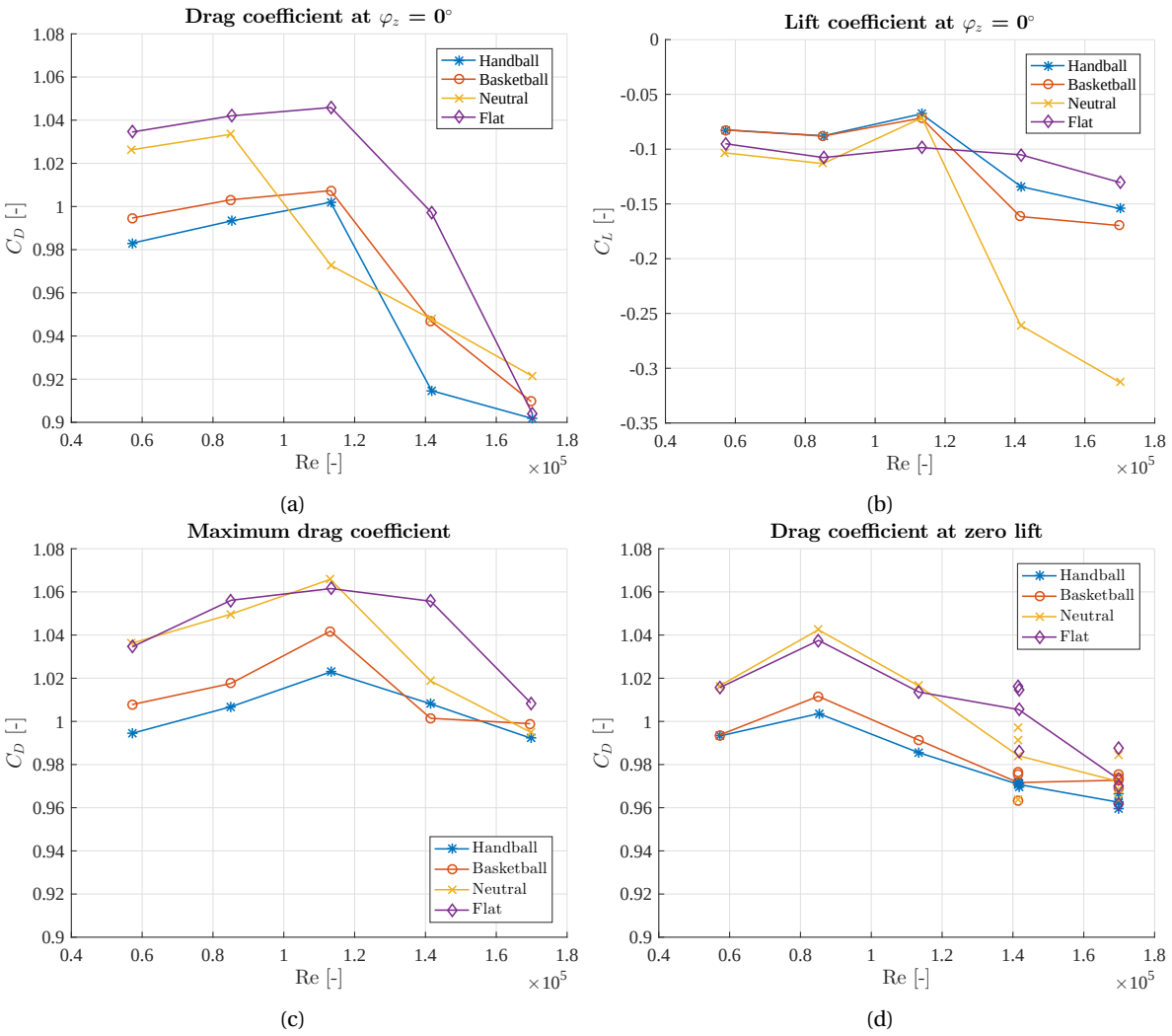

Figure 5.10: Collection of force coefficients as a function of Reynolds number for the different hand cuppings. (a) And (b) gives the drag and lift coefficients at $\varphi_z = 0°$, respectively; (c) shows the effects on the maximum drag coefficient; (d) shows the effects on drag coefficient for zero lift.

in drag coefficient were observed for experiments carried out with decreasing and increasing angles of attack. This indicates that effects of hysteresis are present in the flow around the arm models, in similarity to airfoils. This emphasizes the importance to perform all experiments consistently with either increasing or decreasing angles of attack.

5.3.2. Force coefficients versus Reynolds number

A presentation of selected drag and lift coefficients as function of Reynolds number is given figure 5.10, and discussed in this subsection. The data from figures 5.5 – 5.9 has been used for this purpose. The graphs from figure 5.10 demonstrate that no Reynolds number independent effects are found during the present study, in contrary to previous research. Variations in C_D of 15% are observed over the range of Reynolds numbers. A significant decrease in C_D occurs for $\mathrm{Re} > 1.2 \cdot 10^5$. This decrease can be linked to a drag crisis around the cylindrically shaped forearm.

Drag and lift coefficient at $\varphi_z = 0°$

As was mentioned, previous research found a maximum in drag for $\varphi_z = 0°$. During the present study this was not found to be the case. Insight into the drag and lift coefficient at $\varphi_z = 0°$ is still interesting since this is the reference case to literature. Figure 5.10a and 5.10b show C_D and C_L at $\varphi_z = 0°$ as a function of Reynolds number. The *flat* hand gives most drag over the whole Reynolds number range. The *neutral* hand has a trend

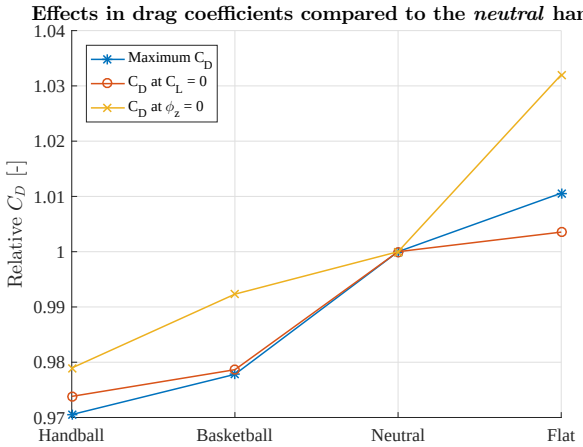

Figure 5.11: For the drag coefficients from figure 5.10 a weighted average over the Reynolds number is range is taken. Then weighted averages are compared relatively to that of the *neutral* hand.

break at Re = $1.1 \cdot 10^5$ as can be seen in figure 5.7b, rotating the arm with $\pm 2°$ changes C_D significantly. For every Reynolds number lower drag is observed for a more cupped hand.

Figure 5.10b shows that the lift coefficient is always negative at $\varphi_z = 0°$, hence it points in a direction from the thumb to the little finger. Especially a large lift coefficient acts on the *neutral* hand for higher Reynolds numbers, leading to a resultant force that acts on the hand with a relatively large angle.

Maximum drag coefficient

One might argue that a swimmer is purely looking for an arm/hand orientation that maximizes the drag coefficient. Figure 5.10c presents the maximum drag coefficient for the arm models as a function of Reynolds number. It shows an equal trend as 5.10a where cupping the hand only leads to a reduce in drag coefficient.

Drag coefficient at zero lift

It was mentioned that the orientation with zero lift is of interest to reduce shear forces acting on the hand of the swimmer. For each arm model and Reynolds number it is determined for what φ_z the lift force is closest to zero, such that the corresponding C_D can be determined. For 10, 15 and 20 $\mathrm{m\,s^{-1}}$ this seems trivial since the lift curves intersect $C_L = 0$ just once. But for 25 and 30 $\mathrm{m\,s^{-1}}$ the lift curves intersect $C_L = 0$ up to three times, as shown in figures 5.8 and 5.9 . The mean drag coefficient corresponding to the three points where $C_L = 0$ are taken into account in figure 5.10d, where the individual points are plotted as well. Based on these remarks figure 5.10d is formed, which shows the same effect of having a flat hand is beneficial and cupping only reduces the drag coefficient.

Reynolds number averaged drag coefficients

The weighted averages of the drag coefficients of the graphs from figure 5.10 are taken, after which they are normalized by the weighted average of the *neutral* hand. This allows for easy comparison between the different arm models over the whole Reynolds number range. Figure 5.11 presents the averaged drag coefficients relative to *neutral* hand. It can be seen that the flatter the hand is, the more drag it experiences. In comparison to the *neutral* hand, the *handball* shape experiences 2% to 3% less drag, the *basketball* model experiences 1% to 3% less drag, and the *flat* model experiences 0.5% to 3% more drag.

5.3.3. Repeatability

The drag and lift curves from figures 5.5 – 5.9 showed some irregularities, with the occurrence of local minima and maxima. Verification is needed whether these irregularities are a result of random errors or actually introduced by the fluid flow. For insight in the repeatability of experiments, the experiments for the *neutral* model are performed two times. Figure 5.12a shows the resulting drag coefficients for 20 $\mathrm{m\,s^{-1}}$, 'Data set 1' corresponds to the data as in figure 5.7a. 'Data set 2' comes from the repeated experiments, where only a collection of matching angles of attack is investigated.

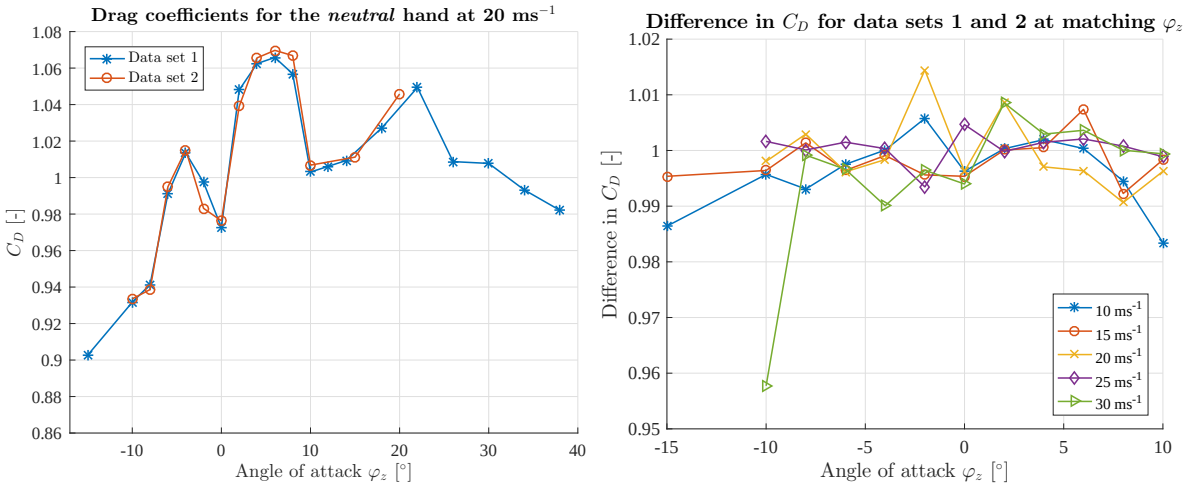

(a) (b)

Figure 5.12: The effects of repeating the experiments for the *neutral* hand. (a) Shows the drag coefficients for the repeated experiments at $V = 20\,\mathrm{m\,s^{-1}}$. (b) Shows the differences in C_D found for the repeated experiments.

Table 5.4: Influence of the balance system's accuracy ($\eta = 0.01$ N) on the measured drag forces.

Velocity [m s^{-1}]	F_D [N]	η / F_D [%]
10	2.5	0.4
15	6	0.2
20	10	0.1
25	16	0.06
30	23	0.04

Drag coefficients for both data sets follow a similar trend, with local minima and maxima for the same angles of attack. Measurements performed at matching φ_z result in values of C_D that are very similar. Repetition of the experiments at other flow velocities led to similar figures and observations, hence only the effects for $20\,\mathrm{m\,s^{-1}}$ are presented. However, for all velocities the relative difference in C_D for the two data sets is given in figure 5.12b. Differences are generally around 0.5% – 1.0%. At lower velocities the accuracy η of the balance system plays an important role, where $\eta = 0.01$ N/0.01 N m.

Table 5.4 gives typical drag forces F_D that were measured at each flow velocity, whereafter the accuracy is given in comparison to the drag force. Apparently the balance system already introduces errors up to 0.4%. Based on this and figure 5.12b can be concluded that the experiments are very well repeatable for the chosen experimental procedure.

5.4. Conclusion

The research inside the LTT showed that the drag coefficient C_D is largely affected by the angle of attack φ_z, a small variation of 2° can be responsible for variations in C_D of 4%. A maximum in C_D is never found where the projected area is maximized ($\varphi_z = 0°$), furthermore the angle of attack where maximum C_D occurs varies per Reynolds number and arm model. This shows the importance of always varying the angle of attack when research is done towards force coefficients of human arm models. It also demonstrates that a high accuracy is needed for varying the angle of attack, as a small difference of 2° has large effects on C_D. Some local maxima in C_D were observed. During future research the angles of attack can be varied more gradually around these maxima for more insight in the effects.

Especially at low Reynolds numbers a clear distinction is observed for the drag curves from different arm models. Differences in C_D between the arm models are up to 6%, where the *flat* and *neutral* hand shape are responsible for largest C_D. The differences in C_D become smaller at the largest investigated Reynolds numbers, resulting in differences in C_D up to 2% between the arm models. Although, still a clear distinction in performance for the different hand shapes is seen at high Reynolds numbers.

The Reynolds number effects are investigated for the maximum drag coefficient, the drag coefficient at zero lift, and the drag coefficient at $\varphi_z = 0°$. They all showed that a cupped hand is not beneficial for maxi-

mizing drag forces. In fact, it appears that the *flat* hand shape is always optimal. As hands are getting more cupped the drag coefficients are always decreasing, this is the case over the whole investigated range of Reynolds numbers, this range covers the Reynolds numbers found in swimming. This is in contrary to the cupped disks, where chapter 1 showed that a small cupping could be beneficial for increasing the drag.

Taking a weighted average over the different C_D versus Reynolds number plots from figure 5.10 shows relative effects of drag over the whole velocity range during a swimming stroke. They all show the same order of performance for the different cupped hands, with only a difference in their magnitudes. Depending on the used criteria, a *flat* hand can reach up to 3% larger C_D than a *neutral* hand. Furthermore, the *basketball* and *handball* models found decreases in C_D up to 2% and 3%, respectively.

For the currently used arm models it is always advised to make a swimmers hand as flat as possible, while simultaneously maintaining a 5° finger spreading, as this maximizes drag forces according to all different analysis on force coefficients. The hand models were given a 5° finger spreading, as this was found optimal from the research in chapter 2. However, this is not necessarily an optimum finger spreading for the flat hand as well. Therefore it would be interesting to investigate the effect of finger spreading for the *flat* hand during future research.

The local minima and maxima in the drag coefficient were linked to a phenomenon similar to a drag crisis. Here wall roughness played an important role as this accelerates the effects of boundary layer transition and causes a shift in the drag crisis towards lower Reynolds numbers.

Furthermore, drag coefficients for the arm models are showing Reynolds number dependencies. An optimum appears for Re $\approx 10^5$, hereafter C_D decreases such that up to 10% lower values are obtained at Re $\approx 1.7 \cdot 10^5$. This decrease in C_D has again similarities to a drag crisis, where the cylindrically shaped forearm is expected responsible for this behaviour. Here the surface roughness of the arm models is of importance for the shift towards lower Re where the drag crisis occurs. For future research it is of interest to perform experiments at even larger Reynolds numbers, such that a drag crisis hypothesis can be validated, even though these higher Reynolds numbers are unrealistic for swimming. Furthermore, it would be of interest to look into the effects on C_D for arm models with a hydrodynamically smooth surface. Because for a smooth surface it takes longer before the boundary layer becomes turbulent. Surface roughness can affect the flow differently around different arm models at different Reynolds numbers and angles of attack. Hence performing experiments with a smooth surface can for example show whether the local minima in drag curves are a result of surface roughness. The observed Reynolds number dependency shows the importance to always vary the Reynolds number for research on force coefficients of arm models.

The repetition of experiments showed the reliability of the used experimental setup. Differences in C_D for repeated experiments were smaller than 1%, and generally smaller than 0.5%. Forces are relatively small at low Reynolds numbers, therefore the measuring accuracy plays an important role in the observed measurement errors at low Re. As fluctuations in the flow become larger at higher Re, fluctuations in measured forces also increase. Therefore the relative magnitude of the measurement errors did not decrease at high Reynolds numbers.

This study used a set of four arm models all generated from the same base model inside MakeHuman, this base model concerns the *neutral* hand with a 5° finger spreading. Among the human population variations in hand and arm geometry exist, these four arm models are not corresponding to that of all professional swimmers per definition. However, it is likely that found conclusions for this particular set of hand configurations can be extended to most human arms. Because the found trend is very clear, where a more flat hand is always performing better. It is unlikely that this trend is specific for this particular arm geometry. However magnitudes of the found effects are likely to vary for different human arms.

Taking everything into consideration gives as advise to swimmers to always make the hands as flat as possible while simultaneously maintaining a 5° finger spreading to maximize propulsive forces. This result is independent of the stroke velocity and angle of attack of the arm.

6

Conclusion

Extensive experimental research was carried out towards the effects on drag forces for three-dimensional arm models with varying finger spreadings and hand cuppings. Furthermore, CFD simulations were performed on simplified hand models that represent finger spreading. This chapter gives concluding remarks of all done research, together with some recommendations for future research. Finally, performance enhancements in swimming are derived based on the outcomes of the experimental research.

As a fist statement it should be taken into consideration the the experimental research only looked at fluid flow in a steady state, with the arm model at a fixed orientation towards the flow. A swimming stroke is a rather complicated motion, where the arm is rotating and (de)accelerations take place. Effects of hand cupping were not investigated in the past, the current research at constant velocities is a necessary step before looking into unsteady effects.

During this research all experiments were done for one particular set of arm models. It should be kept in mind that variations in the human body occur along the population. Therefore the found experimental results cannot necessarily be extended to that of arm models with different geometries. Although, the optimum in hand cupping was found at a boundary condition where the hand was completely flat. This indicates that a flat hand is always beneficial for maximizing drag forces. Different research groups tend to make use of different arm models, it is suggested to make use of a standardized arm model for all research towards propulsion in swimming, this allows for better comparisons of different swimming research.

Angles of attack and hand configurations were investigated without paying attention to the required energy consumption to maintain these. It can be argued that it is more energy consuming to maintain a complete flat hand for long distance swimming, compared to a relaxed neutral position. Similarly, large angles of attack can be more more difficult to maintain. It would be interesting to look into the effects of energetic efficiency during swimming. Such that a hand configuration can be found that maximizes propulsive forces and minimizes energy consumption.

Chapter 2 looked into the effects of finger spreading by towing five different hand shapes through a large water tank, here it concerned hands with a neutral hand cupping. The arm models were only partly immersed, such that the forearm was piercing the water surface. Obtained results were partly in agreement with previous research, as it confirmed that a small finger spreading is beneficial for drag maximization. A finger spreading of 5° was found responsible for an increase in force and moment based drag coefficients of 1.1% and 1.7%, respectively. Furthermore, it appeared that finger spreadings larger than 10° were always disadvantageous for drag maximization. The research indicated that Reynolds number independent effects apply for the hand models in the absence of a free water surface. It appeared that a towing tank is a suitable experimental setup for finding small differences in drag acting on different hand shapes. Although the introduced component of wave drag due to the interface piercing forearm might be undesirable. The research showed that a variation of the immersion depth affects the values of C_D, indicating that not all interference in the flow generated by the fingers and forearm is taken into account for a small immersion depth. However, still a clear distinction in drag coefficients of the different finger spreadings was obtained.

Wind tunnel experiments were carried out for a variety of cupped hand models in chapter 4, those models have a 5° finger spreading as the towing tank research found this optimal. It appeared that varying the angle of attack φ_z is of great importance when looking into effects of drag and lift that act on arm models. Small variations in φ_z of 2° can be responsible for variations in C_D of 4%. Furthermore it was shown that, in contrary

to cupped disks, cupping the hand is not beneficial for increasing drag forces. For a *flat* hand an increase in drag of 0.5% to 3% compared to a *neutral* hand was found. Furthermore, a decrease in drag coefficient of up to 3% was found for the cupped hands. The Low Turbulence Tunnel appeared to be a suitable facility for well rounded research towards aerodynamic forces acting on arm models. It has a high measuring accuracy, reaches high flow velocities, has a low turbulence intensity and a large test section. Moreover, the possibility to easily adjust the angle of attack with high accuracy was found of great value for the current study.

CFD simulations were carried out in chapter 3 to look into the effects of abstractly modelling a hand with finger spreading. Various slotted disks that could represent finger spreading were created for this purpose. Simulations carried out with two turbulence models, both having suitable characteristics for this modelling problem, lead to contradicting results in drag coefficients. This indicated that simple simulations around slotted disks are not viable to represent hands with finger spreading. Experimental research by means of wind tunnel tests is recommended to look into the effects of drag for the slotted disks before continuing any simulations.

The experimental results provided information that swimmers can use to improve their performance, with the remark that the research concerns just one particular set of arm models and experiments are done at a constant velocity. Chapter 1 showed that the 50 m freestyle swimming for women has finishing times around 24 s, where a difference of only 0.12 s can result in a sixth place or a gold medal. This indicates that improving the swimming velocity U with only 0.5% can lead to a podium place. A short analysis on the power and forces generated by a swimmer can give insight in the changes in finishing times for varying hand configurations. When a swimmer moves at a constant velocity U through the water, the drag force F_D generated by its limbs is equal to the resistive forces $F_{D,B}$ acting on its body, such that

$$F_D = F_{D,B} \rightarrow \frac{1}{2}\rho V^2 A C_D = \frac{1}{2}\rho U^2 A_B C_{D,B}. \tag{6.1}$$

Here A_B and $C_{D,B}$ are respectively the frontal projected area and drag coefficient corresponding to the body of the swimmer, which are assumed constant. The velocity U needs maximization in order to improve the swimming performance. With equation 6.1 a scaling argument for the velocity U is found as

$$U \sim \sqrt{V^2 C_D}. \tag{6.2}$$

Furthermore, the power P that a swimmer can generate with its muscles is assumed constant, and is expressed as

$$P = F_D V = \text{constant} \rightarrow F_D \sim V^{-1}. \tag{6.3}$$

Simultaneously, the drag force generated by the arm is

$$F_D = \frac{1}{2}\rho V^2 A C_D \sim V^2 C_D. \tag{6.4}$$

Combining equations 6.2, 6.3 and 6.4 gives a scaling argument for the swimming velocity as

$$U \sim C_D^{1/6}. \tag{6.5}$$

The required swimming time for a distance s then scales as

$$t = \frac{s}{U} \sim C_D^{-1/6}. \tag{6.6}$$

Finally, the changes in finishing times with respect to a reference arm model are determined as

$$\Delta t = t^* - t^* \left(\frac{C_D^*}{C_D}\right)^{1/6}, \tag{6.7}$$

here t^* and C_D^* are the finishing time and drag coefficients corresponding to the reference model. Section 1.3 mentioned that 85% to 90% of propulsive forces in swimming are generated by the arm and hand, where the hand has a 2.5 times larger contribution to the drag. Taking this into consideration, in combination with equation 6.7, gives insight in the changes in finishing times for different hand configurations. The towing tank experiments show that a 5° finger spreading can decrease the finishing times with 0.03 s, compared to closed fingers. Similarly, a 20° finger spreading leads to an increase in finishing times of 0.04 s. The wind tunnel research shows that a *flat* hand decreases the finishing time with 0.02 s to 0.10 s, compared to a *neutral* hand. The largest investigated hand cupping leads to an increase in finishing times of 0.07 s to 0.10 s. This short analysis on the effects of drag coefficients of the hand on finishing times, shows that having an optimal hand configuration is of large importance in swimming. From which is recommended to use a *flat* hand with 5° finger spreading in competitive swimming to increase the chances of winning medals.

A

Force measuring system: towing tank

The force measuring system used in chapter 2 is composed of load cells that are chosen based on the expected forces an moments acting on the arm models. The partly immersed arm models have a frontal projected area $A \approx 0.025$ m^2. Chapter 1 showed drag coefficients for hand models are around $C_D \approx 1.1$. Then for a water density $\rho = 998$ kg m^{-3} and the towing velocities from table 2.1 the expected drag forces F_D are in a range of 3.4 - 55 N. Assuming that the mean drag force acts on the centre of the immersed hand part, the drag-induced moments M_D are of the range 1.4 - 22 Nm.

Figure A.1 gives a schematic top view of the bottom frame that was displayed in figure 2.3. The locations of the six different load cells and distance to the centre of the frame are given. One load cell ($F_{x,1}$) measures force in the x-direction. Two loads cells ($F_{y,1}$, $F_{y,2}$), measure in the y-direction. And three loads cells ($F_{z,1}$, $F_{z,2}$, $F_{z,3}$) measure in the z-direction. The forces measured by the load cells can be translated into forces and moments acting on the arm models, by use of the known positions of the load cells from figure A.1. This results in equations A.1 to A.6, describing the calculation of F_x, F_y, F_z, M_x, M_y and M_z.

$$F_x = F_{x,1} \tag{A.1}$$

$$F_y = F_{y,1} + F_{y,2} \tag{A.2}$$

$$F_z = F_{z,1} + F_{z,2} + F_{z,3} \tag{A.3}$$

$$M_x = 0.2274 \cdot (F_{z,1} - F_{z,2}) \tag{A.4}$$

$$M_y = 0.13125 \cdot (F_{z,1} + F_{z,2}) - 0.2625 \cdot F_{z,3} \tag{A.5}$$

$$M_z = 0.235 \cdot (F_{y,1} - F_{y,2}) \tag{A.6}$$

The capacity of the six load cells is chosen in such a way that the expected forces and moments are measured accurately. Table A.1 gives an overview of the selected load cells and their capacities and measuring intervals. Based on the load cell intervals from table A.1, the measuring intervals of F_x and M_y are determined as ± 0.06 N and ± 0.09 N m, respectively. Based on the measuring intervals and the expected drag forces F_x and drag moments M_y, the measuring accuracies of F_x and M_y are determined and presented in figure A.2. Figure A.2 indicates that F_x is measured more accurate at higher towing velocities, with a measuring accuracy smaller than 0.5% for $V > 1$ m s^{-1}. M_y is measured more accurate at lower towing velocities, with a measuring accuracy around 1% for $V < 1$ m s^{-1}.

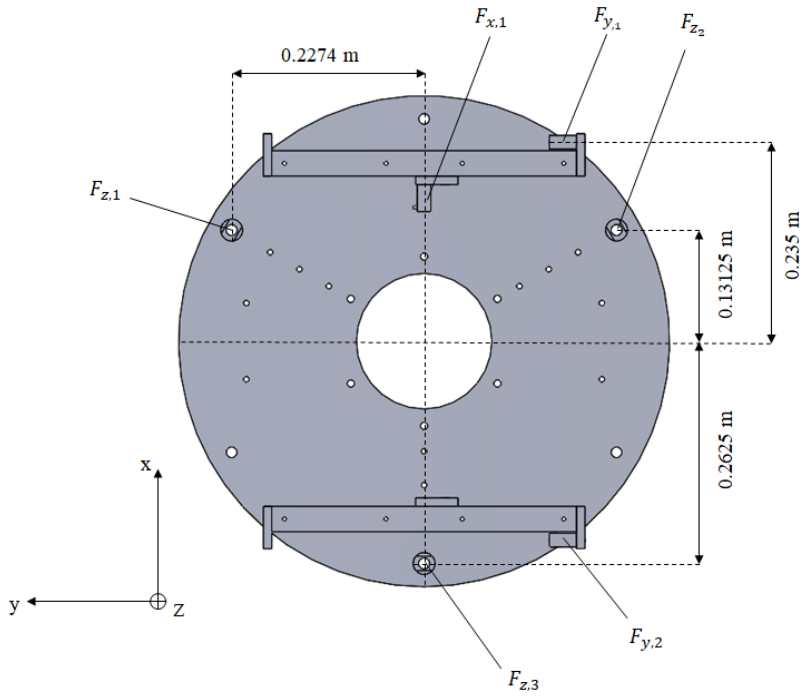

Figure A.1: Schematic top view of the six-component measurement system with the important dimensions and positions of the load cells.

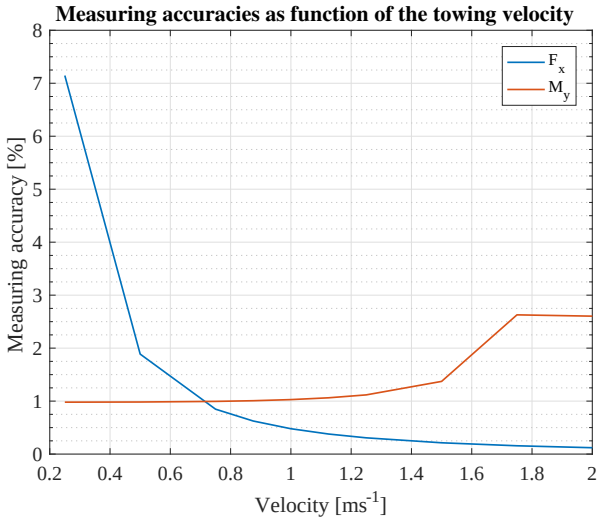

Figure A.2: Presentation of the measuring accuracies in F_x and M_y as function of the towing velocity. The accuracies are based on the measuring intervals for F_x and M_y and the expected forces and moments acting on the arm models.

Table A.1: Specifications of the used load cells (Zemic, 2013).

Transducer	Brand	Type	Capacity [N]	Measuring interval [N]
F_{x_1}	Zemic	L6J-C3D-15kg-0.45B	150	0.06
F_{y_1}	Zemic	L6J-C3D-5kg-0.45B	50	0.02
F_{y_2}	Zemic	L6J-C3D-5kg-0.45B	50	0.02
F_{z_1}	Zemic	H3-C3-50kg-3B	500	0.17
F_{z_2}	Zemic	H3-C3-50kg-3B	500	0.17
F_{z_3}	Zemic	H3-C3-50kg-3B	500	0.17

B

Numerical settings

Table B.1: Numerical settings used during the CFD simulations carried out in ANSYS Fluent in chapter 3.

Solver	Type	Pressure-Based
	Time	Steady
Pressure-Velocity Coupling	Scheme	Coupled
Spatial Discretization	Gradient	Least Squares Cell Based
	Pressure	Second order
	Momentum	Second Order Upwind
	Turbulent Kinetic Energy	Second Order Upwind
	Turbulent Dissipation Rate	Second Order Upwind

C

Wind tunnel flow velocity

The wind tunnel consists of a contraction cone in which the flow velocity is increased by reducing the pressure. The pressure difference ΔP over this cone is determined by two pressure sensors, the flow velocity leaving the contraction cone can be determined with the Bernoulli equation, given as

$$\frac{1}{2}V^2 + gz + \frac{P}{\rho} = \text{constant}. \tag{C.1}$$

Here z is the elevation of the fluid, which can be neglected. P is the static pressure that is measured in the the contraction cone. From the principle of conservation of mass follows that $\rho_1 A_1 V_1 = \rho_2 A_2 V_2$. Here A_1 and A_2 are respectively the cross sectional areas of the inlet and outlet of the contraction cone, and V_1 and V_2 the respective velocities at these points. It is assumed that no density changes occur over the cone and $A_1/A_2 << 1$, then the flow velocity entering the test section is found by rewriting equation C.1 to

$$V_2 = \sqrt{\frac{2(P_1 - P_2)}{\rho}}. \tag{C.2}$$

D

Force measuring system: LTT

Figure D.1 illustrates the six-component balance system.

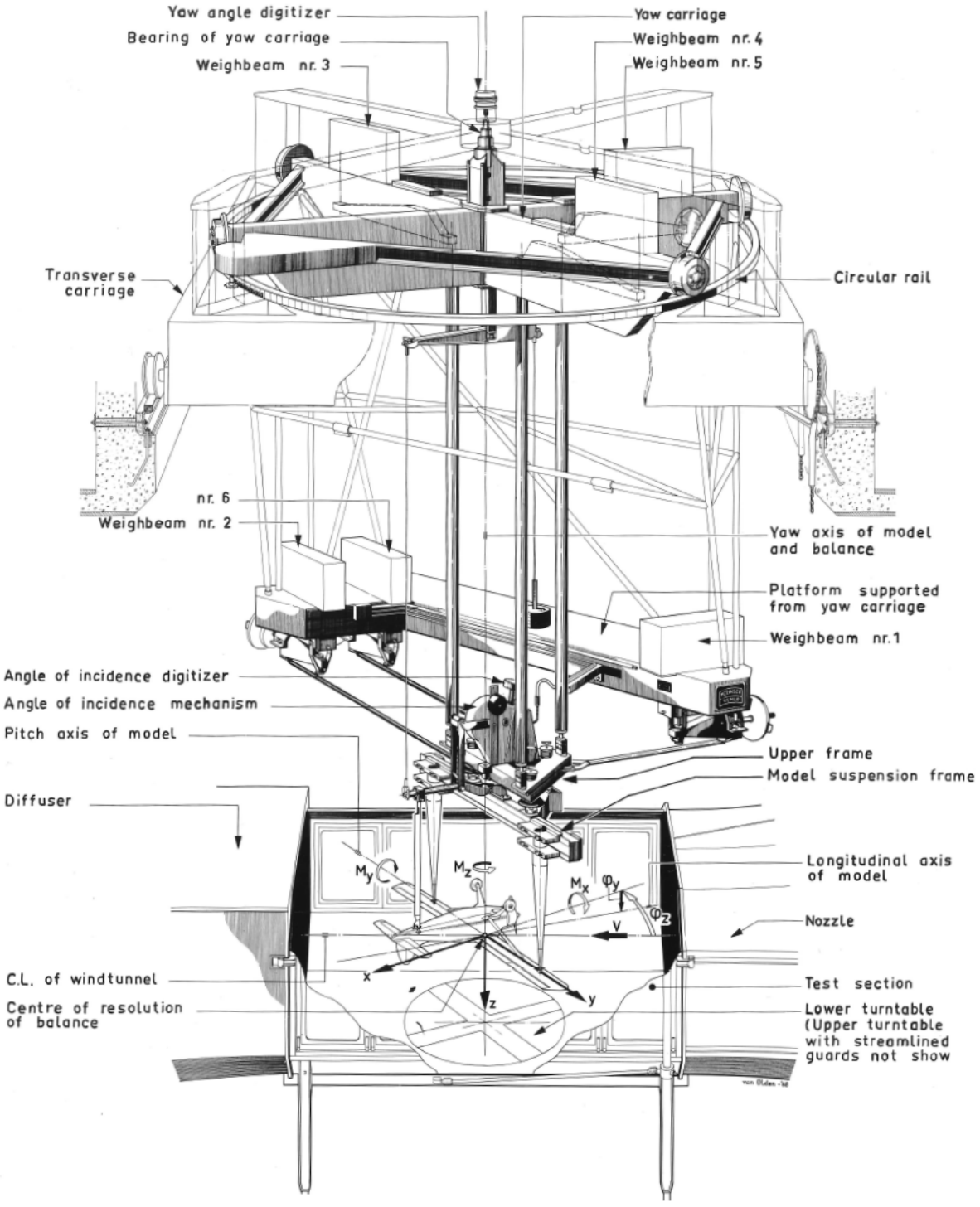

Figure D.1: Overview of the six-component balance system. Air is flowing from right to left with velocity V. Positive forces are pointing along the x, y and z-axis.

E

Point of application of force

Aerodynamic forces are distributed over the hand and forearm during the wind tunnel experiments from chapter 5. Especially insight in the distributed forces over the height of the arm model is of interest. The measurement of both the forces and moments provides information on the distribution of forces. For example for a two-dimensional case, if a point force F_x and moment M_y are measured with $M_y = LF_x$, and L is the length of the forearm, it indicates that the drag force is concentrated at the hand. This appendix describes a method to determine the distribution of forces for the three-dimensional case. A sensitivity analysis is used to investigate the effects of couple moments. Finally the method is applied to the experimental data on cupped hands from chapter 5.

E.1. Analytical method

For the three-dimensional case of the experiments from chapter 5, the measured forces $\vec{F}$ are distributed at distances $\vec{a}$ from the origin of the coordinate system, illustrated in figure E.1a. In other words, the distances $\vec{a}$ correspond to the point of application of force (POA). It is tempting to define the POA such that

$$\vec{M} = \vec{a} \times \vec{F}, \tag{E.1}$$

given in matrix notation as

$$\begin{bmatrix} M_x \\ M_y \\ M_z \end{bmatrix} = \begin{bmatrix} a_y F_z - a_z F_y \\ a_z F_x - a_x F_z \\ a_x F_y - a_y F_x \end{bmatrix}. \tag{E.2}$$

Here $\vec{F}$ and $\vec{M}$ are the forces and moments measured during the experiments. Equation E.1 cannot be solved as the system of three equations is linearly dependent, i.e. it only contains two unique equations while $\vec{a}$ contains three unknown variables. Further characteristics of the POA introduce two extra equations that have to be satisfied, namely

$$|\vec{a}| = \frac{|\vec{M}|}{|\vec{F}|} \tag{E.3}$$

and

$$\vec{a}^{\top} \cdot \vec{F} = 0. \tag{E.4}$$

Here equation E.3 follows from equation E.1, and equation E.4 follows from the principle that vector $\vec{a}$ is perpendicular to $\vec{F}$. The introduction of equations E.3 and E.4, together with the two linear independent equations of E.1, leads to an overdetermined system of equations. Because there are now four linear independent equations and only the three unknown variables in $\vec{a}$.

The distance a_z (POA along the height of the arm) occurs in both the moments M_x and M_y from equation E.2. Due to the overdetermined system of equations, only one of the moment equations from equation E.2 can be solved exactly while simultaneously solving equations E.3 and E.4. It is observed that M_y dominates for $\varphi_z \to 0°$, while M_x dominates for $\varphi_z \to \pm 90°$. As an approach, equations for both M_x and M_y are tried to solve simultaneously, where no exact solving of the equations takes place. Solving for both M_x and M_y results in the calculation of $\vec{a}$. Substituting the calculated $\vec{a}$ in equation E.2 results in the the calculated moment vector

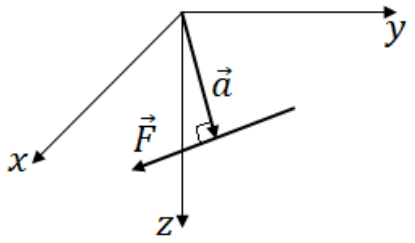

(a) Coordinate system in which $\vec{F}$ applies orthogonal to the origin with $\vec{a}$.

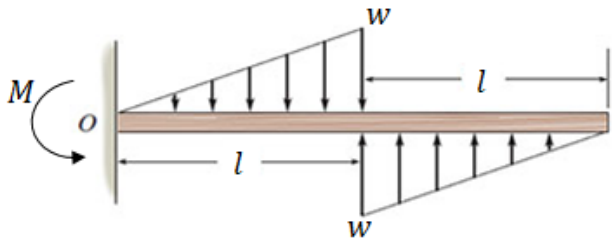

(b) A beam with 2 equally sized pressure distributions on both it sides, resulting in a couple moment M and zero resultant force. Modified from Chegg (2018).

Figure E.1: Coordinate system and visualization of couple moments for analysis point of application.

$\vec{M}'$. Errors are present in the calculated moments M'_x and M'_y, compared to the measured moments M_x and M_y, errors are defined as

$$\varepsilon_{x,y} = \frac{M_{x,y} - M'_{x,y}}{M_{x,y}} \tag{E.5}$$

The error ε_x needs minimization for $\varphi_z \to \pm 90°$, as the moment M_x dominates for these angles of attack. Similarly, the error in ε_y needs minimization for $\varphi_z \to 0°$. From this an error is introduced that needs minimization, expressed as

$$\varepsilon = \sqrt{(\varepsilon_x \sin\varphi_z)^2 + (\varepsilon_y \cos\varphi_z)^2}. \tag{E.6}$$

An error formulated in this way allows for prioritizing the minimization of the error in the dominating moment. The system of equations necessary for determining the POA is solved iterative, such that a solution is found that minimizes the error ε. In this way an estimate of the point of application of force is found.

A possible reason behind the errors in the calculated moments M'_x and M'_y are couple moments acting on the arm models. Figure E.1b gives an illustration of a distributed pressure acting on a beam. The two pressure distributions are equal in size but oppositely directed, this introduces a couple moment while there is zero resultant force. It is expected that the distributed pressures on the arm models are not necessarily pointing in one direction, this would lead to the introduction on couple moments on the arm models. A sensitivity analysis is carried out in section E.2 that gives insight in the effects of couple moments, while the resultant force is zero. Furthermore, in section E.3 the method for determining the POA is applied to the experimental data on the cupped hands from chapter 5.

E.2. Sensitivity analysis

To investigate the effect of couple moments a sensitivity analysis is performed for artificial data. Points of attraction for simultaneously varying M_x and M_y are found. Hereby the error from equation E.6 is minimized. Now the sensitivity analysis is performed for varying M_x and M_y, such that $\vec{M} = \vec{M} + \vec{\delta}$, here $\vec{\delta}$ is the introduced couple moment. Figure E.2a demonstrates the error ε as a function of the simultaneously varying moments M_x and M_y. Figure E.2b shows their corresponding values of a_z. It is observed that $\varepsilon = 0$ when $\vec{\delta} = 0$, where no couple moments are introduced. a_z is varying significantly throughout the surface space, while ε remains small. This makes the current used method promising for finding the POA when couple moments are introduced to the experimental data.

E.3. Point of application of force

The point of application of force gives information about the distribution of drag forces on the arm models. The described procedure from section E.1 is used for finding an estimate of a_z for the experimental data on the cupped hands from chapter 5. Furthermore, comparisons are made with the two-dimensional case where $a'_z = M_y / F_x$. Similar graphs for a_z and a'_z are found for the different investigated flow velocities. Therefore figure E.3 presents just the results of a_z and a'_z at 15 $\mathrm{m\,s^{-1}}$. As described in section E.1, errors $\varepsilon_{x,y}$ are introduced, these are presented in figure E.4.

Figure E.3 shows opposite behaviour in a_z and a'_z. Where a_z increases for increasing φ_z is a'_z decreasing. The shape and projected area of forearm are not varying much by changing the angle of attack, therefore

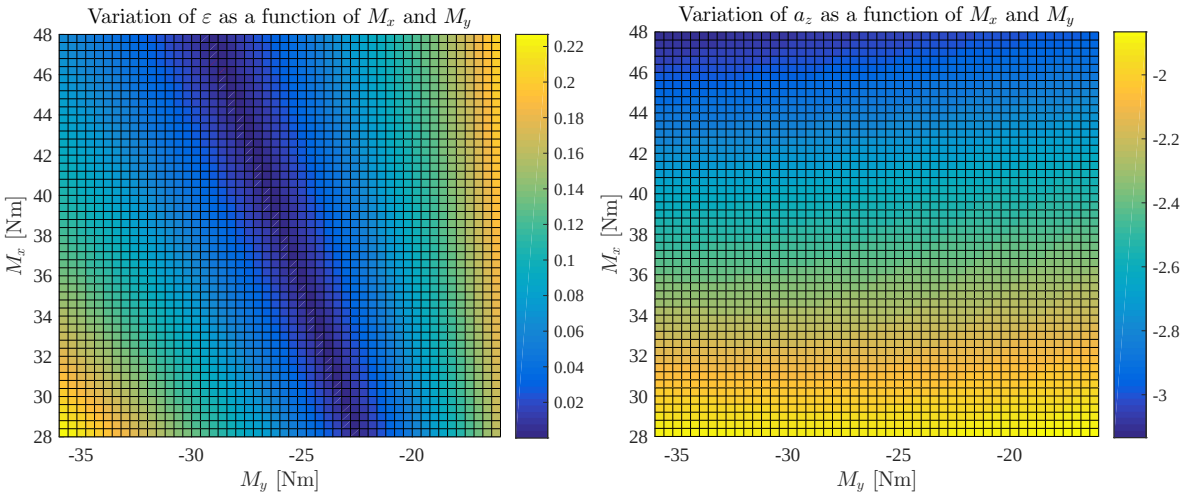

(a) (b)

Figure E.2: Sensitivity analysis for varying M_x and M_y. (a) presents the obtained minimum error ε. While (b) shows the corresponding variation of a_z

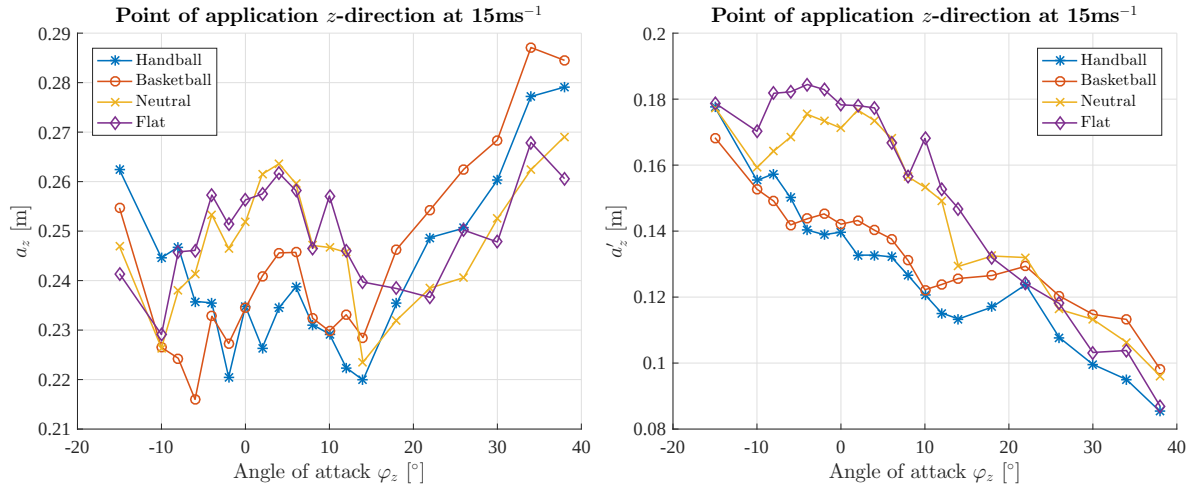

(a) (b)

Figure E.3: (a) Gives a_z based on the analytical method from section E.3. (b) presents $a'_z = M_y/F_x$. Positive values of a_z and a'_z are directed from the base of the arm to the hand.

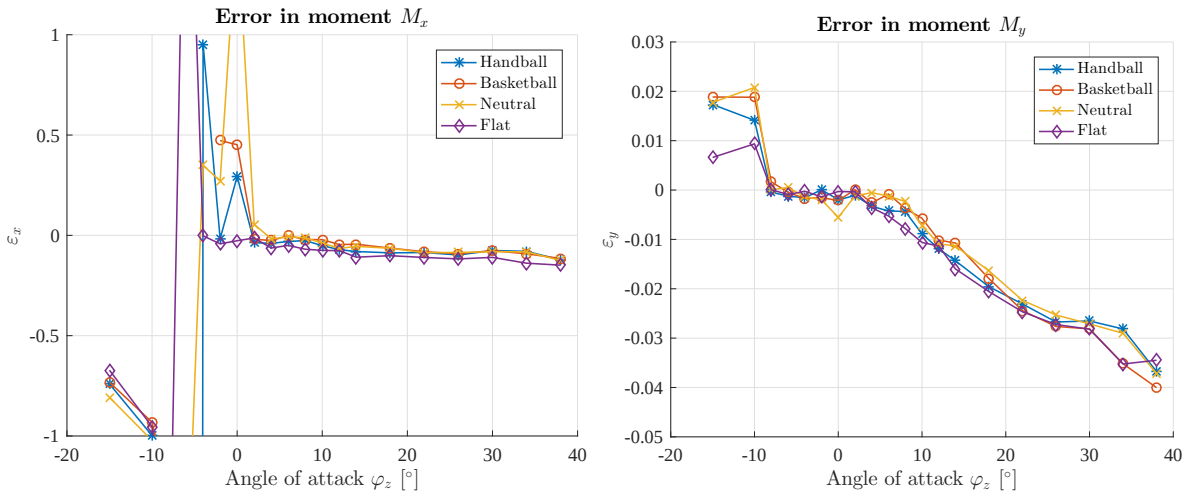

(a) (b)

Figure E.4: Presentation of the errors in the moments following from the calculated POA. (a) gives the error in M_x and (b) the error in M_y.

it is expected that the contribution of the forearm is approximately constant independent of the angle of attack. C_D decreases for increasing φ_z, meaning that the contribution of the hand to C_D decreases. As the contribution of the hand decreases, the POA should shift more towards the forearm, since the contribution of the forearm on C_D increases. This should mean that a_z and a'_z decrease for increasing φ_z. Only a'_z shows such behaviour. Although the graphs show similar behaviour for φ_z = -10 - 14°, a strong increase in a_z is found for $\varphi_z > 14°$. This observation suggests that errors in M'_x and M'_y are large for $\varphi_z > 14°$. However for this region of φ_z figure E.4 shows that $\varepsilon_x < 10\%$ and $\varepsilon_y < 4\%$. As these errors are small, it gives the impression that a_z is determined accurately. Calculations of a_z seem less reliable for $\varphi_z < 2°$, as the error ε_x is large for those angle of attack. As a'_z shows a strongly different behaviour it can be seen that assuming $M_y = f(F_x, a_z)$ is incorrect, such that $M_y = f(F_x, F_z, a_x, a_z)$ is a better approach. This is expected to be an artefact of the used experimental setup. Here a large component of $F_z \approx 0.4F_x$ is introduced by mounting the arm models directly to the turntable plate. This subsequently introduces a large influence of F_z on M_y.

Bibliography

ANSYS, I. (2009). ANSYS FLUENT 12.0 User's Guide.

Barlow, J. B., Rae, W. H., & Pope, A. (1999). *Low-Speed Wind Tunnel Testing*. New York: Wiley-Interscience, 3 edition ed.

Batchelor, G. K. (2000). *An Introduction to Fluid Dynamics*. Cambridge: Cambridge University Press.

Bilinauskaite, M., Mantha, V. R., Rouboa, A. I., Ziliukas, P., & Silva, A. J. (2013). Computational Fluid Dynamics Study of Swimmer's Hand Velocity, Orientation, and Shape: Contributions to Hydrodynamics. *BioMed Research International*.

Chegg (2018). Homework Problem. http://www.chegg.com/homework-help/questions-and-answers/replace-loading-equivalent-resultant-force-couple-moment-acting-point-o-suppose-w-40-lb-ft-q18784390.

Crowe, C. T., Elger, D. F., Roberson, J. A., & Williams, B. C. (2008). *Engineering Fluid Mechanics*. Hoboken, NJ: Wiley, 9 edition ed.

Dimchev, M. (2012). *Experimental and Numerical Study on Wingtip Mounted Propellers for Low Aspect Ratio UAV Design*. Master of Science Thesis, Delft University of Technology.

Frei, W. (2017). Which Turbulence Model Should I Choose for My CFD Application? https://www.comsol.com/blogs/which-turbulence-model-should-choose-cfd-application/.

Hoerner, S. F. (1965). *Fluid-Dynamic Drag*. Hoerner Fluid Dynamics, 2 ed.

Isyumov, N. (2015). Wind Engineering Terminology. Porto Alegre, Brazil.

Koo, B., Yang, J., Yeon, S. M., & Stern, F. (2014). Reynolds and Froude Number Effect on the Flow Past an Interface-Piercing Circular Cylinder. *International Journal of Naval Architecture and Ocean Engineering*, *6*(3), 529–561.

Kundu, P. K., Cohen, I. M., & Ph.D, D. R. D. (2015). *Fluid Mechanics, Sixth Edition*. Amsterdam ; Boston: Academic Press, 6 edition ed.

Lentink, D., Müller, U. K., Stamhuis, E. J., de Kat, R., van Gestel, W., Veldhuis, L. L. M., Henningsson, P., Hedenström, A., Videler, J. J., & van Leeuwen, J. L. (2007). How Swifts Control Their Glide Performance with Morphing Wings. *Nature*, *446*(7139), 1082–1085.

Lorente, S., Cetkin, E., Bello-Ochende, T., Meyer, J. P., & Bejan, A. (2012). The Constructal-Law Physics of Why Swimmers Must Spread Their Fingers and Toes. *Journal of Theoretical Biology*, *308*, 141–146.

Marinho, D. A., Barbosa, T. M., Reis, V. M., Kjendlie, P. L., Alves, F. B., Vilas-Boas, J. P., Machado, L., Silva, A. J., & Rouboa, A. I. (2010). Swimming Propulsion Forces Are Enhanced by a Small Finger Spread. *Journal of Applied Biomechanics*, *26*(1), 87–92.

Marinho, D. A., Reis, V. M., Alves, F. B., Vilas-Boas, J. P., Machado, L., Silva, A. J., & Rouboa, A. I. (2009). Hydrodynamic Drag during Gliding in Swimming. *Journal of Applied Biomechanics*, *25*(3), 253–257.

Maskell, E. C. (1963). A Theory of the Blockage Effects on Bluff Bodies and Stalled Wings in a Closed Wind Tunnel. Tech. rep., AERONAUTICAL RESEARCH COUNCIL LONDON (UNITED KINGDOM).

ME-Meßsysteme (2016). Datasheet 3-Axis Force Sensor K3D60a.

Minetti, A. E., Machtsiras, G., & Masters, J. C. (2009). The Optimum Finger Spacing in Human Swimming. *Journal of Biomechanics*, *42*(13), 2188–2190.

Nakayama, Y., & Boucher, R. F. (1998). 9 - Drag and Lift. In *Introduction to Fluid Mechanics*, (pp. 148–170). Oxford: Butterworth-Heinemann.

Nieuwstadt, F. T. M., Westerweel, J., & Boersma, B. J. (2016). *Turbulence: Introduction to Theory and Applications of Turbulent Flows*. Springer International Publishing.

Polloreno, J. (2014). The 4 Phases Of The Freestyle Swim Stroke. http://www.triathlete.com/2014/08/training/4-phases-freestyle-swim-stroke_103439.

Pytel, S. (2018). Taking breath swimming butterfly isolated black background. Royalty-free stock photo.

Schleihauf, R. E. (1979). A Hydrodynamic Analysis of Swimming Propulsion. *Swimming III*, *8*, 70–109.

Shapeways (2018). Strong & Flexible Plastic 3D Printing Material Information - Shapeways. https://www.shapeways.com/materials/strong-and-flexible-plastic.

Strzala, M., & Tyka, A. (2009). Physical Endurance, Somatic Indices and Swimming Technique Parameters as Determinants of Front Crawl Swimming Speed at Short Distances in Young Swimmers. *Medicina Sportiva*, *13*, 99–107.

Takagi, H., Shimizu, Y., Kurashima, A., & Sanders, R. (2001). Effect of Thumb Abduction and Adduction on Hydrodynamic Characteristics of a Model of the Human Hand.

The MakeHuman team (2016). MakeHuman.

Theunissen, R., Worboys, R., & Masullo, A. (2016). Near-wake analysis of perforated disks with varying hole topology. In *18th International Symposium on the Application of Laser and Imaging Techniques to Fluid Mechanics*. Lisbon, Portugal.

Timmer, W. A., & van Rooij, R. P. J. O. M. (2003). Summary of the Delft University Wind Turbine Dedicated Airfoils. *Journal of Solar Energy Engineering*, *125*(4), 488–496.

van Houwelingen, J., Schreven, S., Smeets, J. B., Clercx, H. J., & Beek, P. J. (2017). Effective Propulsion in Swimming: Grasping the Hydrodynamics of Hand and Arm Movements. *Journal of Applied Biomechanics*, *33*(1), 87–100.

van Houwelingen, J., Willemsen, D. H. J., Kunnen, R. P. J., van Heijst, G. F., Grift, E. J., Breugem, W. P., Delfos, R., Westerweel, J., Clercx, H. J. H., & van de Water, W. (2016). The Effect of Finger Spreading on Drag of the Hand in Human Swimming. *arXiv:1611.08578 [physics]*.

van Ingen Schenau, G. J., & Cavanagh, P. R. (1990). Power Equations in Endurance Sports. *Journal of Biomechanics*, *23*(9), 865–881.

van 't Veer, A. (2018). Towing Tank No. 2. https://www.tudelft.nl/3me/over-3me/organisatie/afdelingen/maritime-and-transport-technology/research/ship-hydromechanics/facilities/towing-tank-no-2/.

Westerweel, J., Breugem, W. P., Grift, E. J., & Tummers, M. (2016). Handiger Zwemmen. *Nederlands Tijschrift voor Natuurkunde*, (pp. 170–173).

White, F. M. (2011). *Fluid Mechanics*. McGraw Hill.

Willemsen, D. H. J. (2016). How to Swim More Efficiently by Spreading Your Fingers. Tech. rep., Eindhoven University of Technology.

Yang, Z., Igarashi, H., Martin, M., & Hu, H. (2008). An Experimental Investigation on Aerodynamic Hysteresis of a Low-Reynolds Number Airfoil. *46th AIAA Aerospace Sciences Meeting and Exhibit*.

Yu, T. (2010). Problem solution Kundu & Cohen 6.8.

Zemic (2013). Datasheet type H3 Load Cell.